Fracture Analysis of Orthotropic Beams

Linear Elastic and Non-Linear Methods

Stefansson, Fridberg

2001

Document Version:
Publisher's PDF, also known as Version of record

LUND UNIVERSITY

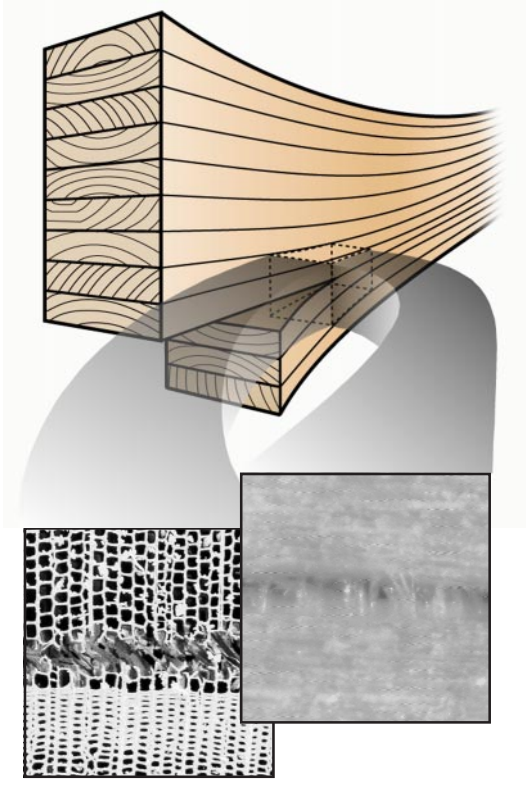

FRACTURE ANALYSIS OF ORTHOTROPIC BEAMS
Linear elastic and non-linear methods

FRIDBERG STEFANSSON

Structural Mechanics

Licentiate Dissertation

Structural Mechanics

ISRN LUTVDG/TVSM--01/3029--SE (1-137)
ISSN 0281-6679

FRACTURE ANALYSIS OF ORTHOTROPIC BEAMS
Linear elastic and non-linear methods

FRIDBERG STEFANSSON

Printed by KFS I Lund AB, Lund, Sweden, November 2001.

For information, address:
Division of Structural Mechanics, LTH, Lund University, Box 118, SE-221 00 Lund, Sweden.
Homepage: http://www.byggmek.lth.se

Preface

The work presented in this licentiate thesis has been carried out at the Division of Structural Mechanics, Lund Institute of Technology, Lund University. It was initiated by Professor Hans Petersson and partly financed by the Swedish Council for Building Research (BFR).

Throughout my work I have benefitted from the great patience and support of my supervisors, Dr. Per-Johan Gustafsson and Prof. Hans Petersson. Their guidance and valuable encouragement is gratefully acknowledged.

I would also like to express my gratitude to former colleagues and friends at the Division of Structural Mechanics who both knowing and unknowing have made vital contributions to this work.

Finally, I want to express my deepest gratitude to my family for making this work possible.

Abstract

The use of timber as a construction material demands continuous improvements of our knowledge about the material and computational techniques for structural analysis and design.

In this report the fracture properties of wood are studied and implemented into numerical crack propagation models. The numerical algorithms are utilized for computing the development of cracks in structural elements. Six types of timber beams, with holes and notches, are studied. Experimental results for critical load indicate that the numerical results are fairly accurate. In addition, numerical studies are performed regarding the influence of distribution of load at support, influence of beam geometry, load configuration and axial force. The experimental results presented include a comprehensive testing series on the fracture softening properties of wood in pure and combined shear and tension perpendicular to grain.

For end-notched beams, the distribution of load at support affects the load-bearing capacity when the loaded area is close to a corner. The way the load was distributed was found to have little influence on beams of different size, while the notch geometry has a strong influence on the load-bearing capacity. The notch depth and height are the main parameters where the notch height has the most intensive influence. Load configuration does not influence the load-bearing capacity to any greater extent except for external loads placed within a distance of beam height from the notch. In that case the load runs partly straight down to the support without affecting the stress singularity very much at the notch corner. If the supporting force is at an angle to the support area, an axial force may develop in the structure resulting in influence on the load-bearing capacity.

It may be convenient to use simple correction factors to specify in an approximate manner the influence of the studied parameters on the load-bearing capacity of structural elements.

Keywords: Fracture mechanics, wood, crack, notches, holes, finite element analysis.

Contents

Chapter 1

Introduction

1.1 General background

Different kinds of structural damage and disasters repeatedly remind us about the necessity to place requirements on the load-bearing capacity of structural components. The common aim is to prevent the failure or fracture of materials and structures at the same time as we strive for more economic use. Hazardous situations do occur which unfortunately, from time to time, have catastrophic consequences. The assessment of some of the risks may be accomplished by fracture mechanics and there is a development towards practicing fracture mechanics as a common engineering tool.

The use of wood as a construction material often implies interference in the regular structure of the material. It is quite common that holes and notches must be made in structural members which may substantially reduce the load-bearing capacity. Environmental and time related effects as well as the design practice can severely affect the extent to which the capacity of the material may be used. Notches are often used at structural supports and connections which also suffer from different kind of stress concentrations due to drilling of holes or driving nails. The integration of a load-bearing system of a building with the non-structural systems for different kind of operations and service often implies conflicts where those systems intersect. One of the common solutions, and perhaps the only one in many cases, is to draw the operating and service system components (electric system, pipelines, ventiducts

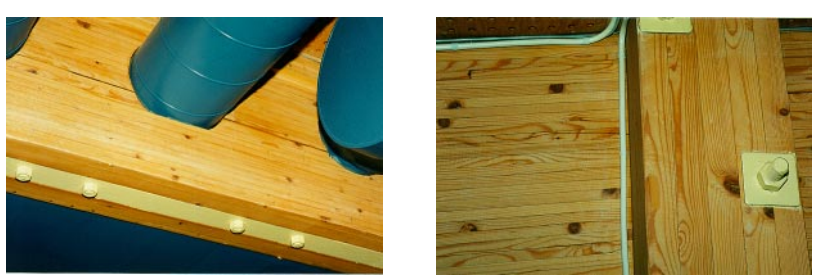

Figure 1.1: Intersection of a load-bearing system and an operating system.

etc.) through holes or notches in the load-bearing system as indicated in Figure (1.1). Geometric changes of cross-sections of load-bearing structures may also be of architectonic nature and due to economic aspects. This may imply an optimization in order to reduce the volume of building materials being used, resulting in cross-section variations of the structural members. The reduction of the load-bearing capacity is primarily due to stress concentration in critical regions, Figure (1.3). Conventional design methods rely normally on stress criteria, but according to linear elastic stress analysis the stresses may approach infinity close to a sharp corner of a hole or a notch. In such cases the necessity for another approach than the use of a stress criterion is obvious.

1.2 Some specific applications

Several application areas for wood and timber research can be mentioned where use is made of fracture mechanics, Figure (1.2). Some specific applications are listed below:

- Finger joints [32, 33]
- Arch of light weight beams [32]
- Notched beams [5, 27, 38]
- Wood composites [7]
- Structural joints [27, 37, 35, 14]
- Design codes [27]
- Splitting [27]
- Probabilistic fracture [27]
- Load duration [27, 38]
- Holes in structural members [27]
- Hangings [27]
- Cambered beams [27]
- Nail driving [27]
- Drying checks [27, 41]

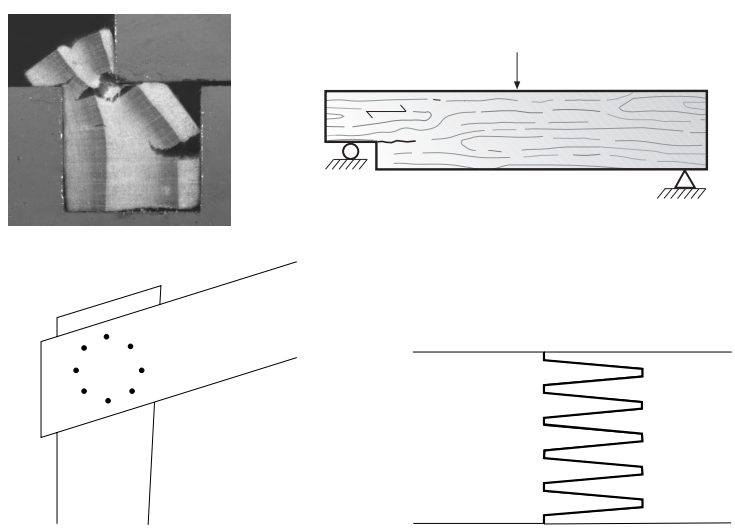

Figure 1.2: Applications of fracture mechanics

1.3 Scope and limitations

The main purpose of this report is to describe and study two methods for numerical analysis of the load-bearing capacity of structural members; one of linear elastic fracture mechanics (LEFM) and the other of non-linear fracture mechanics (NLFM). Several models may be used in strength design in relation to the risk of fracture in wood, see [4],[8] and [27]. One of the most promising numerical models in LEFM, according to the author, was dealt with by Petersson [8]. It is based on an energy approach and will be treated and applied in the following sections. It is often called the energy release rate approach, the compliance method or the virtual crack extension method.

Basic limiting assumptions adopted throughout this study are:

- the material outside the fracture process zone is linear elastic
- dynamics and inertia forces are neglected
- linear geometry
- no plasticity in the fracture region; only linear or non-linear elasticity

First some basic theory will be presented which is then applied on beams with cracks propagating in the longitudinal direction. This direction is assumed to coincide with the wooden grain direction. LEFM and NLFM formulations for determining

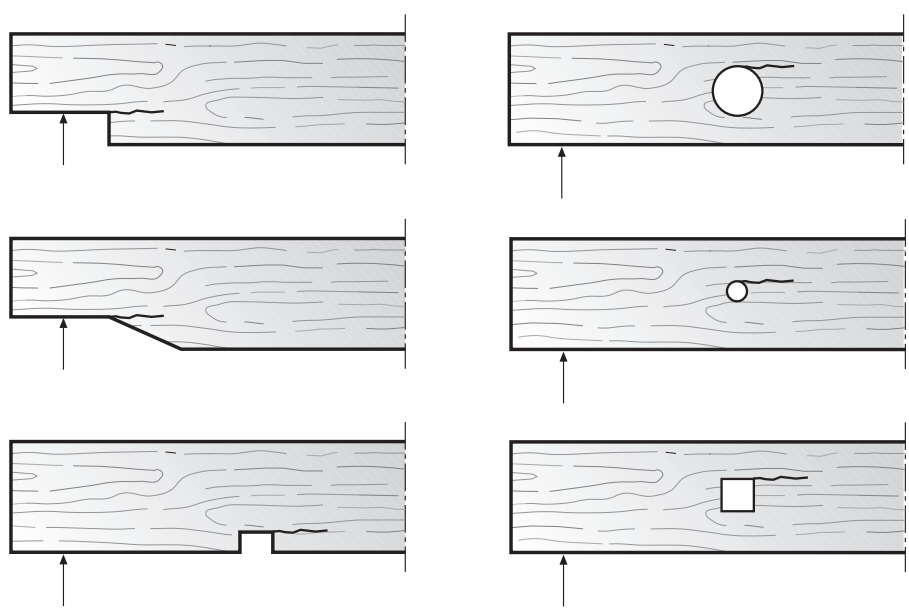

Figure 1.3: Studied types of beam structures

the crack load by finite element analysis are given and procedures for the numerical analysis are outlined. Results for some types of beams with a notch or a hole are presented and discussed. The wooden structural elements analyzed by LEFM are summarized in Figure (1.3). NLFM is applied to the end-notched beam and to a three-point bending specimen used for testing material properties. In addition to the computational studies, some material property and crack propagation test results are presented.

1.4 Disposition of the report

In Chapter 2 some constitutive properties of wood are reviewed with emphasis on orthotropic plane material properties. The three modes of fracture are introduced and the structural levels of wood with related properties are described.

The theories of linear and non-linear fracture mechanics are described in Chapter 3. From the theory of plane anisotropic elasticity, the stress functions for the stress field in the vicinity of a crack tip are derived in brief. Subsequently the methodology of the linear elastic approach is described. Several methods of non-linear fracture mechanics are mentioned and some numerical methods outlined.

Several test methods have been proposed for determining the fracture properties of wood and some of the methods are outlined in Chapter 4.

In chapter 5 the modelling of wood with linear elastic fracture mechanics is treated.

Modelling with non-linear fracture mechanics is described in Chapter 6, where the description is essentially focused on the fictious crack model (FCM).

In Chapter 7 the numerical studies are presented and the two methodologies of LEFM and NLFM are compared.

Finally,Chapter 8, comprises concluding remarks with discussion on design criteria and potential future research.

Chapter 2

Some constitutive properties of wood

2.1 General

A thorough understanding of the fracture properties of wood is the basis for modelling and the fracture process can be more easily comprehended with some basic knowledge of the different structural levels of wood. A short description follows with emphasis on the structural levels, the orthotropic properties and the constitutive properties of the fracture zone. Linear elastic fracture mechanics deals with the analysis of cracks by means of linear elastic theory. The region where the fracture process takes place is in that case regarded as infinitely small. The loading of a crack or a fracture plane is often divided into three modes. Mode I refers to a symmetric opening of the crack, mode II to shear and mode III to antisymmetric shear according to Figure (2.1). In the following sections mainly mode I and mode II will be discussed, including a combined action of mode I and II, termed as mixed mode.

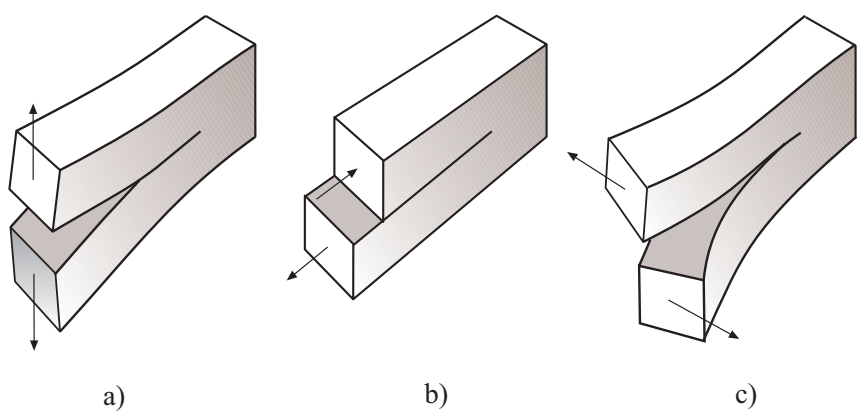

Figure 2.1: Loading and fracture modes (a) Mode I, (b) Mode II, (c) Mode III

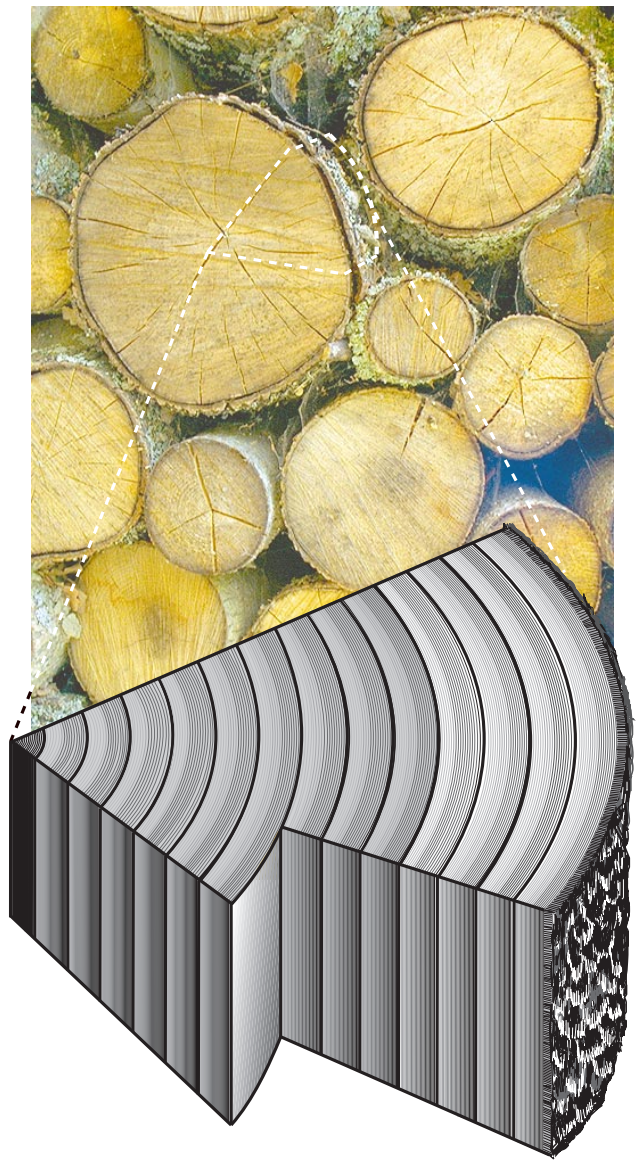

Figure 2.2: Principal structural features of a wood segment

2.2 Structural levels and related properties

Wood can be regarded as an orthotropic material. Different definitions of the constitutive properties can be given for different structural levels. Starting with the cross section of a tree trunk one detects the characteristic pattern of the annual rings, Figure (2.2). The annual rings, also termed as growth rings, develop through a difference in growth intensity during spring and summer. The light-colored earlywood that forms during the spring and early summer stands for the major part of the

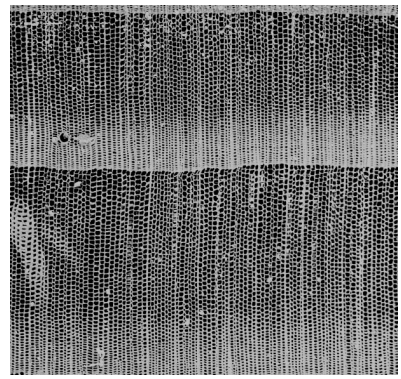

Figure 2.3: Annual rings [42] with an approximate width of 1.5mm and 2.0mm respectively

growth and is relatively porous and weak compared to the dark latewood, Figures (2.2) and (2.3). At this macroscopic level the material can be described as cylindrical orthotropic [22]. The next level is the annual ring, Figure (2.3), where we usually describe the constitutive properties as rectlinearly orthotropic. In engineering practice these first two levels are usually treated as transversely isotropic, i.e. no difference is made between the properties in the radial and the tangential directions [39]. The next structural level beyond the annual ring would be the individual cell or rather the cell wall which may be regarded as a composite material with its cell wall layers and a lignin layer between the cells constituting a gluing agent between the cells, Figures (2.4) and (2.5).

The constitutive properties are affected also by other structural variations. Among those is the existence of juvenile wood which comprises roughly the first twenty annual rings. The juvenile wood is characterized by lower strength and stiffness, but with higher shrinkage, Figure (2.6). The existence of knots and the forming of reaction wood affect also the properties of wood considerably. However, regarding fracture, knots have proven to have a reinforcing effect when oriented perpendicular to the fracture surface.

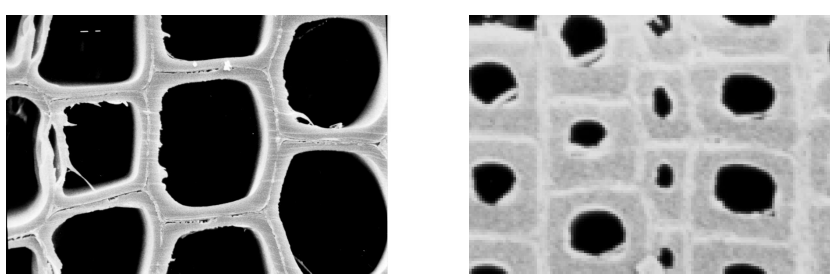

Figure 2.4: Cellular structure of softwood (Picea abies) [42]

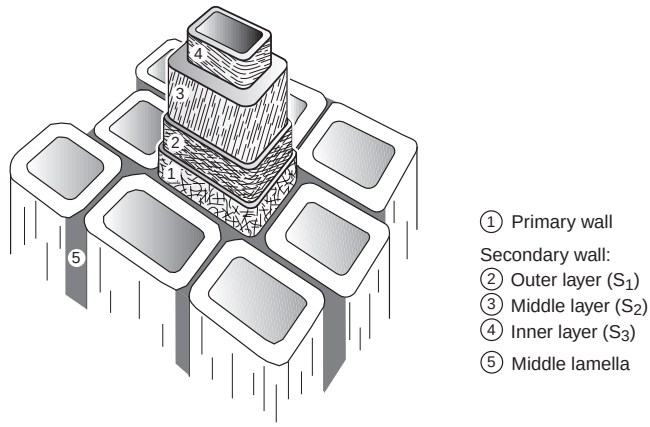

Figure 2.5: Composite structure of the cell wall

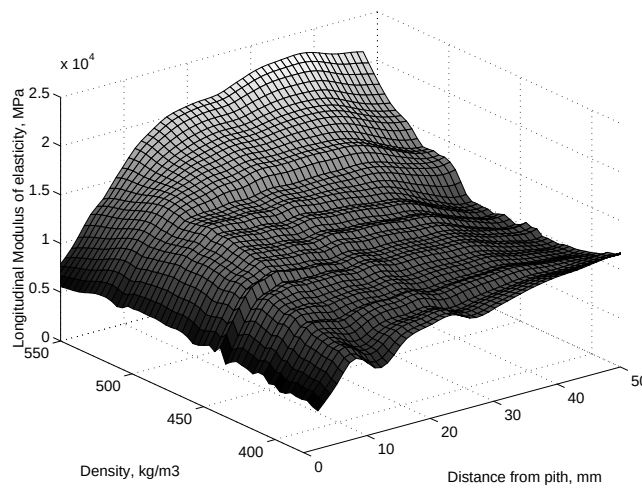

Figure 2.6: Measured variation of longitudinal modulus of elasticity with density and distance from pith [44]

2.3 Orthotropic elasticity

Although the computational results in this report will be dealing with two-dimensional models only, it is appropriate to review the relevant constitutive relations for a three-dimensional case. The constitutive relation for an in-plane state is simplest extracted from the three-dimensional constitutive expression for an orthotropic linear elastic medium, see for example [2] and [23].

Starting from

$$\begin{Bmatrix} \epsilon_{xx} \\ \epsilon_{yy} \\ \epsilon_{zz} \\ \gamma_{xy} \\ \gamma_{xz} \\ \gamma_{yz} \end{Bmatrix} = \begin{bmatrix} \frac{1}{E_{xx}} & \frac{-\nu_{yx}}{E_{yy}} & \frac{-\nu_{zx}}{E_{zz}} & 0 & 0 & 0 \\ \frac{-\nu_{xy}}{E_{xx}} & \frac{1}{E_{yy}} & \frac{-\nu_{zy}}{E_{zz}} & 0 & 0 & 0 \\ \frac{-\nu_{xz}}{E_{xx}} & \frac{-\nu_{yz}}{E_{yy}} & \frac{1}{E_{zz}} & 0 & 0 & 0 \\ 0 & 0 & 0 & \frac{1}{G_{xy}} & 0 & 0 \\ 0 & 0 & 0 & 0 & \frac{1}{G_{xz}} & 0 \\ 0 & 0 & 0 & 0 & 0 & \frac{1}{G_{yz}} \end{bmatrix} \begin{Bmatrix} \sigma_{xx} \\ \sigma_{yy} \\ \sigma_{zz} \\ \tau_{xy} \\ \tau_{xz} \\ \tau_{yz} \end{Bmatrix} \tag{2.1}$$

which for plane stress, i.e. for $\sigma_{\mathbf{zz}} = \tau_{\mathbf{xz}} = \tau_{\mathbf{yz}} = \mathbf{0}$, gives

$$\begin{Bmatrix} \epsilon_{xx} \\ \epsilon_{yy} \\ \gamma_{xy} \end{Bmatrix} = \begin{bmatrix} \frac{1}{E_{xx}} & \frac{-\nu_{yx}}{E_{yy}} & 0 \\ \frac{-\nu_{xy}}{E_{xx}} & \frac{1}{E_{yy}} & 0 \\ 0 & 0 & \frac{1}{G_{xy}} \end{bmatrix} \begin{Bmatrix} \sigma_{xx} \\ \sigma_{yy} \\ \tau_{xy} \end{Bmatrix} \tag{2.2}$$

which represents Hooke's law for an orthotropic material in a plane stress state if the planes of symmetry coincide with the coordinate axes. Written in a more compact form

$$\{\epsilon\} = [C]\,\{\sigma\} \tag{2.3}$$

The compliance matrix C is composed of the four independent parameters E_{xx}, E_{yy}, G_{xy} and ν_{xy}. Due to symmetry of $[C]$ the relation

$$\nu_{yx} = \nu_{xy}\frac{E_{yy}}{E_{xx}} \tag{2.4}$$

will hold. The inverse relation to Eq.(2.3) is

$$\{\sigma\} = [D]\,\{\epsilon\} \tag{2.5}$$

where D is the stiffness matrix. Written on matrix form the stiffness matrix for the plane stress state is

$$D = D_\sigma = \begin{bmatrix} \frac{E_{xx}}{(1-\nu_{xy}\nu_{yx})} & \frac{\nu_{yx}E_{xx}}{(1-\nu_{xy}\nu_{yx})} & 0 \\ \frac{\nu_{xy}E_{yy}}{(1-\nu_{xy}\nu_{yx})} & \frac{E_{yy}}{(1-\nu_{xy}\nu_{yx})} & 0 \\ 0 & 0 & G_{xy} \end{bmatrix} \tag{2.6}$$

and the strain ϵ_{zz} can be calculated form

$$\epsilon_{zz} = -\left(\frac{\nu_{xz}\sigma_{xx}}{E_{xx}} + \frac{\nu_{yz}\sigma_{yy}}{E_{yy}}\right) \tag{2.7}$$

Making use of the inverse of the compliance matrix in Eq.(2.1) and assuming that $\epsilon_{zz} = \gamma_{xz} = \gamma_{yz} = 0$ the stiffness matrix in a plane strain state appears as

$$D = D_\epsilon = \begin{bmatrix} \frac{E_{xx}(1-\nu_{yz}\nu_{zy})}{|T|} & \frac{E_{xx}(\nu_{yx}+\nu_{yz}\nu_{zx})}{|T|} & 0 \\ \frac{E_{yy}(\nu_{xy}+\nu_{xz}\nu_{zy})}{|T|} & \frac{E_{yy}(1-\nu_{zx}\nu_{xz})}{|T|} & 0 \\ 0 & 0 & G_{xy} \end{bmatrix} \tag{2.8}$$

where

$$|T| = 1 - 2\nu_{yx}\nu_{zy}\nu_{xz} - \nu_{xz}\nu_{zx} - \nu_{yz}\nu_{zy} - \nu_{xy}\nu_{yx} \tag{2.9}$$

The stress σ_{zz} becomes

$$\sigma_{zz} = \frac{E_{zz}}{|T|}\left(\left(\nu_{xz} + \nu_{xy}\nu_{yz}\right)\epsilon_{xx} + \left(\nu_{yz} + \nu_{xz}\nu_{yx}\right)\epsilon_{yy}\right) \tag{2.10}$$

2.4 Plane material properties

In order to study the difference between states of plane stress and plane strain, properties for a typical softwood species (Picea abies) is chosen for two different densities, $\rho = 390kg/m^3$ and $\rho = 430kg/m^3$, see Table (2.1).

The stiffness matrices, D_σ, for plane stress according to (Eq.(2.6)) and D_ϵ for plane strain according to Eq.(2.8)) are, respectively, for $\rho = 390kg/m^3$

	$\rho = 390kg/m^3$	$\rho = 430kg/m^3$
Moduli of elasticity	MPa	MPa
E_L	10700	13760
E_R	710	910
E_T	430	490
Moduli of rigidity	MPa	MPa
G_{LR}	500	510
G_{LT}	620	730
G_{TR}	23	30
Poisson's ratio		
ν_{LR}	0.380	0.452
ν_{RL}	0.030	0.030
ν_{LT}	0.510	0.536
ν_{TL}	0.025	0.019
ν_{RT}	0.510	0.559
ν_{TR}	0.310	0.301

Table 2.1: Elastic constants for different densities according to [15] and [21]

$$D_\sigma = \begin{bmatrix} 10823 & 299 & 0 \\ 299 & 718 & 0 \\ 0 & 0 & 500 \end{bmatrix} \quad D_\epsilon = \begin{bmatrix} 11145 & 520 & 0 \\ 520 & 867 & 0 \\ 0 & 0 & 500 \end{bmatrix} \tag{2.11}$$

and for $\rho = 430 kg/m^3$

$$D_\sigma = \begin{bmatrix} 13949 & 417 & 0 \\ 417 & 922 & 0 \\ 0 & 0 & 510 \end{bmatrix} \quad D_\epsilon = \begin{bmatrix} 14335 & 698 & 0 \\ 698 & 1128 & 0 \\ 0 & 0 & 510 \end{bmatrix} \tag{2.12}$$

In a simplified two-dimensional fracture mechanics analysis it is often necessary to choose between plane stress and plane strain. In reality the governing state is a mixture of these two states. Which one is dominating, depends primarily on the dimensions of the body being modelled [20]. However, for wood and the type of problems studied in this investigation a number of finite element calculations has shown that variations of the matrix element $D_{12} = D_{21}$ has very little influence on the overall results (the load-bearing capacity). Further, the variations of the stiffness properties for wood are substantial, Figure (2.7) and (??). These variations have substantially larger influence on the structural response than the choice of a proper stress or strain state.

In order to get a well-defined input for the numerical analysis a state of plane stress will be chosen. Further, no difference will be made between radial, tangential or a mixed radial-tangential direction for the in-plane analysis, only distinguishing between the fiber direction $\parallel$ and the transversal direction $\perp$. The stiffness parameters are selected in such a way that $E_\perp = \frac{E_\parallel}{30}$ and $G_{\parallel\perp} = \frac{E_\parallel}{16}$ as shown in Table (2.2).

The material matrix D, for plane stress, with values from Table (2.2) then becomes

$$D = \begin{bmatrix} 12069 & 169 & 0 \\ 169 & 402 & 0 \\ 0 & 0 & 750 \end{bmatrix} \tag{2.13}$$

The off-diagonal term $D_{12} = D_{21}$ in Eq.(2.13) seems quite small, but is probably a reasonable choice in practice if also the influence of rolling shear is to be considered to some extent (the y- and z axes do not coincide with the principal axes). Experimental results according to [6] clearly show that substantially lower values

Moduli of elasticity	MPa
$E_\parallel$	12000
$E_\perp$	400
Moduli of rigidity	MPa
$G_{\parallel\perp}$	750
Poisson's ratio	
$\nu_{\parallel\perp}$	0.41

Table 2.2: Elastic constants for FE-model

should be used for D_{12} and D_{22} than Eq.(2.11) and Eq.(2.12) indicate. For a more accurate analysis than a two-dimensional calculation can provide, a complete three-dimensional analysis must be performed considering the current orientation of the principal axes (longitudinal, radial and tangential axes) in each material point of the studied body.

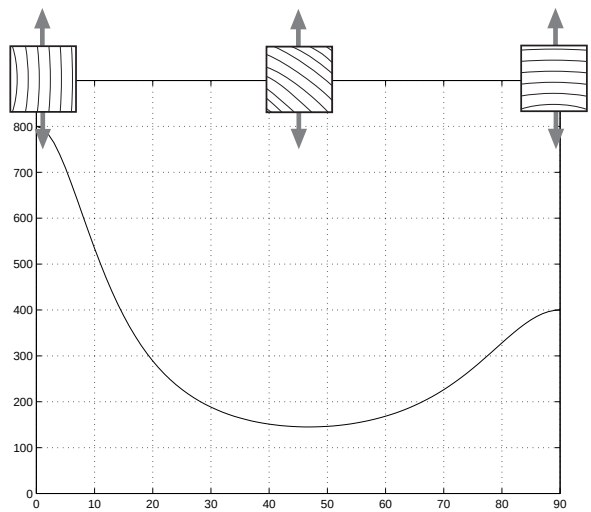

Figure 2.7: Variation of stiffness with orientation of annual rings (Vertical axis shows stiffness in MPa and the horizontal axis shows annual ring angle)

Chapter 3

Fracture Mechanics

3.1 General

The conventional methods for strength analysis by stress based criteria have limitations. The American Concrete Institute has argued for the use of fracture criteria instead of stress failure criteria using the following arguments [65]:

- **Energy requirement for crack growth**. The use of energy based criteria is needed due to the fact that crack propagation requires a certain amount of energy per unit crack extension.
- **Objectivity of load and response calculations**. The use of numerical methods has expanded continually since the early sixties. Different kind of models have been developed for fracture analysis. The experience seems to reveal a considerable element-size-dependency of the response (*This is not the experience in the present study*).
- **Lack of yield plateau**. For non-yielding materials the post-peak tension softening describes the propagation of a crack not including any yielding process of plastic deformations.
- **Energy absorbing capability and ductility**. A complete load-response curve, including the effects of post-peak tension softening, expresses the energy absorption of a body during the failure process. Apart from the recoverable elastic part the energy is absorbed by the fracture process. The size and form of the tension softening range is crucial for the structural behavior. The larger the post-peak range; the more energy is absorbed and the more ductile is the response. Energy absorbing characteristics cannot be indicated with stress limit analysis.
- **Size effect**. The size effect probably represents the most obvious advantage in using fracture mechanics analysis on structures, Figure (3.1). It is recognized on all levels of analysis; from laboratory testing to the full scale response of a structural member. The size effect reflects the variation of material strength with the size of tested body. Moreover, the post-peak response may also be greatly affected as the question of stability is concerned.

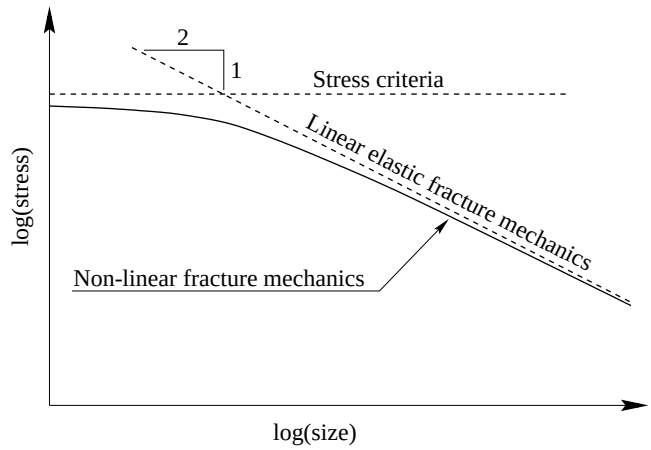

Figure 3.1: Principals of failure criteria and size effect prediction [65, 66]

When discussing fracture we may distinguish between two different fracture phenomena which both give rise to a similar structural performance. Fracture can be the result of either excessive yielding, also termed as plastic instability (necking) or simply due to the propagation of cracks. Still, fracture due to necking results normally in cracking caused by excessive stress concentrations in the neck. We often distinguish between ductile and brittle fracture, referring both to micro- and macrostructural level, Figure (3.2). Ductile behavior on the macrostructural level implies microstructural ductility which may also be the cause for globally brittle fracture. However, microstructural brittle fracture only gives rise to the analogous performance on the global basis. Wood, like many other materials, is frequently referred to as a quasi-brittle material meaning that these materials can fail by fracture but the extent of the fracture zone cannot be ignored. Besides this fact, wood is a strongly orthotropic and grain oriented material which entails almost completely predictable crack paths. Fracture involving crack paths aligned with the grain direction dissipates less energy than cross-grain fracture, Figure (3.3).

3.2 Fracture Models

Apart from the traditional definition of linear elastic fracture mechanics (LEFM) and non-linear fracture mechanics (NLFM) there exist models which may be regarded as a composition of both theories [8, 30, 55] where the assumed stress distribution is illustrated in Figure (3.4). The models applied in the subsequent chapters correspond to stress distribution of Figure (3.4 a) and b) respectively.

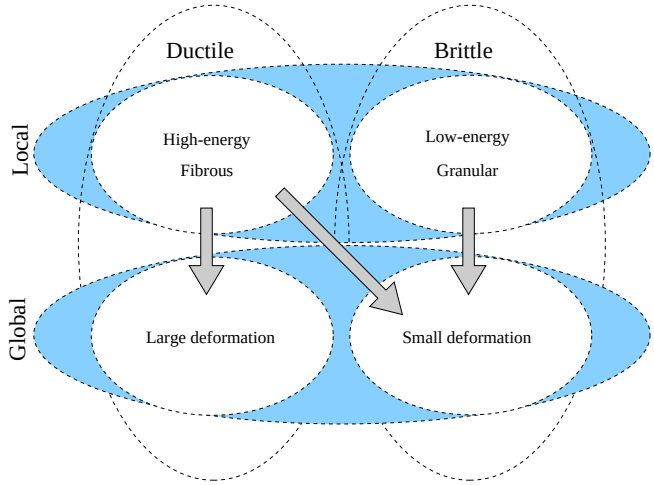

Figure 3.2: Concepts of the form of fracture (Modified after [16])

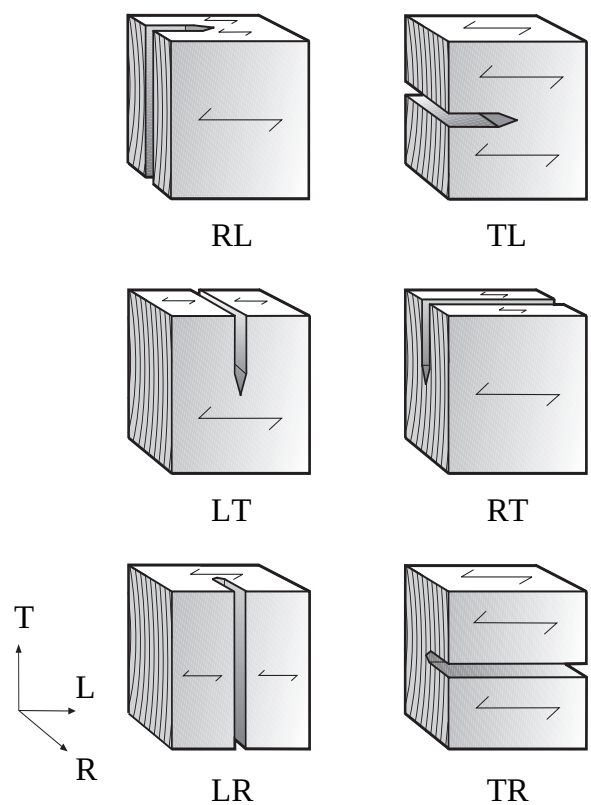

Figure 3.3: Orientation of crack paths

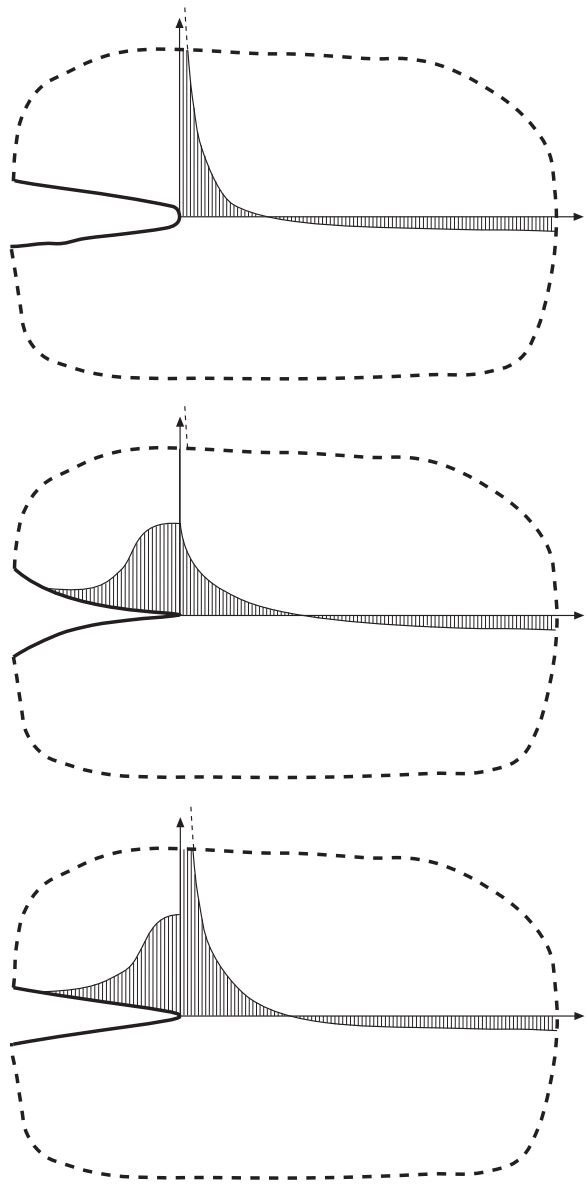

Figure 3.4: Stress distribution of the fracture models a) LEFM model, b) NLFM model, c) Non-linear cohesive crack model with singularity (Modified after [55])

3.3 Linear Elastic Fracture Mechanics

3.3.1 General

The basics of linear elastic fracture mechanics (LEFM) will be outlined in the subsequent sections. Due to the assumptions which make up the foundations of LEFM we are faced with the question to which extent the methodology is valid. The main

feature of LEFM is the stress singularity at the tip of a crack and accordingly the requirement of a prescribed crack. In other words, LEFM cannot be used to predict the occurrence of crack initiation. But if a crack exists in a body, LEFM can be a good tool for propagation analysis, provided that the size of the fracture process region is small compared to the length of the crack. The application of linear elastic theory implies neglecting possible yielding at both some remote point on the body in question and in the vicinity of the crack tip.

3.3.2 Energy release rate and fracture energy

The energy release rate $\mathcal{G}$ is also termed as the crack driving force. It is defined as the release of potential of the loads and elastic strain energy of the body for a crack extension of one unit area. Depending on the mode of action the energy release rate is often denoted as G_I, G_{II} or G_{III} respectively. When the energy release rate reaches a critical value, i.e. when crack propagation occurs

$$\mathcal{G} = G_c = 2\gamma \tag{3.1}$$

where γ is the surface energy density and G_c is termed as the critical energy release rate of the material. The energy release rate at mixed loading is obtained by summation.

$$\mathcal{G} = G_I + G_{II} + G_{III} \tag{3.2}$$

The principals of variations of energy terms is illustrated to some extent in Figure (3.5). The crack propagation criterion, i.e. $\mathcal{G} = G_c = 2\gamma$, can be identified by the

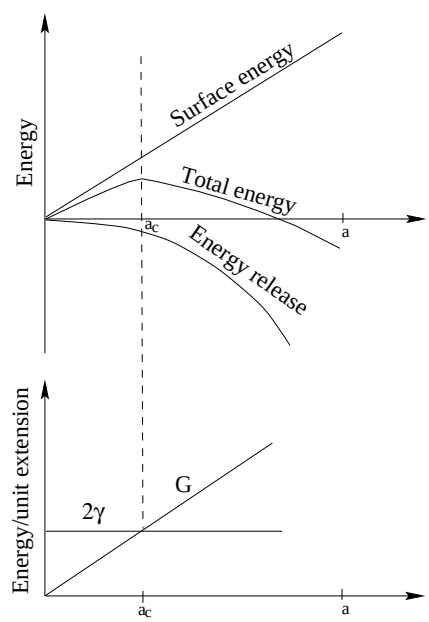

Figure 3.5: Schematic variations of energy parameters with crack extension (Modified after [53])

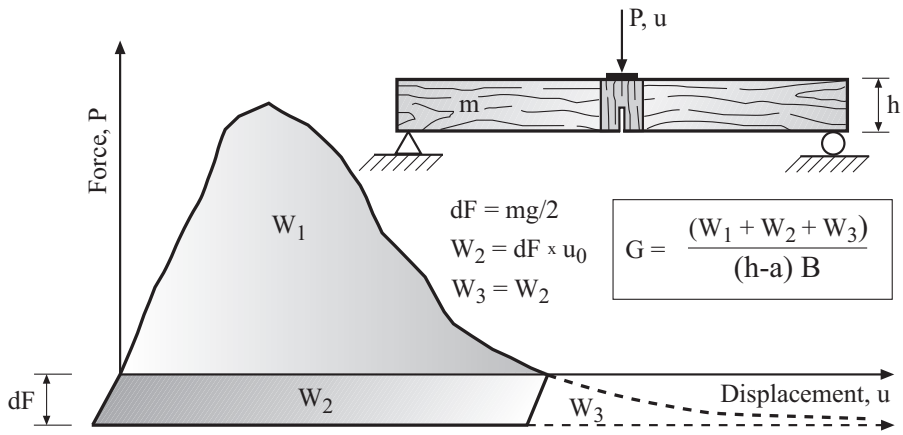

Figure 3.6: Evaluation of fracture energy from experimental testing

crack length a_c at the point of intersection or by the corresponding maximum point of the energy curve. The critical energy release rate should not be confused with the fracture energy, G_F although for certain conditions $\mathcal{G}_c = G_F$. The fracture energy, G_F, may be defined as the area below the $\sigma - \delta$ curve [31, 65], see Figure (3.6). This curve is determined from laboratory tests and G_F is frequently used as an input parameter in fracture mechanics models. The critical energy release rate , according to the definition above, may depend upon the geometry of the body as well as the load configuration. Furthermore, G_c may include other terms of energy dissipation than those emerging from crack propagation, such as limited plasticity at the crack tip. [53, 20, 65]. Then

$$2\gamma = 2\gamma_c + \gamma_p \tag{3.3}$$

where γ_c is the energy density of the fracture surface and γ_p is the plastic energy per unit crack extension. The definition of the critical energy release rate may thus seem to be rather conservative as it is taken for granted that all changes in stored energy of a body are due to dissipation of the fracture process. This assumption is true only for a body of elastic brittle material although it may be approximately true or acceptable for bodies with limited yielding in the vicinity of the crack tip [53, 46].

3.3.3 Stress intensity factors

A stress criterion for crack propagation (Appendix A) is often defined in terms of stress intensity factors, which depend on the geometry of the body and the load. Here, use is made of these stress intensity factors in deriving an expression for the energy release rate, G, in mixed mode as a function of the stresses in the vicinity of the crack.

Studying the case of a two-dimensional anisotropic elasticity, the equations of equilibrium, in the absence of body forces are [23]

$$\tilde{\nabla}^T \sigma = 0 \tag{3.4}$$

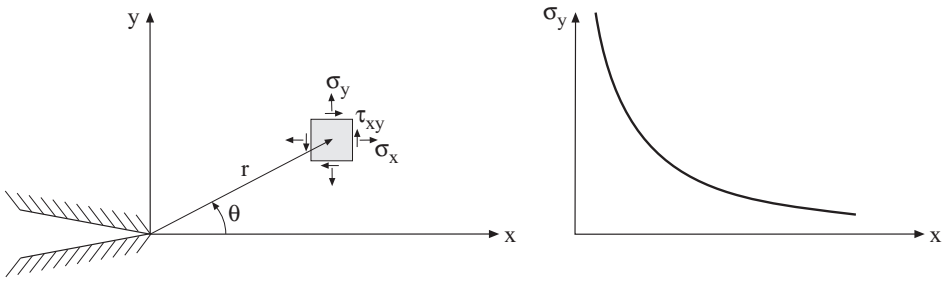

Figure 3.7: Stress distribution at the tip of a crack.

or written on component form

$$\begin{aligned} \frac{\partial \sigma_{xx}}{\partial x} + \frac{\partial \tau_{xy}}{\partial y} &= 0 \\ \frac{\partial \tau_{yx}}{\partial x} + \frac{\partial \sigma_{yy}}{\partial y} &= 0 \end{aligned} \tag{3.5}$$

where

$$\tau_{yx} = \tau_{xy} \tag{3.6}$$

From strain-displacement relationships a compatibility equation is derived as

$$\frac{\partial^2 \epsilon_{xx}}{\partial y^2} + \frac{\partial^2 \epsilon_{yy}}{\partial x^2} - \frac{\partial^2 \gamma_{xy}}{\partial x \partial y} = 0 \tag{3.7}$$

By introducing an Airy stress function Φ [22][24][25] where the stresses are defined as second derivatives of Φ, the equilibrium and compatibility equations can be satisfied exactly. The governing equation can be written as

$$c_{22}\frac{\partial^4 \Phi}{\partial x^4} - 2c_{23}\frac{\partial^4 \Phi}{\partial x^3 \partial y} + (2c_{12} + c_{33})\frac{\partial^4 \Phi}{\partial x^2 \partial y^2} - 2c_{13}\frac{\partial^4 \Phi}{\partial x \partial y^3} + c_{11}\frac{\partial^4 \Phi}{\partial y^4} = 0 \tag{3.8}$$

where c_{ij} are the components of the compliance matrix C, Eq.(2.3). The expression above can be simplified by using linear differential operators of the first order

$$D_k = \frac{\partial}{\partial y} - \mu_k \frac{\partial}{\partial x} \qquad\qquad k = 1, 2, 3, 4 \tag{3.9}$$

which applied on Eq.(2.18) gives

$$D_1 D_2 D_3 D_4 \Phi = 0 \tag{3.10}$$

The parameters μ_k appearing in the differential operator are the roots of the characteristic equation, being either complex or purely imaginary

$$c_{11}\mu^4 - 2c_{13}\mu^3 + (2c_{12} + c_{33})\mu^2 - 2c_{23}\mu + c_{22} = 0 \tag{3.11}$$

In an orthotropic plane state, the compliance components $c_{13} = c_{23} = 0$ which leads

to a further simplification of Eq. (3.11)

$$\mu^4 + \frac{(2c_{12} + c_{33})}{c_{11}}\mu^2 + \frac{c_{22}}{c_{11}} = 0 \tag{3.12}$$

which in the state of plane stress and plane strain takes the form

$$\mu^4 + (\frac{E_{xx}}{G_{xy}} - 2\nu_{xy})\mu^2 + \frac{E_{xx}}{E_{yy}} = 0 \tag{3.13}$$

and

$$\mu^4 + (\frac{E_{xx}}{G_{xy}}\frac{1}{1-\nu_{xz}\nu_{zx}} - 2\frac{E_{xx}}{E_{yy}}\frac{\nu_{yx}+\nu_{yz}\nu_{zx}}{1-\nu_{xz}\nu_{zx}})\mu^2 + \frac{E_{xx}}{E_{yy}} = 0 \tag{3.14}$$

respectively. A general solution of Eq.(3.8) with respect to the stress field in the vicinity of a crack tip is

$$\begin{aligned}
\sigma_{xx} &= 2\Re\left[\mu_1^2\Phi_1''(z_1) + \mu_2^2\Phi_2''(z_2)\right] \\
\sigma_{yy} &= 2\Re\left[\Phi_1''(z_1) + \Phi_2''(z_2)\right] \\
\tau_{xy} &= -2\Re\left[\mu_1\Phi_1''(z_1) + \mu_2\Phi_2''(z_2)\right]
\end{aligned} \tag{3.15}$$

where $\Re$ stands for the real part of the expression and $z_k = x + \mu_k\, y$, $(k = 1, 2)$ [24] with x and y being the Cartesian coordinates of a point close to the crack tip for which the stress is to be calculated, Figure (3.7). The functions Φ_1 and Φ_2 are defined in the transformed coordinate systems according to Figure (3.8), where the distance r_k to the point of interest in the transformed region is $r_k = r\sqrt{\cos(\theta) + \mu_k \sin(\theta)}$ By introducing a suitable form of the stress function and further variable substitutions,

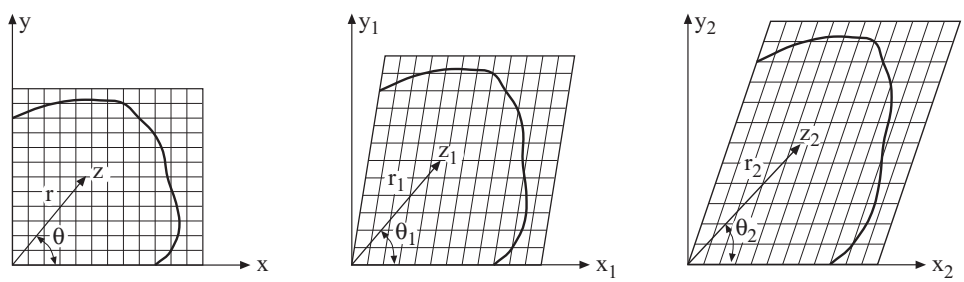

Figure 3.8: Notation of real space region and transformed regions.

the stress fields close to the crack tip can be expressed as

$$\begin{aligned}
\sigma_{xx} &= \frac{K_I}{\sqrt{2\pi r}}\Re\left[\frac{\mu_1\mu_2}{\mu_1-\mu_2}\left\{\frac{\mu_2}{\sqrt{\cos\theta+\mu_2\sin\theta}}-\frac{\mu_1}{\sqrt{\cos\theta+\mu_1\sin\theta}}\right\}\right] \\
&+ \frac{K_{II}}{\sqrt{2\pi r}}\Re\left[\frac{1}{\mu_1-\mu_2}\left\{\frac{\mu_2^2}{\sqrt{\cos\theta+\mu_2\sin\theta}}-\frac{\mu_1^2}{\sqrt{\cos\theta+\mu_1\sin\theta}}\right\}\right] \\
\sigma_{yy} &= \frac{K_I}{\sqrt{2\pi r}}\Re\left[\frac{1}{\mu_1-\mu_2}\left\{\frac{\mu_1}{\sqrt{\cos\theta+\mu_2\sin\theta}}-\frac{\mu_2}{\sqrt{\cos\theta+\mu_1\sin\theta}}\right\}\right] \\
&+ \frac{K_{II}}{\sqrt{2\pi r}}\Re\left[\frac{1}{\mu_1-\mu_2}\left\{\frac{1}{\sqrt{\cos\theta+\mu_2\sin\theta}}-\frac{1}{\sqrt{\cos\theta+\mu_1\sin\theta}}\right\}\right] \\
\tau_{xy} &= \frac{K_I}{\sqrt{2\pi r}}\Re\left[\frac{\mu_1\mu_2}{\mu_1-\mu_2}\left\{\frac{1}{\sqrt{\cos\theta+\mu_1\sin\theta}}-\frac{1}{\sqrt{\cos\theta+\mu_2\sin\theta}}\right\}\right] \\
&+ \frac{K_{II}}{\sqrt{2\pi r}}\Re\left[\frac{1}{\mu_1-\mu_2}\left\{\frac{\mu_1}{\sqrt{\cos\theta+\mu_1\sin\theta}}-\frac{\mu_2}{\sqrt{\cos\theta+\mu_2\sin\theta}}\right\}\right]
\end{aligned} \tag{3.16}$$

where K_I and K_{II} are the stress intensity factors for the stress and displacement fields near a crack tip according to the first two modes of fracture. Apart from the roots of the characteristic equation, μ_1 and μ_2, the expressions for σ_{xx}, σ_{yy} and τ_{xy} include the radial distance r from the crack tip and the angle θ from the direction of the crack, see Figure (3.7). These expressions can be written in a more compact form

$$\tilde{\sigma} = \tilde{\Theta}\tilde{\mathcal{K}} \tag{3.17}$$

where

$$\begin{aligned}
\tilde{\sigma}^T &= [\sigma_{xx} \quad \sigma_{yy} \quad \tau_{xy} \quad \tau_{yz}] \\
\tilde{\mathcal{K}}^T &= [K_I \quad K_{II} \quad K_{III}]
\end{aligned} \tag{3.18}$$

and

$$\tilde{\Theta} = \begin{bmatrix} \theta_{11} & \theta_{12} & \theta_{13} \\ \theta_{21} & \theta_{22} & \theta_{23} \\ \theta_{31} & \theta_{32} & \theta_{33} \\ \theta_{41} & \theta_{42} & \theta_{43} \end{bmatrix} \tag{3.19}$$

The last term, K_{III}, in Eq.(3.18) may be identified in appendix A, Eq.(A.36). The terms θ_{ij} are functions of the angle θ and the term $\frac{1}{\sqrt{2\pi r}}$. Furthermore, by identifying the elements in $\tilde{\Theta}$ which are equal to zero we get

$$\tilde{\Theta} = \begin{bmatrix} \theta_{11} & \theta_{12} & 0 \\ \theta_{21} & \theta_{22} & 0 \\ 0 & 0 & \theta_{33} \\ 0 & 0 & \theta_{43} \end{bmatrix} \tag{3.20}$$

In the case of isotropic material the equilibrium and compatibility conditions lead to the bi-harmonic equation

$$\Delta^2\Phi = \nabla^4\Phi = 0 \tag{3.21}$$

with the roots $\mu_1 = \mu_2 = i$. Thus, the expressions in Eq.(3.16) are obviously not applicable for isotropic materials and the special case of orthotropic materials when $\mu_1 = \mu_2 = \beta i$. The general solution for isotropic materials results in the following

expressions for the stress field in the xy-plane near the tip of the crack, see for example [1] and [16]

$$\begin{bmatrix} \sigma_{xx} \\ \sigma_{yy} \\ \tau_{xy} \end{bmatrix} = \frac{K_I}{\sqrt{2\pi r}} \cos\frac{\theta}{2} \begin{bmatrix} 1 - sin\frac{\theta}{2} sin\frac{3\theta}{2} \\ 1 + sin\frac{\theta}{2} sin\frac{3\theta}{2} \\ sin\frac{\theta}{2} cos\frac{3\theta}{2} \end{bmatrix} + \frac{K_{II}}{\sqrt{2\pi r}} \sin\frac{\theta}{2} \begin{bmatrix} -2 - cos\frac{\theta}{2} cos\frac{3\theta}{2} \\ cos\frac{\theta}{2} cos\frac{3\theta}{2} \\ cot\frac{\theta}{2} - cos\frac{\theta}{2} sin\frac{3\theta}{2} \end{bmatrix} \tag{3.22}$$

The stress intensity factors are are closely related to the energy release rate [24], G

$$G_i = \xi_i K_i^2 \qquad\qquad i = I, II \tag{3.23}$$

where the factors ξ_i for orthotropic plane state, with the geometric axes aligned with the principal axes of elasticity, are

$$\begin{aligned} \xi_I &= \frac{1}{E_I} = \sqrt{\frac{c_{11}c_{22}}{2}} \left[\sqrt{\frac{c_{22}}{c_{11}}} + \frac{2c_{12} + c_{33}}{2c_{11}} \right]^{1/2} \\ \xi_{II} &= \frac{1}{E_{II}} = \frac{c_{11}}{\sqrt{2}} \left[\sqrt{\frac{c_{22}}{c_{11}}} + \frac{2c_{12} + c_{33}}{2c_{11}} \right]^{1/2} \end{aligned} \tag{3.24}$$

3.3.4 Mixed mode failure criterion

The values of the stress intensity factors K_I and K_{II} depend on the load case, the geometry and the boundary conditions. In pure mode I or pure mode II fracture is assumed to take place when either $K_I = K_{Ic}$ or $K_{II} = K_{IIc}$, where K_{Ic} and K_{IIc} are material parameters. In order to determine the critical load in mixed mode one often uses empirical expressions, such as

$$\left(\frac{K_I}{K_{Ic}}\right)^m + \left(\frac{K_{II}}{K_{IIc}}\right)^n = 1 \tag{3.25}$$

where m=1 and n=2 has been suggested for wood by Wu [28]. In order to find a reasonable relation between G_c and the stress ratio at the crack tip $\bar{\sigma}_\perp/\bar{\tau}$ we may start from a case illustrated in Figure (3.9). According to Eq.(3.16) we may approximate

$$\frac{\bar{\sigma}}{\bar{\tau}} \approx \lim_{\theta \to 0} \frac{\sigma_{yy}}{\tau_{xy}} \approx \frac{K_I}{K_{II}} \tag{3.26}$$

where the stress intensity factors K_I and K_{II} can be related to elasticity and fracture parameters [16][25][26].

We have

$$K_I = \sqrt{E_I G_I} \tag{3.27}$$

$$K_{II} = \sqrt{E_{II} G_{II}} \tag{3.28}$$

and, referring to Figure (3.9),

$$\frac{E_I}{E_{II}} = \sqrt{\frac{E_y}{E_x}} = \sqrt{\frac{E_\perp}{E_\parallel}} \tag{3.29}$$

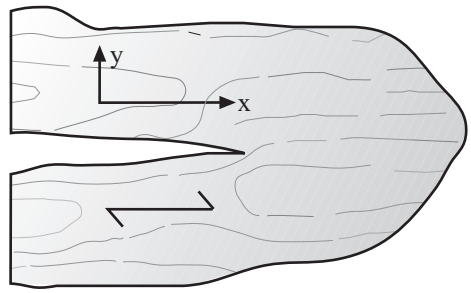

Figure 3.9: Crack propagation in grain direction.

where $E_\perp$ and $E_\parallel$ are the elasticity moduli perpendicular to and parallel with the grain direction. By use of Wu's suggestion [28] based on the stress intensity factor approach, Eq.(3.27) and (3.28), the fracture energy G_c in a mixed mode

$$G_c = G_I + G_{II} \tag{3.30}$$

is assumed to be related to the fracture energy in pure mode I (G_{cI}) and pure mode II (G_{cII}) as

$$\frac{\sqrt{G_I}}{\sqrt{G_{Ic}}} + \frac{G_{II}}{G_{IIc}} = 1 \tag{3.31}$$

According to Eq.(3.25) and (3.26) and after some manipulations of Eq.(3.27) to (3.31) we get

$$G_c = \frac{1}{a}\left[1 + \frac{b^2}{2a}(1 - \sqrt{1 + \frac{4a}{b^2}})\right] \tag{3.32}$$

where

$$a = \frac{1-\kappa^2}{G_{IIc}} \tag{3.33}$$

$$b^2 = \frac{\kappa}{G_{Ic}} \tag{3.34}$$

and

$$\kappa^2 = \frac{1}{1 + \sqrt{\frac{E_\perp}{E_\parallel}}\left(\frac{\bar{\tau}}{\bar{\sigma}}\right)^2} \tag{3.35}$$

This expression, Eq.(3.32), will be used subsequently in FE-computations for the fracture energy G_c in mixed mode.

3.3.5 Stress fields in the vicinity of singularities

The analytical solution, according to Lekhnitskii [22], for an elastic stress field in the vicinity of a crack is presented in Eq.(3.16). Several other formulations have been developed where the one suggested by Williams [57] has also gained some interest. Williams approach is, due to its simplicity and being formulated as an eigenvalue

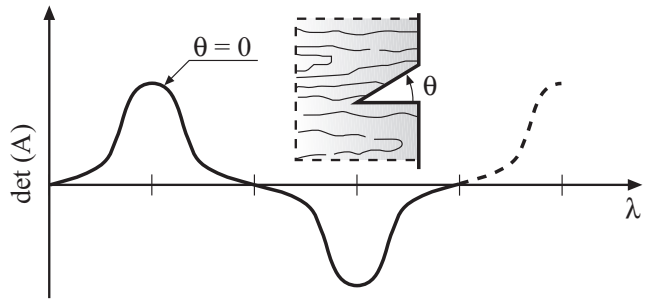

Figure 3.10: Linear-elastic eigenvalue analysis of stress fields (Modified from [58])

problem, quite suitable for numerical procedures [58, 16, 59, 7]. A common principal feature in the eigenvalue formulations is the assumed stress function

$$\Phi = Ar^{\lambda}F(\theta, \lambda) \tag{3.36}$$

where A is an arbitrary constant, r and θ are polar coordinates and λ is an resulting in solutions for the stress field on the form

$$[\sigma_r, \sigma_\theta, \sigma_{r\theta}] = A\mathcal{F}(F(\theta), F'(\theta), F''(\theta), \lambda) \tag{3.37}$$

With appropriate boundary conditions Eq.(3.37) may be used to define an eigenequation

$$\mathbf{A}\alpha = \mathbf{0} \tag{3.38}$$

which is solved for λ.

3.3.6 Quasi-brittle fracture

A quasi-brittle material may be defined as a material which reflects negligible or at the most moderate strain hardening prior to the ultimate tensile stress followed by a descending tension softening branch, Figure (3.11). The material is linear to begin

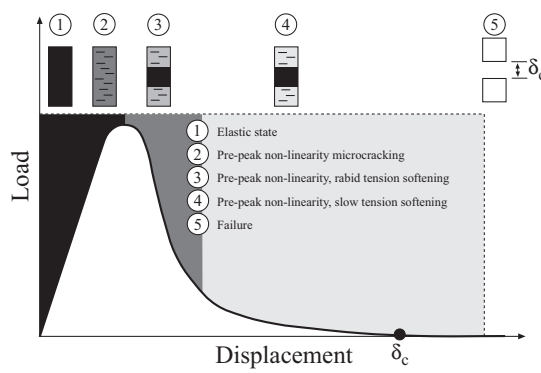

Figure 3.11: Load-deflection response of a quasi-brittle material

with but due to the occurrence of micro-cracks or small scale yielding it develops a non-linear response up to the level of ultimate tensile strength. From now on the micro-cracks or the plastic deformations develop very fast and a primary crack or necking forms successively with the corresponding loss of load-bearing capacity as a consequence. Quasi-brittle global response may be defined with analogous restrictions, i.e. the potential forming of multiple cracks or excessive plastic deformations which eventually cause a global failure or instability.

3.4 Fracture Mechanisms in Wood

3.4.1 Fracture process zone

When wood is subjected to tensile loading the nominal strength is dependent upon the existence of defects in the material. What normally is considered as defects are, for example, knots; reaction wood and visible cracks which may have formed either due to drying [67, 62, 41] or the application of load [5, 4, 9, 10]. When a wooden structure is subjected to a load it may suffer from extensive stress concentrations due to singularities. These singularities may, for instance, be pre-existing cracks or notches, Figure (3.12). If we have a close look at a crack in clear wood [42] we may notice the crack bridging fibers which still maintain some stiffness in the fractured area, Figure (3.14). Just before the ultimate load the material can be almost intact, i.e. no severe cracking has taken place. Micro-cracks may have started to form but when passing the point of ultimate load the cracking increases substantially and the crack successively develops. Materials like wood which exhibit moderate local micro-cracking effects and very little plastic yield, prior to ultimate load, may be defined as quasi-brittle where the fracture process zone practically occupies the entire non-linear region, Figure (3.13). The fracture process zone is assumed to consist of a micro-cracking zone, in front of the crack tip, and a primary cracking zone with bridging wood fibers between the adjacent crack surfaces. The size of the fracture process zone, ℓ_p, is of major interest but is not easy to determine. Another parameter of similar order, the material characteristic length, ℓ_{ch}, may be used for crude estimation of the process zone length.

$$\ell_p \sim \ell_{ch} = \frac{E_\perp G_F}{f_t^2} \tag{3.39}$$

Figure 3.12: Stress concentration in a structural member

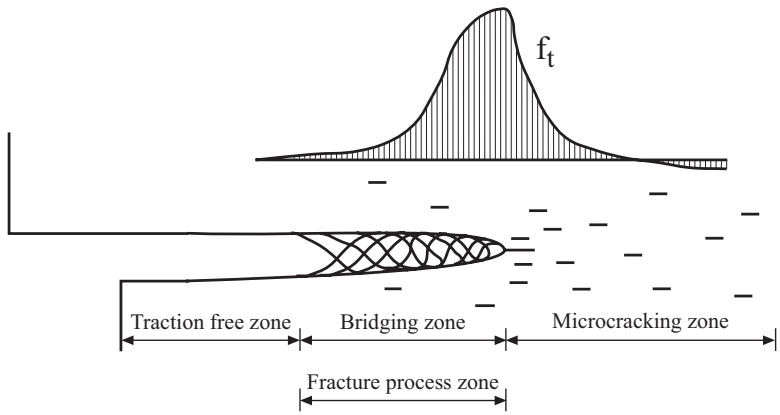

Figure 3.13: Fracture process zone

Typical values of ℓ_{ch} are in the interval 5-15 mm and for mode I propagation of RL and TL cracks, Figure (3.3), ℓ_p can be about $1.5\ell_{ch}$ [5]. Hillerborg (1983) proposed the ratio $\frac{d}{\ell_{ch}}$ as a dimensionless parameter (brittleness number) where some characteristic size, d, of a structural member is related to material properties, $E_\perp, G_F, f_t$. This has proved to be useful in presenting results in form of general dimensionless diagrams. The brittleness number also appears in the literature on a reciprocal form $\frac{\ell_{ch}}{d}$.

3.4.2 Tensile softening models

The material properties needed for modelling of wood with a proper crack model can be obtained from stable experimental test results. An example of such results is illustrated in Figure (3.15). A specimen is loaded in uniaxial tension. The initial response is linear elastic, i.e. the deformations are assumed to be uniformly distributed along the whole length of the specimen which in turn allows the strain to be written as

$$\epsilon = \frac{\Delta\ell}{\ell} \tag{3.40}$$

Beyond the linear elastic limit the material exhibits non-linear behavior which up to the attainment of ultimate tensile capacity is primarily due to development of micro-cracks. Plastic deformations and material defects may also contribute to this non-linear behavior. The strain softening response, when the load carrying capacity passes the ultimate strength, is characterized by increase in deformations accompanied with decrease in strength. When the load is about to pass the ultimate tensile strength a so called fictious localized fracture zone is assumed to develop across the entire cross section. At this point, increasing elongation, $\Delta\ell$, of the specimen results in branching of the load-deformation response where the material in the fracture process zone follows the strain softening branch and the material outside the fracture zone follows the unloading branch. The total elongation of the specimen may thus be given by

$$\Delta\ell = \epsilon\ell + \delta \tag{3.41}$$

The first term in the expression, $\epsilon\ell$, represents the elastic response and the second one, δ, the crack opening displacement. Due to the branching of the load-deformation curve the material properties are expressed with two separate relations representing the mechanical properties of the material. This is very convenient in

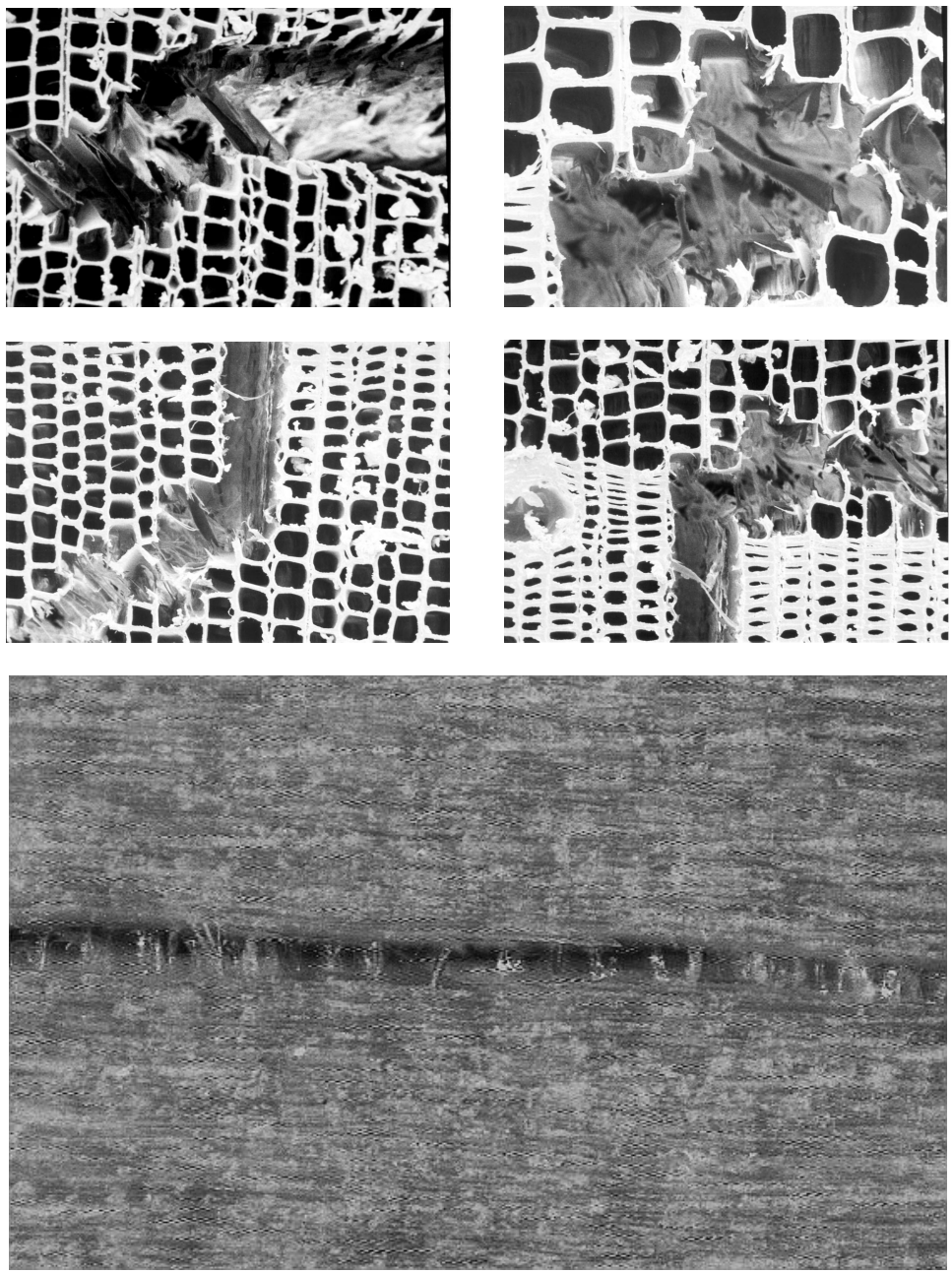

Figure 3.14: Fracture in clear wood

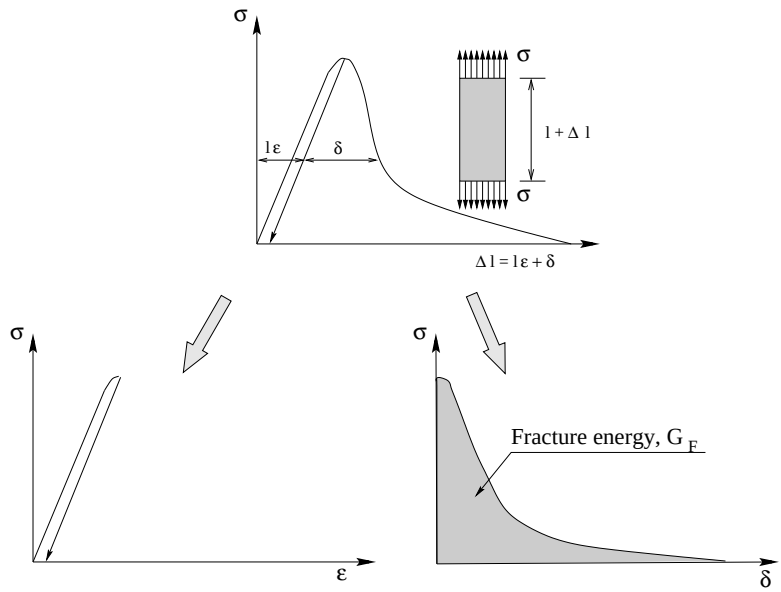

Figure 3.15: Characteristics of a stable tensile fracture test

the case of modelling fracture with the fictious crack model (FCM). The elastic response is represented with a $\sigma - \epsilon$ relation while the fracture and separation of the crack surfaces is represented with a $\sigma - \delta$ relation.

3.4.3 Crack paths

If we take a close look at Figure (3.3) we may identify six potential crack paths in the principal material directions. The attainment of fracture mechanics material data has been restricted to these orientations to a large extent. In fact the LR and LT directions have hardly been investigated at all. Normally we make no difference between the fracture energy in cracks with the same orientation of crack surfaces, i.e. $G_{TL} = G_{TR}$, $G_{RL} = G_{RT}$ and $G_{LR} = G_{LT}$. At least we have not been able to determine any significant difference with the present-day methods. Crack paths in wood initially run according to the orientation of the singularity (initial crack) or defect causing the fracture. Shortly after a crack has begun to develop, and sometimes almost instantaneously, the crack has a tendency to adjust to the principal orthotropic directions of the material, Figure (3.16). This is not surprising, given the variation in density in a growth ring. The crack path tends to follow low-density material where it propagates more easily, Figure (3.14) and Figure (3.16).

3.4.4 Environmental influence on material parameters

The environmental influence on the material properties is often neglected in fracture analysis. Environmental influence is used here to mean the influence of moisture and temperature. Moisture variations in wood are a major cause for internal stresses

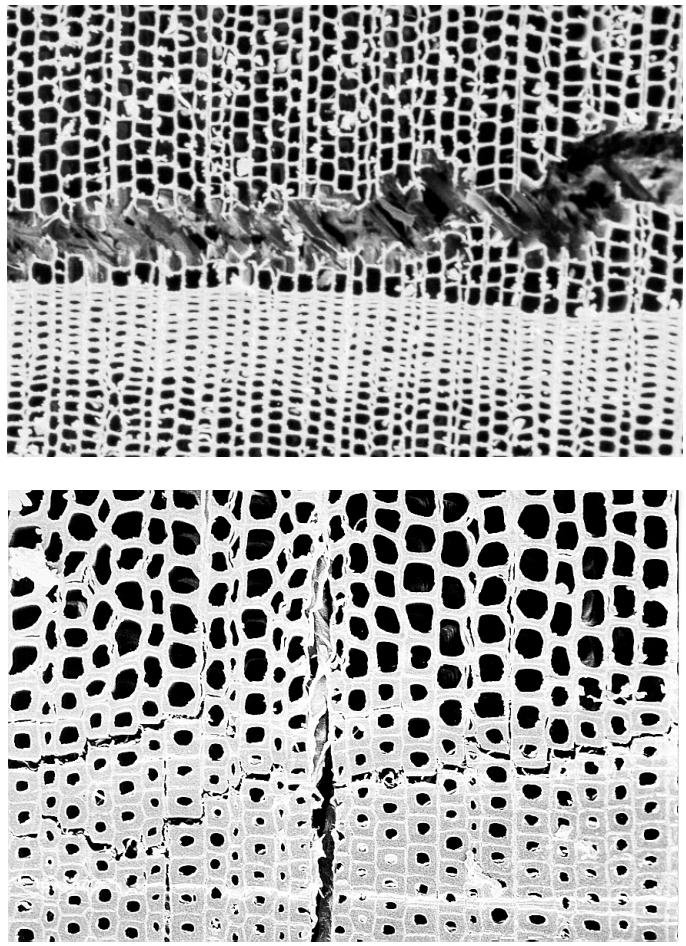

Figure 3.16: Example of possible crack paths, a) parallel with annual rings b) perpendicular to annual rings

due to its hygroscopic properties [67, 68, 62, 69, 41]. When discussing wood drying one may perhaps distinguish between the drying from a green state to what we experience as "normal" dry wood, often in the vicinity of 10% - 20%MC, and the seasonal variations caused by climatic changes. There can be dramatic changes in stresses when wood is subjected to process drying and those changes are traced to the shrinking [41], which can be large when the moisture content decreases below the fibre saturation point. The properties of the main chemical constituents of wood, i.e. lignin, hemicellulose and cellulose are decisive for the macroscopic shrinkage properties. Furthermore, the variations in microfibril angle of wood [42, 44] have considerable influence on the shrinkage and its anisotropy. Experience shows that cracks tend to occur in wood as the moisture content decreases. As the moisture distribution in a log is initially uneven there may be an almost immediate shrinking in the heartwood, but delayed shrinking in the sapwood. The process which results in shrinking variations in the material, along with the material anisotropy, are the

basis for the development of internal stresses. When the stresses have reached the strength of the material, cracks start to develop and as the shrinkage properties depend, to some extent, on the stress level we may experience an indirect fracture effect on the shrinkage properties due to stress relaxation in the fracture process. The long-term effects of climatic variations on the material properties of wood are still a matter of investigation. The intensive research on the microscopic level may reveal the effects and generate knowledge applicable to the engineering practice. The effects found at microscopic or material level, projected on structural members, give rise to the question whether the size effect and duration of load are coupled in some way through climate variations.

3.5 Non-Linear Fracture Mechanics

3.5.1 General

Non-linear fracture mechanics (NLFM) is defined here as the theory of fracture mechanics which takes into account the non-linear material behavior in the fracture process zone (see subsection 3.4.1, page 25). This behavior may be either a pure fracture process or localized plastic yielding or a mixture of both.

3.5.2 Cohesive crack models

For the purpose of implementation in numerical procedures we are first of all faced with the choice of modelling the fracture either with a discrete pre-assumed crack or a continuum model. The present study will focus entirely on discrete cracks with a prescribed propagation path. The fictious crack model, FCM, will be utilized in the theory and the subsequent computations. The fictious crack model was presented by Hillerborg [30] for modelling crack propagation in concrete and it has been utilized successfully by many since then, see for instance Modéer [30], Gustafsson [5], Boström [62] and Wernersson [32].

The first attempt to model the stress state in a cohesive fracture process zone was made in the late fifties by Barenblatt, who introduced a smoothly closing crack, Figure (3.17), where forces act on a zone (fracture process zone) near the crack tip. The main drawback of Barenblatt's model is that the distribution of the cohesive forces is usually unknown. A closely related model referred to as the Dugdale model (1960) is based on similar configuration of the fracture zone, apart from the distribution of traction forces, σ_y, in the fracture process zone which are considered to be constant, Figure (3.17). Both models imply the same kind of geometric configuration of the crack tip, i.e. smoothly closing crack faces which in turn implies that the stresses are finite. The fact that we have finite stresses in front of the crack tip makes the stress concentrations vanish and the Irwin theory of brittle fracture is no longer applicable (see subsection 3.3.2 and appendix A.4).

$$K_i = 0 \qquad i = I, II, III \tag{3.42}$$

The zero stress intensity implies that we have entered the category of non-linear fracture mechanics. The fictious crack model (FCM) is a widely used model. It differs

from Barenblatt's and Dugdale's models, primarily due to assumptions concerning the stress distribution in the fracture process zone, Figure (3.13). In the FCM there is no pre-assumed stress distribution in the fracture process zone. Instead, we apply a constitutive relation in the fracture zone which is extracted from a stable tensile test, Figure (3.15), or a three point bending test, Figure (3.6). When the maximum stress has been reached in the material all further deformations within the fracture zone result in increased damage and decreasing traction forces. Simultaneously the non-fractured part of the material outside the fracture zone is unloaded. The fracture successively localizes in a narrow band or zone. This zone is the one referred to as a fictious crack, i.e. stress transferring crack. We simply assume a prescribed crack path and adopt appropriate stress-widening rules for the separation of the crack faces. A closely related method, the crack band method (CBM), was proposed by Bažant and Oh (1983). The primary difference is the assumption that the fracture process is distributed on a certain width, i.e. we do not have a discrete crack, but a narrow band with distributed fracture properties. Both models have their origin in fracture modelling of concrete.

Invariant integrals have played an important role in both elastic and elastic-plastic

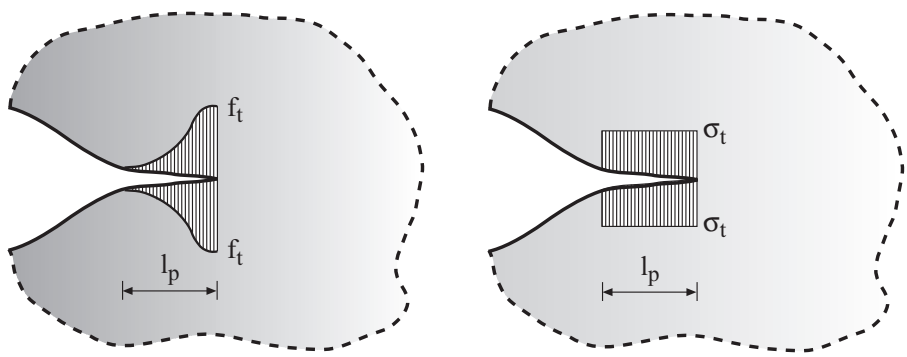

Figure 3.17: Cohesive crack models, a) Barenblatt's model b) Dugdale's model

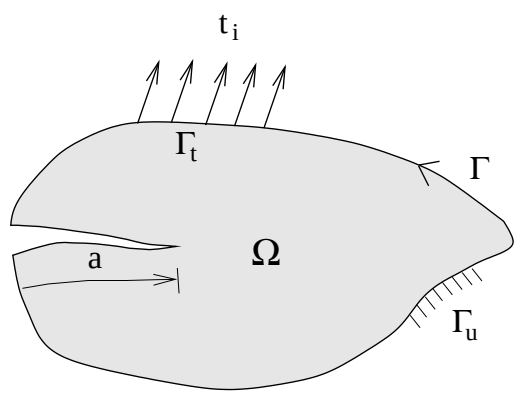

Figure 3.18: A plane, cracked region of non-linear elastic material

fracture mechanics. Rice (1968) adopted the J-integral in fracture mechanics. It may be interpreted as a generalisation of the energy release rate, **G**, for non-linear elasticity. If we disregard the body forces, the potential energy of a body may be expressed as

$$\Pi = \int_{\Omega} W d\Omega - \oint_{\Gamma_t} t_i u_i d\Gamma \tag{3.43}$$

where **W** is the strain energy density of a body on the domain Ω and Γ_t is the boundary of the body with traction forces t_i and the displacements u_i, Figure (3.18). By differentiating Eq.(3.44) with respect to the crack length, **a**, we obtain

$$\frac{d\Pi}{da} = \int_{\Omega} \frac{dW}{da} d\Omega - \oint_{\Gamma} t_i \frac{du_i}{da} d\Gamma \tag{3.44}$$

or

$$-\frac{d\Pi}{da} = \oint_{\Gamma} \left(W n_x - t_i \frac{du_i}{da} \right) d\Gamma \tag{3.45}$$

The right hand side of Eq.(3.45) is identical with Rice's definition of the J-integral and thus we arrive at

$$J = -\frac{d\Pi}{da} \tag{3.46}$$

which makes the J-integral identical with the energy release rate, **G**, in the case of linear elasticity. Equation (3.46) reveals that the J-integral may be determined experimentally as the change in potential energy of two similar bodies with a slight difference in crack lengths [60].

3.5.3 Some alternative methods of non-linear fracture modelling

Dahlblom [54] developed a smeared crack model by utilizing the fictious crack model. By introducing a parameter termed as the equivalent element length; implying the effect of crack shearing and unloading a fictious crack model evolved, free of one of the main drawbacks of the original FCM which is the predefinition of the crack path. Petersson [10] established yet another version of the fictious crack model or rather the crack band model. This method presumes a prescribed crack path with a band of continuum crack elements. The solution algorithm is based on an eigenvalue analysis of the negative stiffness in the fracture process zone, Section (6.3). A quite different FE approch is the one presented by Tryding [71] who studied the in-plane failure of paper by means of two continuum models which both are formulated as a plasticity problem. Another FE plasticity approach was studied by Cannmo [72] who implemented an interface model, based on plasticity and damage, in FE code. In his study, Schellecens [29] dealt with a formulation of solution strategies for composite structures where he came up with an approach for both interface and continuum models formulated as FE plasticity problems.

3.6 Numerical Methods

The most widely used methods are the finite difference method (FDM), the finite element method (FEM), the boundary element method (BEM) and the dual boundary element method (DBEM). Each of these methods are to be preferred in different

situations. An example of the use of finite difference method is the two-dimensional crack path study of Hori et.al. [19]. The FE method is probably the most common numerical method used in mechanics context, including fracture mechanics. The boundary element method (BEM) is growing as a numerical method within many fields of engineering. It is based on an element discretisation, but different from the FEM it is made on the boundary only. This means that the solution domain within the boundary is solved exactly. The method is considered to be very accurate but the need for analytic solution of the inner domain may sometimes be considered as a serious drawback. The BEM is more or less regarded as a complement to the FEM. Its growing popularity in the field of fracture mechanics is partly due to the simplicity of modelling the fracture process zone in the non-linear case. The DBEM is a sort of a mixed formulation version of the BEM applied primarily to fracture problems. Its main features lie in the use of a displacement boundary integral equation on one part of the fracturing surface and a traction boundary integral equation on the other. This method has the advantage ahead of the BEM that no subsequent re-meshing is needed as the crack propagates.

Chapter 4

Experimental Determination of Fracture Properties

4.1 Introduction

Various methods have emerged for evaluating fracture energy of clear wood or for establishing constitutive relations. Some methods of evaluating fracture parameters for wood will be mentioned here briefly and experimental results are presented from a series of tests which were carried out at the laboratories of Lund Institute of Technology in 1993. For establishing mode I fracture energy values of clear wood we have to rely mainly on two methods of testing; a simple tensile test, referred to as the Compact Tension test (CT) and the tree point bending test (TPB). The CT test has been discussed by Boström [62] and the TPB test by Larsen and Gustafsson [52]. Furthermore, Boström [61] has worked on developing a fracture energy test for shear parallel with grain.

4.2 Tensile tests, mode I

4.2.1 The Compact Tension test

The tensile fracture toughness test is probably the most simple one of fracture testing methods applied for wood. Originally applied to metals and later to concrete it has also been frequently used for evaluating fracture properties of wood. Apart from being simple in performance it does not require large quantities of material for the testing. The geometry of the CT specimen according to ASTM (1981) is illustrated in Figure (4.1). The load is applied to the specimen with a displacement controlled testing machine, either by directly pulling the two cantilever beams apart or by driving a wedge in the crack direction between bearings attached to the specimen. The CT test was investigated to some extent by Boström [62] where he performed a FE analysis on the CTS in order to determine the error of the geometry function Y in the expression $K_{IC} = Y P_{max}\sqrt{a}/(bh)$ which is derived for isotropic material. The error was estimated to $K_{IC,iso}/K_{IC,ortho} \approx 1.07$. According to ASTM the geometry expression is valid only in the interval of $0.45 < a/h < 0.55$, on the form presented here, but Hillemeier and Hilsdorf [65] have modified it to be valid for $0.125 < a/h < 0.925$ so the CTS should be applicable to wide range of crack lengths, a.

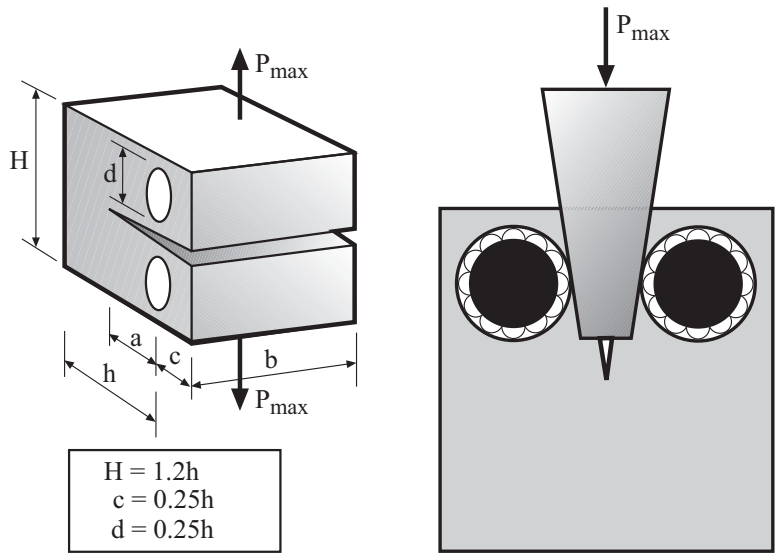

Figure 4.1: Compact Tension Specimen (CTS) a) Geometry according to ASTM (1981) b) Wedge loaded CTS

Boström however, found out in his theoretical study of the CT test that the material characteristic length needed to be $\ell_{ch} \leq (h-a)/3$, in order to attain fracture energy values fairly accurate for use in linear elastic computations. With ℓ_{ch} in the vicinity of $5-20$ mm we may be expecting a ligament size in the interval of $15-60$ mm and thus a specimen size up to 150 mm, given that the initial notch is approximately of the same size as the ligament, i.e. $h \approx 2a$. This potential restriction on specimen size may be difficult to comply with in order to attain a representative clear wood specimen.

4.2.2 The Three-Point Bending test

The tensile fracture energy test, based on three point bending, is probably the most reliable one, at the present, for direct fracture energy testing of wood [52]. A joint testing project, initiated by Larsen and Gustafsson, has been performed in conjunction with the intended introduction of the TPB in the CIB timber design code. The fracture energy is the energy dissipated in the fracture process zone (work of fracture) during a unit elongation of a crack. Depending on the load configuration in the testing setup, Figure (4.2), the energy put into the fracture process may be obtained

$$G_{cI} = \frac{1}{(h-a_0)b}\left(\int_0^{\delta_c} P\, d\delta + (m_0 + 2m_P)\, g\, \delta_c\right) \tag{4.1}$$

where a_0 is the notch depth; δ_c is the deflection at failure; m_0 is the weight of the specimen and m_P is the weight of the testing equipment applied on the specimen. The results of these tests reveal a linear relation between the density, $\varrho_{\omega,\omega}$, and the measured fracture energy, G_{Ic}, Figure (4.16). Similar results are reported by

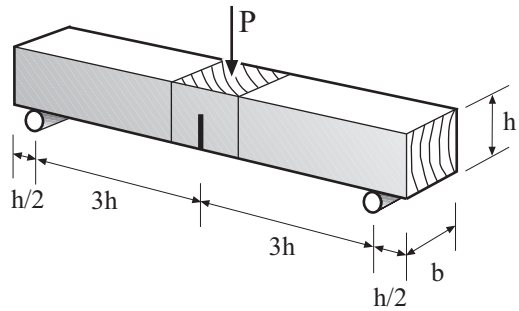

Figure 4.2: Geometry of testing setup in three point bending

Kretschmann [64] and Boström [62]. The specimen with the dimensions $l \times b \times h = 48 \times 45 \times 80$ mm is glued in between two blocks of wood and it is provided with an initial notch of $a_0 = 0.6\ h$. The length of the notch is determined in order to avoid instability in the test. This has been verified with FE calculations by Petersson in [10] and by the author in a verification example of the applied algorithm in the present study, see subsection (7.2.1).

4.3 Shear tests, mode II

4.3.1 Small specimen shear test

Wernersson [32] used a rigid steel frame or grips in which the wood specimen is attached, Figure (4.3). This test was introduced for adhesive joints by Wernersson and Gustafsson in 1987 but has also been used successfully for pure wood specimen. A compressive anti-symmetric load is applied at the ends of the frame for obtaining shear in the specimen. Piston movements in the testing machine are registered as well as the relative slip of the two frame halves. The specimen is provided with notches in order to achieve approximately uniform stress distribution and to stabilize the test. In this test not only the fracture energy but the complete shear stress-deformation curve for the gradual damage of the shear fracture process region is recorded.

4.3.2 Tapered end-notched flexural test

Racois and Valentin and suggested a test for determination of fracture energy in clear wood with respect to shear parallel with grain. The method has been developed within RILEM TC 133 [61]. It consists of a beam with a varying cross-section, $l \times b \times h$, where $l = 500$ mm; $b = 16 - 26$ mm and $h \leq 58$ mm. The beam specimen is provided with a notch where two pieces of teflon are placed in order to prevent undesirable compression at the crack tip. The load deflection response is registered and the work of load, W, evaluated. The size of the fractured region is determined from a visual inspection of the specimen, whereby the fracture energy in modus II

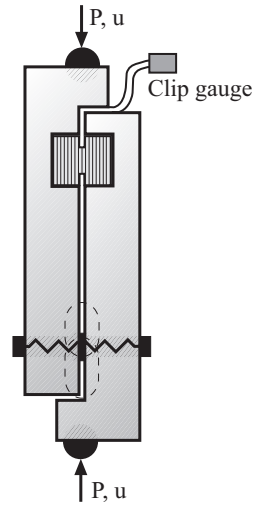

Figure 4.3: Small specimen shear test setup

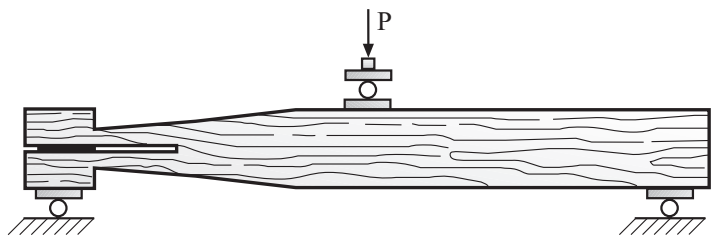

Figure 4.4: Tapered end-notched flexural test

may be calculated as

$$G_{f,II} = \frac{W}{\Delta A} \tag{4.2}$$

The propagation of the crack in the specimen results in a crack area increment equal to $\Delta A = \{(b_1 + b_2)/2 \times (\Delta a_1 + \Delta a_2)/2 + b_1/2 \times b_1/2\}$ where b_1 and b_2 represent the thickness of the specimen at the crack tip, before and after testing. The variables Δa_1 and Δa_2 are the lengths of the crack propagation path on each side of the specimen.

4.4 Mixed mode testing

The strive for a complete mixed mode testing of clear wood has led to the development of a sophisticated equipment for material testing at the Division of Structural Mechanics in Lund. This testing machine (EMS) is equipped with an electromagnetic actuator and it is capable of loading a specimen bi-axially, Figure (4.5). The very high stiffness of the machine in relation to the average specimen size makes it possible to perform direct measurements of fracture energy. Thus, it is not necessary

to make any adjustments of the experimental results regarding influence of the testing equipment as the machine may be considered as completely rigid. The horizontal stiffness of the EMS is in the vicinity of $K_{EMS,H} \approx 50000kN/m$. A specimen of clear wood may be expected to have a corresponding stiffness of $K_{spec,H} \approx 0.015kN/m$ so the difference is of the order 10^6. The control response time is approximately 10 ms for short strokes.

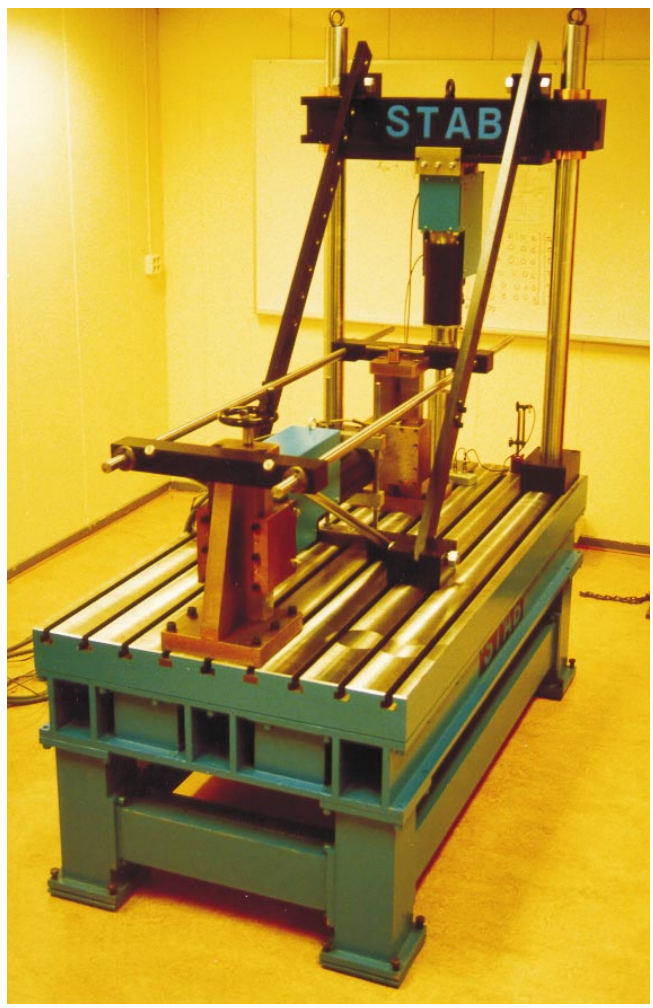

Figure 4.5: EMS testing machine

4.5 Experimental results

4.5.1 General

The experiments reported in this section were all performed with the EMS machine. The specimens of Norwegian spruce (picea abies) were taken from a log referred

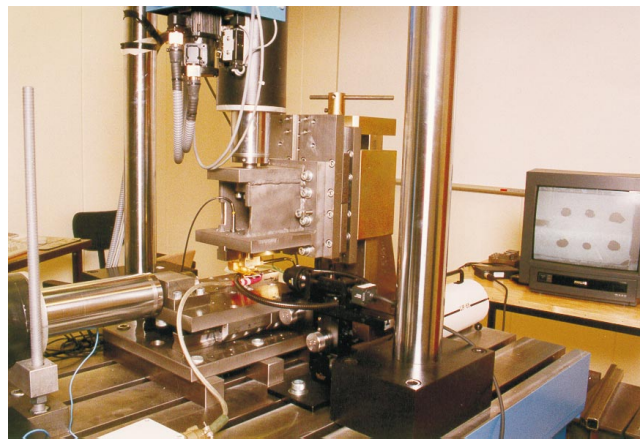

Figure 4.6: Mounted specimen in the biaxial machine

to as 3047001 or $H1$ which was cut at a height between 500mm and 960mm from ground surface. This log has also been used in the experimental part of several other reports, for instance by Persson [44]. Between cutting and production of specimens the log was kept at 5°C and 80% RH. The specimens were cut from the south-east quadrant of the log and preserved at 20°C and 60% RH until testing. The average moisture content at testing was 13.8%. The testing climate was $20-25$°C and about 30% RH.

4.5.2 Experimental setup

The relative shear and tensile movements of the testing machine were registered with LVDT sensors, one for each direction. Further details of the setup are shown in Figure (4.7) and Figure (4.8). The material coordinate directions of the specimens are indicated with L, R and T in the figure. The forces and displacements are F_s, δ_s in the shear direction and F_n, δ_n in the tensile direction. The dimensions of the

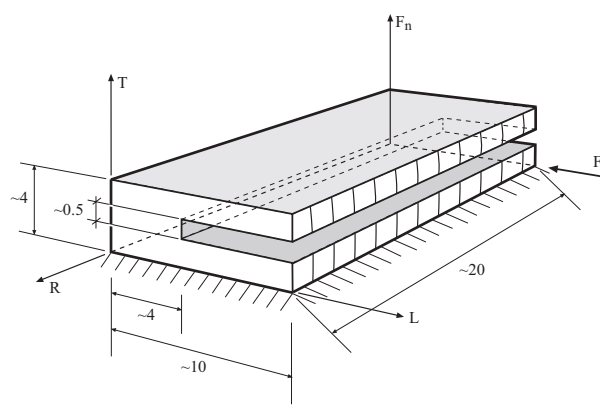

Figure 4.7: Specimen geometry [mm] and definition of coordinates

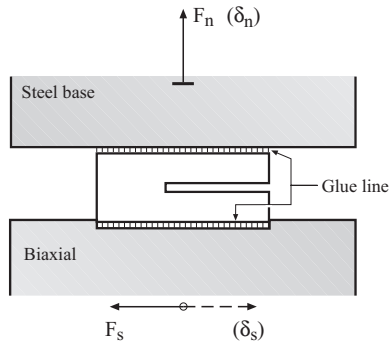

Figure 4.8: Specimen setup

specimen were approximately according to Figure (4.7). The following notations were used in the experiments:

$\delta_n =$	vertical tensile displacement
$\delta_s =$	horizontal shear displacement
$\sigma =$	mean tensile stress
$\tau =$	mean shear stress
k =	δ_n/δ_s or σ/τ

Table 4.1: Experiment notations

The loading rate was kept constant, $\sqrt{\delta_n^2 + \delta_s^2} = 0.0017mm/s$, throughout the experiments.

4.5.3 Results obtained

The experimental results presented here are subtracted from the basic results of displacement controlled testing, given in Appendix B. The combined stress-displacement curves are given in Figures (4.9) to (4.13).

Each figure represents a specific displacement ratio. The shear stresses are indicated with dashed lines and the tensile stresses with solid lines. In Figure (4.9) the curves coincide fairy well, indicating a rather stable testing procedure. This is also reflected in the remaining figures regarding the shear mode. On the other hand, the tensile mode shows more deviations from what might be expected. This is especially apparent in Figure (4.10) and Figure (4.11) i.e. for the lower values of the displacement ratio. For the displacement ratios of $k = 2.0$ and $k = \infty$ this effect seems to be absent or at least minimal. The pure tensile tests also indicate a fairly stable testing procedure.

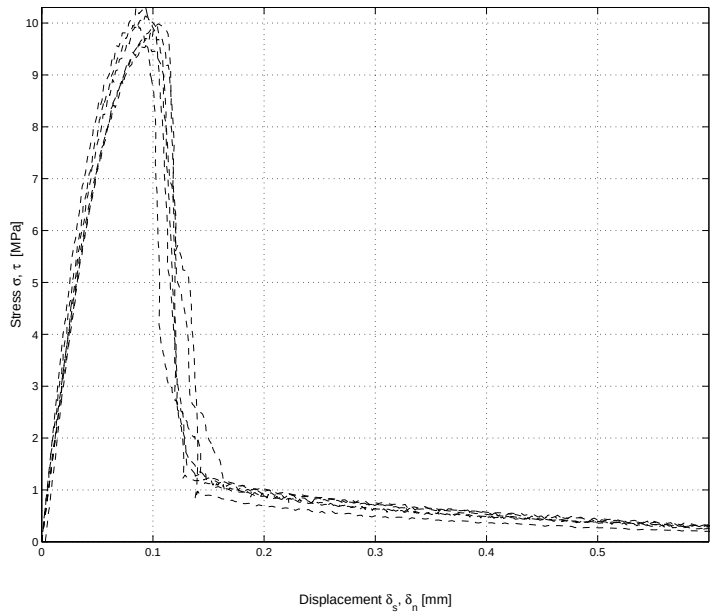

Figure 4.9: Stress-displacement, combined results for $k = 0.0$

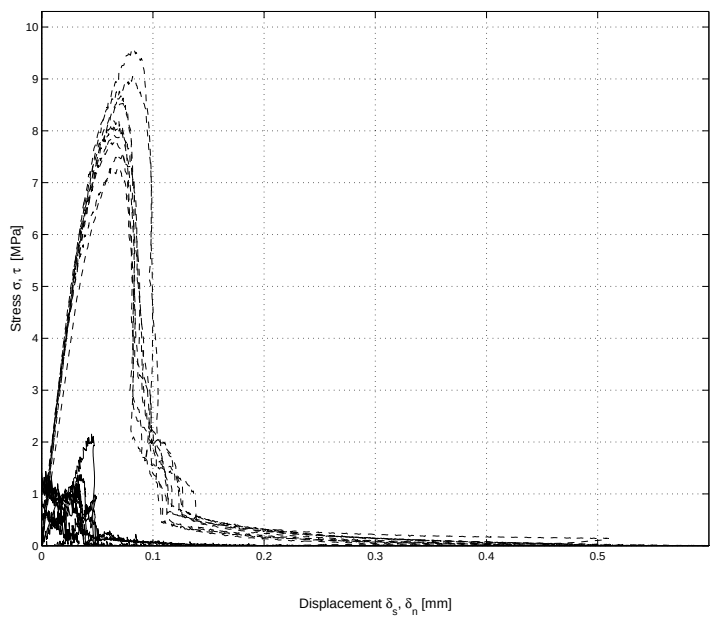

Figure 4.10: Stress-displacement, combined results for $k = 0.5$

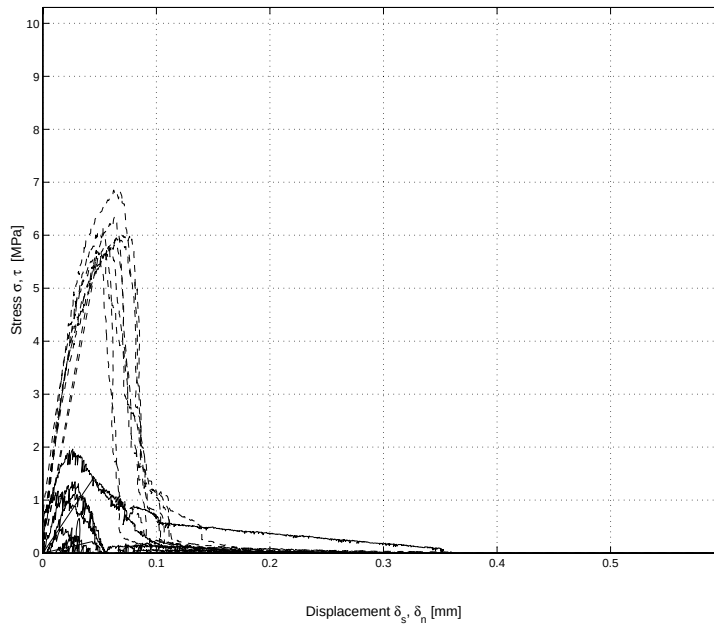

Figure 4.11: Stress-displacement, combined results for $k = 1.0$

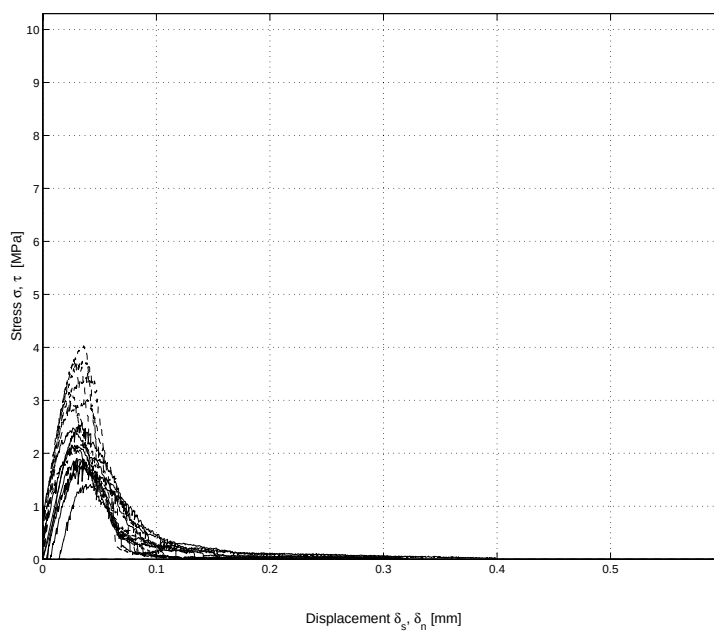

Figure 4.12: Stress-displacement, combined results for $k = 2.0$

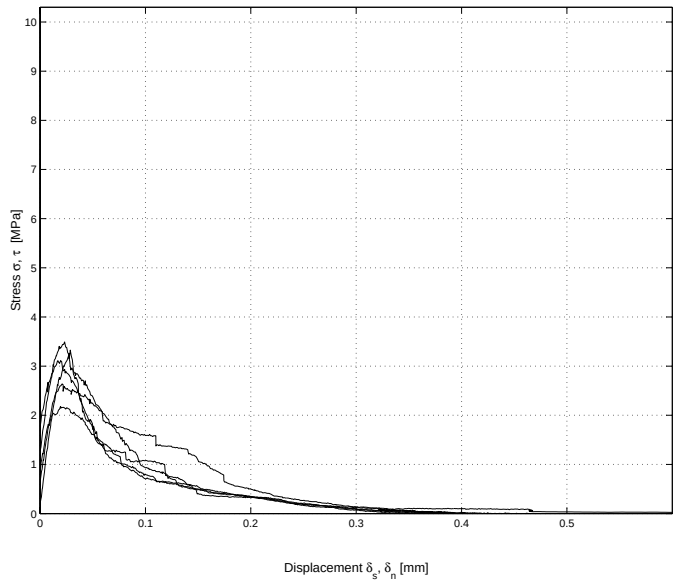

Figure 4.13: Stress-displacement, combined results for $k = \infty$

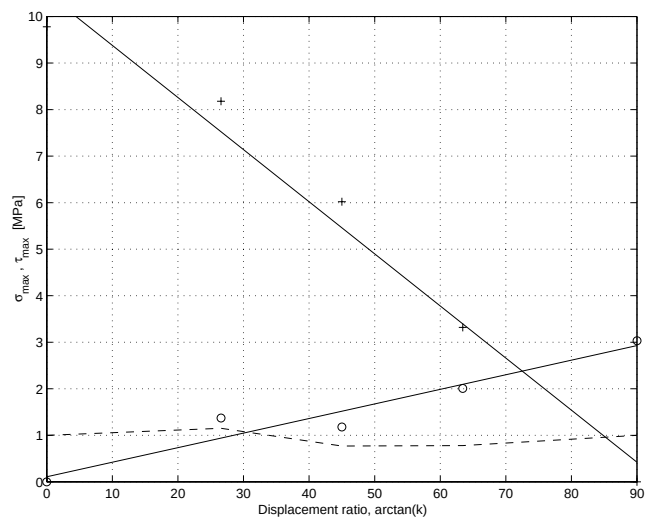

Figure 4.14: Strength versus displacement ratio.

Figure (4.14) shows the average tensile and shear strength in relation to the displacement ratio. The data has been fitted with linear regression curves. Applying Norris criterion to the measured results we get the dashed line in Figure (4.14) which is fairly close to the expected value 1.0 and thus supports the use of the criterion in

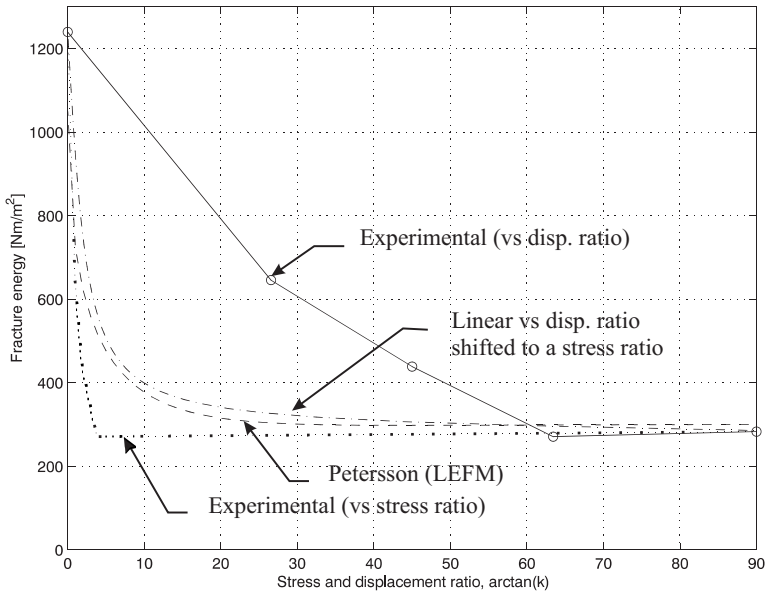

Figure 4.15: Fracture energy versus displacement/stress ratio.

the fracture analysis. The criterion of Norris used here is:

$$\left(\frac{\sigma}{f_t}\right)^2 + \left(\frac{\tau}{f_v}\right)^2 = 1.0 \tag{4.3}$$

In Figure (4.15) the fracture energy versus displacement ratio is indicated as experimental results versus displacement ratio. Assuming that $\frac{E_\parallel}{E_\perp} \approx 30$ we can plot the measured results versus stress ratio which deviates primarily form the criterion assumed by Petersson for stress ratios less than $k = 0.5$. If we instead assume that the fracture energy is related to the displacement ratio, arctan(k), in a linear manner and we get very close to the criterion adopted by Petersson, Figure(5.5) by transforming the displacement ratio to a stress ratio.

4.5.4 Remarks on density

The radial variation of stiffness in the tree trunk has been reported by Persson [44, 45]. This brings to mind the question of how the fracture energy may vary. A potential relation for mode I fracture energy versus density has been extracted from [52], Figure (4.16). This relation is approached with two straight lines, one representing European softwood and the other representing all specimens in the project. This leaves the question of whether it may be possible to estimate fracture energy values in an indirect manner by measuring the density and the elastic modulus.

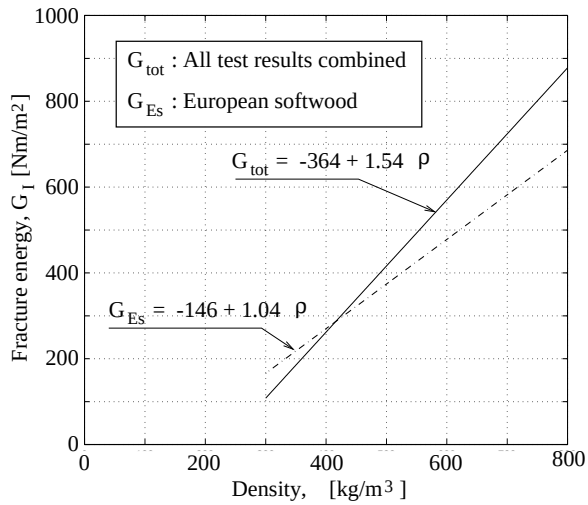

Figure 4.16: Mode I fracture energy versus density [52]

Chapter 5

Linear Elastic Fracture Mechanics Model

5.1 General

Various methods of numerical fracture analysis of structures have been developed by utilizing linear elastic fracture mechanics. One of the most promising methods adopted for finite element analysis is often referred to as the energy release rate method. The method is also known as the compliance method, due to the theoretical approach, or the virtual crack extension method, which reflects the methodology of the calculation process. This method has been adopted here for examining the relationship between crack propagation and the corresponding critical load. An outline of the theory is given in [8] and it has been applied by the author and Gullander [3].

5.2 Basic theory

The following basic theory is adopted from Petersson [8]. A more detailed description is given in Appendix C.

We assume a linear elastic body subjected to small strains, except for the cracking process zone. The equilibrium equations may be written as

$$\frac{\partial \sigma_{ij}}{\partial x_j} + b_i = 0 \tag{5.1}$$

where $\sigma_{ij} = \sigma_{ji}$ is a stress component, b_i a body force component and x_j refers to a Cartesian coordinate system. The tractions, p_i, on the boundary surface S are defined by

$$p_i = n_j \sigma_{ij} \tag{5.2}$$

where n_j is a direction cosine for the outward normal to the surface S.

For a body with a crack, Figure (5.1), a week formulation of the equilibrium equations may be established, starting from equilibrium equations, Eq.(5.1).

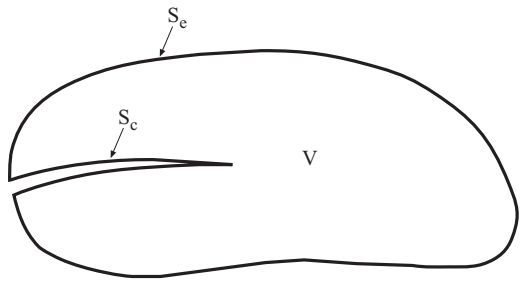

Figure 5.1: Studied body with a crack. Total boundary surface $S = S_e + S_c$

By introducing weighting functions v_i (i = 1,2,3) [23]

$$\int_V v_i \frac{\partial \sigma_{ij}}{\partial x_j} dV + \int_V v_i b_i dV = 0 \tag{5.3}$$

Through substitution of variables and integration by parts we reach at

$$\int_V b_i \frac{du_i}{da} dV + \int_{S_c} p_i \frac{du_i}{da} dS = b_c \int (w_i \frac{dp_i}{da} - \frac{dw_i}{da} p_i) da \tag{5.4}$$

In order to simplify we assume that the relations between p_i and w_i (i=1,2,3) are unique, see Figure (5.2), so we may write $p_i = p_i(w_i)$ or $w_i = w_i(p_i)$, yielding

$$\int_{a_c} (w_i \frac{dp_i}{da} - \frac{dw_i}{da} p_i) da = \int_0^{p_{i0}} w_i dp_i - \int_{w_{i0}}^0 p_i dw_i = 2G_c \tag{5.5}$$

where

$$G_c = \sum_{i=1}^{3} G_{ci} = \int_0^{p_i 0} w_i dp_i = \int_0^{w_{i0}} p_i dw_i \tag{5.6}$$

and da is an infinitesimal crack length and b_c is the width of the crack surface. Substitution of Eq.(5.5) into Eq.(5.4) results in

$$\int_V b_i \frac{du_i}{da} dV + \int_{S_e} p_i \frac{du_i}{da} dS = 2 b_c G_c \tag{5.7}$$

Assuming concentrated forces $\{P\}$ only, we may introduce

$${P_c}^T = [P_{c1} P_{c2} \cdots P_{cn}] \tag{5.8}$$

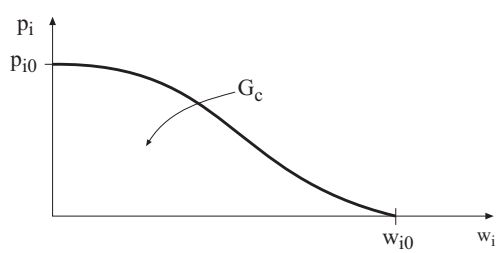

Figure 5.2: Relation between cohesive stress p_i and relative displacement w_i

for the cracking load level where the associated displacements are $\{u_c\}$,

$$u_c{}^T = [u_{c1} u_{c2} \cdots u_{cn}] \tag{5.9}$$

This enables Eq.(5.7) to be written on the form

$$P_c{}^T \frac{du_c}{da} = 2b_c G_c \tag{5.10}$$

This basic matrix equation, Eq.(5.10), can conveniently be used in finite element analysis where $\{P_c\}$ and $\{u_c\}$ will then refer to nodal loads and nodal displacements, respectively.

5.3 Applied theory

The two-dimensional structure introduced in Figure (5.3) is subjected to reference loads {P}. The material is assumed linear elastic and by denoting the displacements with {u} we have

$$\{P\} = \begin{bmatrix} P_1 \\ P_2 \\ \vdots \\ P_n \end{bmatrix} \qquad \{u\} = \begin{bmatrix} u_1 \\ u_2 \\ \vdots \\ u_n \end{bmatrix} \tag{5.11}$$

The crack length is denoted with a and the fracture energy with G_c. The fracture energy G_c is considered to be a material parameter, according to Griffith's theory. By assuming that the external loads are increased proportionally, step by step, the actual loads may be written as $\alpha\{\mathrm{P}\}$ where α is increased gradually up to the critical level of $\alpha = \alpha_c$ which corresponds to the maximum (critical) load level for the actual state (crack length). The corresponding displacements are $\alpha_c\{u\}$. We can express the displacements by the flexibility relation

$$\{u\} = [C]\{P\} \tag{5.12}$$

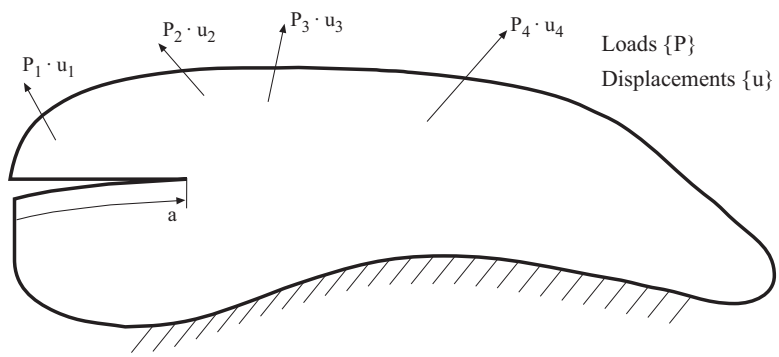

Figure 5.3: Two-dimensional body with a crack

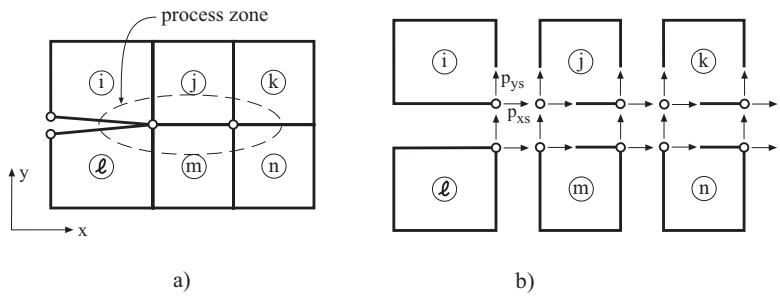

Figure 5.4: Nodal element forces close to cracking process zone

where the flexibility matrix $[C]$ is also termed as the compliance. The linear elastic material stores an internal energy which can be expressed as

$$W = \frac{1}{2}\alpha^2\{P\}^T\{u\} = \frac{1}{2}\alpha^2\{P\}^T[C]\{P\} \tag{5.13}$$

We now have, (see Appendix C)

$$\frac{\partial W}{\partial a} = 2b_c G_c \tag{5.14}$$

which leads to

$$\alpha_c = \sqrt{\frac{2b_c G_c}{\{P\}^T \frac{dC}{da}\{P\}}} \tag{5.15}$$

Equation (5.15) is straightforward to use in finite element analysis. If a crack is allowed to progress gradually we obtain the displacements u_i for each value of the crack length $a = a_i$. Each incremental step in crack length may be approximated with

$$\Delta a_i = a_{i+1} - a_i \tag{5.16}$$

The critical load factor α_c may now be written in an incremental form

$$\alpha_{ci} = \sqrt{\frac{2b_c \Delta a_i G_c}{\{P\}^T(\{u\}_{i+1} - \{u\}_i)}} \tag{5.17}$$

where the crack length is defined as

$$a \approx \frac{a_{i+1} + a_i}{2} \tag{5.18}$$

A convenient method for computing mixed mode fracture includes that the fracture energy is estimated through a relation between the stress ratio $\frac{\bar{\sigma}_\perp}{\bar{\tau}}$ and the fracture energy G_c. A reasonable estimate of this stress ratio can be obtained in finite element analysis by evaluating the nodal forces from the elements which are close to the crack tip, Figure (5.4). The stress ratio in the assumed process zone is obtained by

$$\frac{\bar{\sigma}_\perp}{\bar{\tau}} \approx \frac{\sum_s P_{ys}}{\sum_s P_{xs}} \tag{5.19}$$

The relation between the stress ratio and the fracture energy shown in Figure (5.5) has been suggested by Gustafsson [4]. This relation is based on Eq.(3.32). The material parameters used to establish the relationship and for all LEFM studies in consequent chapters are as follows:

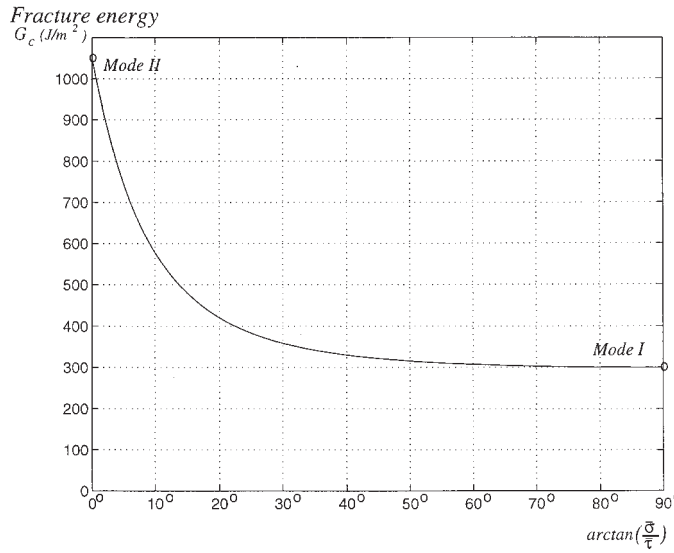

Figure 5.5: Fracture criterion applied for mixed mode

Elasticity moduli	$E_{\parallel}$	12000	MPa
	$E_{\perp}$	400	MPa
Shear modulus	$G_{\parallel,\perp}$	750	MPa
Poisson's ratio	$\nu_{\parallel,\perp}$	0.41	-
Fracture energy	$G_{I,c}$	300	Nm/m^2
	$G_{II,c}$	1050	Nm/m^2

Table 5.1: Material parameters in mixed mode fracture criterion

5.4 Analyzed beam geometries

The finite element calculations have been carried out on six different geometries, Figure (5.6), referred to as geometry a, b, c, d, e and f. Geometries a, b, e and f were analyzed by the author for a beam height of $h = 600mm$ and a width of $b = 120mm$. Calculations on the all these geometries, for both $h = 600mm$ and $h = 95mm$, have also been carried out by Gullander [3].

Due to symmetry, only the left half of the beams is modelled. The support load is chosen as the reference load in the analysis. A basic requirement for application of the conventional non-modified LEFM is the existence of a sharp crack. Therefore, a crack was assumed in the critical region of the beam analyzed, and the critical load was calculated for various lengths of this crack.

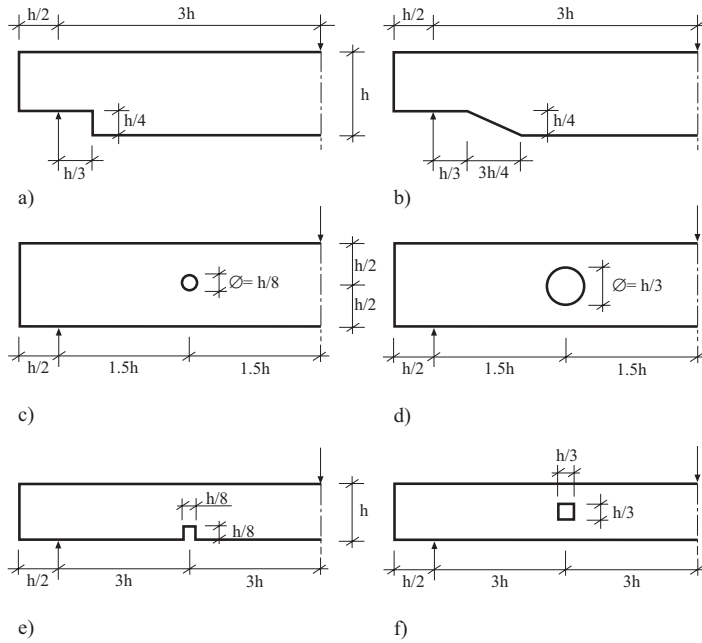

Figure 5.6: Studied beam geometries

5.5 Finite element models

The simulation of crack growth is accomplished by allowing incremental crack growth under constant loading. This is done by using interface elements in the assumed crack zone and allowing them to debond, node by node [8, 18]. Convergence studies, carried out on the end-notched geometry a), revealed that reasonable mesh size for the larger geometries ($h = 600mm$) is approximately 6mm and for the smaller geometries ($h = 95mm$) near 1-2mm. The crack is assumed to propagate parallel to grain which in the model is along the direction of the beam. For the geometries with angular notches or holes the crack is assumed to propagate from the point where the highest stress concentration is experienced which is often in the vicinity of a geometric discontinuity.

The numerical results are presented in Chapter 7.

Chapter 6

Non-Linear Fracture Mechanics Model

6.1 General

The stress-deformation performance of materials is in general non-linear during fracture, both in the fracture process region and in the vicinity of that region. In the process region there is increasing damage and for materials inhibiting some ductile behavior plastic zones will form in the vicinity of the fracture zone. Several numerical methods are available to manage non-linear analysis. They differ in the numerical approach and the definition of fracture elements with the corresponding differences in implementation. The model can be based on continuum elements or interface elements (discrete crack, orthotropic plasticity, Coulomb friction) [29]. A choice has to be made wether the fracture zone is to be modelled with, for instance; discrete springs, distributed springs, hybrid elements with an internal crack or plasticity elements with damage. In the present study a model based on the fictious crack model concept is applied on a prescribed crack path. Interface elements are used and the non-linear numerical algorithm is a perturbation algorithm.

6.2 Fictious crack model

The fictious crack model has its origin in the work of Hillerborg et.al. [30] where the prescribed crack path is applied with appropriate material properties expressed by poly-linear functions as illustrated in Figure (6.1). In this figure a non-linear stress-displacement relation is shown.

6.2.1 Constitutive relations

The material properties of the fracture zone are modelled by introducing contact elements with initial zero thickness between the adjacent fracture surfaces. The constitutive relation for an in-plane state is simplest extracted from the 3-dimensional

constitutive expression for an orthotropic linear elastic medium. Starting from

$$\begin{Bmatrix} \delta_{xx} \\ \delta_{yy} \\ \delta_{zz} \\ \delta_{xy} \\ \delta_{xz} \\ \delta_{yz} \end{Bmatrix} = \begin{bmatrix} C_{11} & C_{12} & C_{13} & 0 & 0 & 0 \\ C_{21} & C_{22} & C_{23} & 0 & 0 & 0 \\ C_{31} & C_{32} & C_{33} & 0 & 0 & 0 \\ 0 & 0 & 0 & C_{44} & 0 & 0 \\ 0 & 0 & 0 & 0 & C_{55} & 0 \\ 0 & 0 & 0 & 0 & 0 & C_{66} \end{bmatrix} \begin{Bmatrix} \sigma_{xx} \\ \sigma_{yy} \\ \sigma_{zz} \\ \tau_{xy} \\ \tau_{xz} \\ \tau_{yz} \end{Bmatrix} \tag{6.1}$$

where the engineering strains ϵ_{ij} have been replaced by relative displacements δ_{ij}. This is due to difficulties in interpreting the strains related to zero thickness of the fracture plane, assumed to be oriented with its normal in the y-direction. The following formulation is according to the spring model of Figure (6.2). The flexibility parameters C_{ij} are functions of the current state of deformation, $C_{ij} = C_{ij}(\delta)$. For the state of plane stress where $\sigma_{zz} = \tau_{xz} = \tau_{yz} = 0$ the constitutive relation reduces to

$$\begin{Bmatrix} \delta_{xx} \\ \delta_{yy} \\ \delta_{xy} \end{Bmatrix} = \begin{bmatrix} C_{11} & C_{12} & 0 \\ C_{21} & C_{22} & 0 \\ 0 & 0 & C_{44} \end{bmatrix} \begin{Bmatrix} \sigma_{xx} \\ \sigma_{yy} \\ \tau_{xy} \end{Bmatrix} \tag{6.2}$$

In the present two-spring model δ_{xx} is assumed not to be affected by σ_{yy} and $\delta_{yy}$is assumed not to be affected by σ_{xx}. Accordingly

$$C_{11} = C_{12} = 0 \tag{6.3}$$

The constitutive relation may now be reduced further and the inverse relation to Eq.(6.2) with the stiffness matrix D simply becomes

$$\begin{Bmatrix} \sigma_{xx} \\ \sigma_{yy} \\ \sigma_{xy} \end{Bmatrix} = \begin{bmatrix} \frac{1}{C_{11}} & 0 & 0 \\ 0 & \frac{1}{C_{22}} & 0 \\ 0 & 0 & \frac{1}{C_{44}} \end{bmatrix} \begin{Bmatrix} \delta_{xx} \\ \delta_{yy} \\ \delta_{xy} \end{Bmatrix} = \begin{bmatrix} D_{11} & 0 & 0 \\ 0 & D_{22} & 0 \\ 0 & 0 & D_{44} \end{bmatrix} \begin{Bmatrix} \delta_{xx} \\ \delta_{yy} \\ \delta_{xy} \end{Bmatrix} \tag{6.4}$$

where, in mixed mode analysis, $D_{11} = D_{11}(\delta_n, \delta_s)$, $D_{22} = D_{22}(\delta_n, \delta_s)$ and $D_{44} = D_{44}(\delta_n, \delta_s)$. The first row in the constitutive expression above can be left out of the modelling of the stresses acting across the fracture zone, resulting in a simple constitutive expression for the non-linear two-spring model.

$$\begin{Bmatrix} \sigma_{yy} \\ \sigma_{xy} \end{Bmatrix} = \begin{bmatrix} D_{22} & 0 \\ 0 & D_{44} \end{bmatrix} \begin{Bmatrix} \delta_{yy} \\ \delta_{xy} \end{Bmatrix} \tag{6.5}$$

Making use of the inverse of the compliance matrix in Eq.(6.1) and assuming that $\delta_{33} = \delta_{13} = \delta_{23} = 0$ the stiffness matrix in a plane strain state appears as

$$\begin{Bmatrix} \sigma_{xx} \\ \sigma_{yy} \\ \sigma_{xy} \end{Bmatrix} = \begin{bmatrix} \frac{C_{33}C_{22} - C_{23}^2}{\mathcal{C}} & \frac{C_{13}C_{32}}{\mathcal{C}} & 0 \\ \frac{C_{13}C_{23}}{\mathcal{C}} & \frac{C_{11}C_{33} - C_{13}^2}{\mathcal{C}} & 0 \\ 0 & 0 & \frac{1}{C_{44}} \end{bmatrix} \begin{Bmatrix} \delta_{xx} \\ \delta_{yy} \\ \delta_{xy} \end{Bmatrix} \tag{6.6}$$

where $\mathcal{C} = C_{11}C_{22}C_{33} - C_{11}C_{23}^2 - C_{22}C_{13}^2$. The third row of Eq.(6.6) reveals that $C_{32} = C_{23} = 0$ which in turn makes the stiffness matrix reducible to

$$\begin{bmatrix} \frac{C_{11}C_{33}-C_{13}^2}{C_{22}(C_{11}C_{33}-C_{13}^2)} & 0 \\ 0 & \frac{1}{C_{44}} \end{bmatrix} = \begin{bmatrix} \frac{1}{C_{22}} & 0 \\ 0 & \frac{1}{C_{44}} \end{bmatrix} = \begin{bmatrix} D_{22} & 0 \\ 0 & D_{44} \end{bmatrix} \tag{6.7}$$

which is exactly the same stiffness matrix as in the case of plane stress. In this case the components, D_{ij}, of the stiffness matrix are derivatives of stress relative to displacements, $\frac{\partial \sigma_{ij}}{\partial \delta_{kl}}$, and not strains as in the normal case of continuum mechanics.

For use in numerical applications the $\sigma - \delta$ curves may be simplified in a manner that assumes linear-elastic material up to the limit of ultimate tensile strength, f_t. The intrinsic $\sigma - \delta$ curve from tests is characterized by the ultimate tensile strength, f_t, at $\delta = 0$; the stress $\sigma(\delta) = 0$ at $\delta = \delta_c$; and the assumed material parameter G_F, the fracture energy which is represented by the area under the $\sigma(\delta)$ curve.

$$G_F = \int_{f_t}^{0} \delta(\sigma) d\sigma = \int_{0}^{\delta_c} \sigma(\delta) d\delta \tag{6.8}$$

where δ_c is the deformation for which $\sigma(\delta) = 0$. In the case of mixed-mode in-plane fracture the total fracture energy can be determined by

$$G_F = \int_{\Gamma} (\sigma(\delta_n) d\delta_n + \tau(\delta_s) d\delta_s) \tag{6.9}$$

The $\sigma(\delta)$ curve may be approximated by some curve, for instance a polynom, or by a multi-linear curve. Common approximations are simple linear and bi-linear curves. For more accurate approximations further subdivision of the $\sigma(\delta)$ curve into piecewise linear relations can be made. For instance, the tangential material stiffness is zero at $\sigma(\delta) = f_t$ which can be expressed in form the derivative of the $\sigma(\delta)$ curve at the point of interest. For a single linear curve $\frac{\partial \sigma}{\partial \delta} < 0$. The degree of multi-linearity must be balanced between accuracy in material modelling and increase in computation time. The poly-linear functions describing the constitutive behavior of the fracture zone can be expressed as analytical functions by utilizing Heaviside's step function, $\theta()$. This choice will prove to be useful when implementing the theory in a program code. Given a piecewise linear curve with all breakpoints known, Figure(6.1) we can express the functions f_0, f_1 and f_2 as

$$\left.\begin{aligned} f_0 &= (\theta(\delta - \delta_0) - \theta(\delta - \delta_1)) \left\{ \frac{\sigma_1 - \sigma_0}{\delta_1 - \delta_0}(\delta - \delta_0) + \sigma_0 \right\} \\ f_1 &= (\theta(\delta - \delta_1) - \theta(\delta - \delta_2)) \left\{ \frac{\sigma_2 - \sigma_1}{\delta_2 - \delta_1}(\delta - \delta_1) + \sigma_1 \right\} \\ f_2 &= (\theta(\delta - \delta_2) - \theta(\delta - \delta_3)) \left\{ \frac{\sigma_3 - \sigma_2}{\delta_3 - \delta_2}(\delta - \delta_2) + \sigma_2 \right\} \end{aligned}\right\} \tag{6.10}$$

Thus, an analytic constitutive expression for any number of poly-linear subsets can be written conveniently as

$$\mathcal{F} = f_0 + f_1 + f_2 + \cdots + f_n \tag{6.11}$$

or

$$\mathcal{F}(\delta) = \sum_{i=0}^{i=n} (\theta(\delta - \delta_i) - \theta(\delta - \delta_{i+1})) \left\{ \frac{\sigma_{i+1} - \sigma_i}{\delta_{i+1} - \delta_i}(\delta - \delta_i) + \sigma_i \right\} \tag{6.12}$$

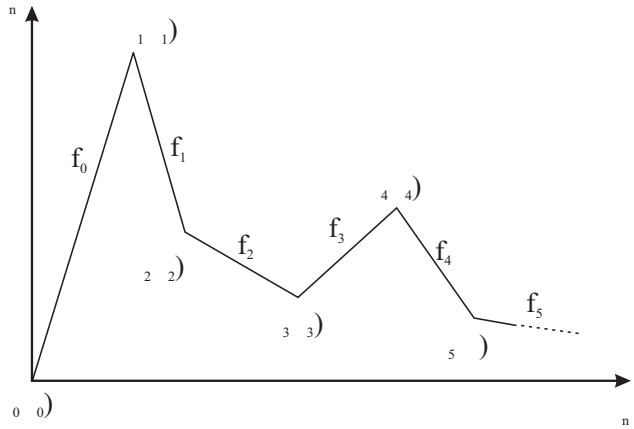

Figure 6.1: Constitutive function

This may not seem to be very smooth and easy analytical form but the advantages appear in the implementation to a program code due to the fact that Heaviside's function can simply be replaced with the sign function, sgn(), implied by all programming languages.

$$\theta(t-a) = \frac{(sgn(t-a)+1)}{2} \tag{6.13}$$

Furthermore the stiffness for any point on the poly-linear curve can now easily be expressed on the same form. The stiffness is simply the slope at any point or the derivative of the constitutive expression. The stiffness thus becomes

$$\begin{aligned} \mathcal{F}'(\delta) &= \sum_{i=0}^{i=n} \left\{ \frac{\sigma_{i+1}-\sigma_i}{\delta_{i+1}-\delta_i}\delta + \sigma_i \right\} (\delta^*(\delta-\delta_i) - \delta^*(\delta-\delta_{i+1})) + \\ & (\theta(\delta-\delta_i) - \theta(\delta-\delta_{i+1}))\frac{\sigma_{i+1}-\sigma_i}{\delta_{i+1}-\delta_i} \end{aligned} \tag{6.14}$$

where δ^* is Dirac's delta function. This function has only values different from zero when the argument is equal to zero, i.e. at the breakpoints. For computing stiffnesses and stress levels these points are not of interest. We can state that our primary interest is the interval between the brake-points. Therefore, it is possible to simplify Eq.(6.14) by eliminating or simply neglecting the terms including the Dirac's delta function and restricting the applicability of the expression to the interval between brakepoints. Thus, the stiffness may be written as

$$\mathcal{F}'(\delta) = \mathcal{K}(\delta) = \sum_{i=0}^{i=n} (\theta(\delta-\delta_i) - \theta(\delta-\delta_{i+1}))\frac{\sigma_{i+1}-\sigma_i}{\delta_{i+1}-\delta_i} \tag{6.15}$$

Equation (6.15) implies that

$$\left.\begin{array}{rcl} f_0' &=& k_0 \\ f_1' &=& k_1 \\ f_2' &=& k_2 \\ \vdots & & \\ f_n' &=& k_n \end{array}\right\} \tag{6.16}$$

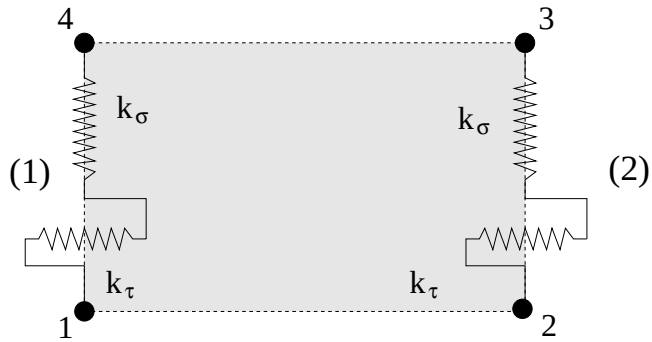

Figure 6.2: Two-spring model

6.2.2 Element formulation

The element formulation is according to a four-node quadrilateral element based on an implementation of the two-spring model, see Figure (6.2). The element consists of two pairs of nodes, each of which coincide up to a load level of ultimate tensile strength, f_t. In the case of non-linear behavior the system of finite element equations may be expressed as

$$K(a)a = f \tag{6.17}$$

where the tangential stiffness matrix $K(a)$ is a function of the displacements, a, and f represents the external forces. Outside the potential crack the material is considered linear-elastic, but the crack elements which inhibit the non-linear behavior have to be formulated in a different manner. Starting with the stiffness matrix

$$K(a) = K(a)_{ij} = \int_S B_i^T D(a) B_j dS \tag{6.18}$$

it may be observed that the B matrix is constant, expressing that no consideration is taken to geometric non-linearity. However, the constitutive matrix, D, is dependent on the displacements as already implied in the discussion of the constitutive relation for the two-spring model. Applying incremental formulation the constitutive relation may be written as

$$\dot{\sigma} = D\dot{\delta} \tag{6.19}$$

and the relative displacement rates are expressed as

$$\dot{\delta} = B\dot{a} \tag{6.20}$$

where the B matrix is defined from the relation between the relative displacements and the nodal displacements in the quadrilateral crack element as follows

$$\begin{bmatrix} \dot{\delta}_n^1 \\ \dot{\delta}_s^1 \\ \dot{\delta}_n^2 \\ \dot{\delta}_s^2 \end{bmatrix} = \begin{bmatrix} 0 & -1 & 0 & 1 & 0 & 0 & 0 & 0 \\ -1 & 0 & 1 & 0 & 0 & 0 & 0 & 0 \\ 0 & 0 & 0 & 0 & 0 & -1 & 0 & 1 \\ 0 & 0 & 0 & 0 & -1 & 0 & 1 & 0 \end{bmatrix} \begin{bmatrix} \dot{u}_1^1 \\ \dot{u}_2^1 \\ \dot{u}_3^1 \\ \dot{u}_4^1 \\ \dot{u}_1^2 \\ \dot{u}_2^2 \\ \dot{u}_3^2 \\ \dot{u}_4^2 \end{bmatrix} \tag{6.21}$$

The constitutive relation for the material results in a stiffness relation for a four node element:

$$\begin{bmatrix} \dot{\sigma}_n^1 \\ \dot{\tau}_s^1 \\ \dot{\sigma}_n^2 \\ \dot{\tau}_s^2 \end{bmatrix} = \begin{bmatrix} D_{nn} & D_{ns} & 0 & 0 \\ D_{sn} & D_{ss} & 0 & 0 \\ 0 & 0 & D_{nn} & D_{ns} \\ 0 & 0 & D_{sn} & D_{ss} \end{bmatrix} \begin{bmatrix} \dot{\delta}_n^1 \\ \dot{\delta}_s^1 \\ \dot{\delta}_n^2 \\ \dot{\delta}_s^2 \end{bmatrix} \tag{6.22}$$

The definition of the tangential stiffness matrix in Eq.(6.18) is based on the determination of the incremental global stiffness, i.e. the global tangential stiffness, which is simply expressed as the slope of the global response

$$\dot{K} = \frac{\partial \dot{\sigma}(a)}{\partial \dot{a}} \tag{6.23}$$

Now, the B matrix, including only constant terms, determines the transformation of displacements, a, and forces, $\dot{\sigma}$, between the local and the global systems

$$\dot{a}' = B\dot{a} \qquad \dot{\sigma} = B^T\dot{\sigma}' \tag{6.24}$$

Expanding Eqn.(3.7) with the chain rule results in

$$\dot{K} = \frac{\partial B^T}{\partial a}\dot{\sigma}' + B^T\frac{\partial \dot{\sigma}'}{\partial \dot{a}'}B \tag{6.25}$$

and as the B matrix is constant, the first term disappears and by identification with Eq.(6.18)

$$\frac{\partial \dot{\sigma}'}{\partial \dot{a}'} = \int_\Gamma \dot{D}'(a)dS \tag{6.26}$$

6.2.3 Load factor

When a crack element is subjected to load the elongation of the springs determines the load level between each node pair. This is schematically illustrated in Figure (6.3) where each spring has been assigned a load interval factor, c, which is a measure of the remaining space of loading towards the nearest breakpoint on the approximative curve for the constitutive relation. In Figure (6.4) we may take $\Delta\sigma_T$ as the total load interval which means that initially the load interval factor, c, is equal to one. When a spring is loaded an initial linear response, $\Delta\sigma_k^1$, is detected in the

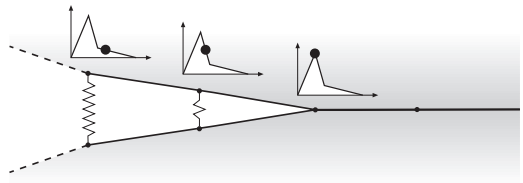

Figure 6.3: Load factor

spring and a new load interval factor may be calculated

$$c_k^1 = 1 - \frac{\Delta\sigma_k^1}{\Delta\sigma_T} = \frac{\Delta\sigma_T - \Delta\sigma_k^1}{\Delta\sigma_T} = \frac{\Delta s_k^1}{\Delta\sigma_T} \qquad (k = node \;\; nr.) \tag{6.27}$$

which gives the loading level, Δs_k^1, as

$$\Delta s_k^1 = c_k^1 \, \Delta\sigma_T \tag{6.28}$$

Continuing in the same manner we get

$$\begin{aligned}
c_k^2 &= 1 - \frac{\Delta\sigma_k^2}{\Delta\sigma_T} = \frac{\Delta\sigma_T - \Delta\sigma_k^2}{\Delta\sigma_T} = \frac{\Delta s_k^2}{\Delta\sigma_T} \\
\Delta s_k^2 &= c_k^2 \, \Delta\sigma_T \\
c_k^3 &= 1 - \frac{\Delta\sigma_k^3}{\Delta\sigma_T} = \frac{\Delta\sigma_T - \Delta\sigma_k^3}{\Delta\sigma_T} = \frac{\Delta s_k^3}{\Delta\sigma_T} \\
\Delta s_k^3 &= c_k^3 \, \Delta\sigma_T \\
&\vdots
\end{aligned} \tag{6.29}$$

which finally results in a general expression for the load interval factor

$$\begin{gathered}
c_k^i = 1 - \frac{\Delta\sigma_k^i}{\Delta\sigma_T \prod_{\gamma=0}^{i-1} c_k^\gamma} \\
nr. \, of \, loading \, steps \;\; i = 1, \cdots, m \quad c_k^0 = 1.0
\end{gathered} \tag{6.30}$$

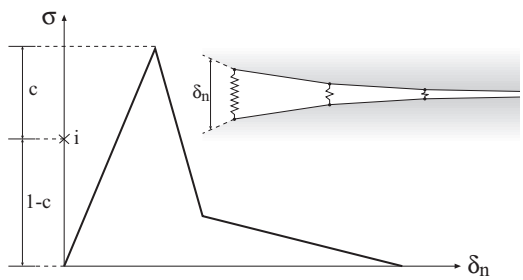

Figure 6.4: Load interval

The load factor, $\mathbf{r}$, is defined as a scaling factor with which the response in the spring $(\Delta\sigma, \Delta\delta)$ is multiplied to reach the nearest breakpoint on the $\sigma(\delta)$ curve. The complementary load interval factor, x, is defined as

$$x_k^i = 1 - c_k^i \tag{6.31}$$

and the load factor, $\mathbf{r}$, may then be derived as

$$r_k^i = \frac{1}{x_k^i} = \frac{1}{1 - c_k^i} = \frac{\Delta\sigma_T \prod_{\gamma=0}^{i-1} c_k^\gamma}{\Delta\sigma_k^i} \tag{6.32}$$

$$nr.\,of\,loading\,steps\ i = 1, \cdots, m \quad c_k^0 = 1.0$$

For convenience we may also write

$$r_k^i = \frac{1}{x_k^i} = \frac{1}{1 - c_k^i} = \frac{\Delta\sigma_T \alpha_k^i}{\Delta\sigma_k^i} \tag{6.33}$$

$$with\ \alpha_k^i = \prod_{\gamma=0}^{i-1} c_k^\gamma; \quad nr.\,of\,loading\,steps\ i = 1, \cdots, m; \quad c_k^0 = 1.0$$

For each computation step the load interval factor, $\mathbf{c}$, has to be updated so as to compensate for the progression of loading. For each and every spring in all loading steps we check for the critical spring or the one which will be the first one to reach a breakpoint anywhere on the $\sigma(\delta)$ curve. Consequently this critical spring will have the smallest load factor, r_{min}, and within each linear computation step we have for each spring a conceivable external load

$$P_k^{i*} = r_k^i \frac{P}{r_{min}} \tag{6.34}$$

Suppose that the external load is always taken to be $P = 1.0$. Then we get the new load interval factors for the present step

$$c_k^i = 1 - \frac{1}{P_k^{i*}} = 1 - \frac{r_{min}}{r_k^i} \tag{6.35}$$

The updated load interval factors that determine the loading space of the next computation step become

$$c_k^{i+1} = c_k^i \prod_{\gamma=0}^{i-1} c_k^\gamma = c_k^i \alpha_k^i \tag{6.36}$$

6.2.4 Path control

For each linear computation step, i, we receive the global response $\bar{E}^i$ corresponding to an unit external load, $P = 1.0$, Figure (6.5). Having determined the corresponding load factor, r_{min}^i, it is still unknown what sign to apply to the the response. It is evident from Figure (6.5) that the directional change of the global response is strongly connected with changes in stiffnesses on the $\sigma(\delta)$ curve. Applying the vector notation in Figure (6.5) the sign of the global response, $r_{min}^i \bar{E}^i$, is derived from the scalar triple product [5]

$$sgn(r_{min}^i) = \frac{\bar{k} \cdot (r_{min}^{i-1} \bar{E}^{i-1} \times \bar{E}^i)}{\bar{k} \cdot (\bar{M}^{i-1} \times \bar{M}^i)} \tag{6.37}$$

$$where\ \bar{k} = (0, 0, 1); \quad \bar{E}^i = (\Delta u^i, 1, 0); \quad \bar{M}^i = (\Delta\delta^i, \Delta\sigma^i, 0)$$

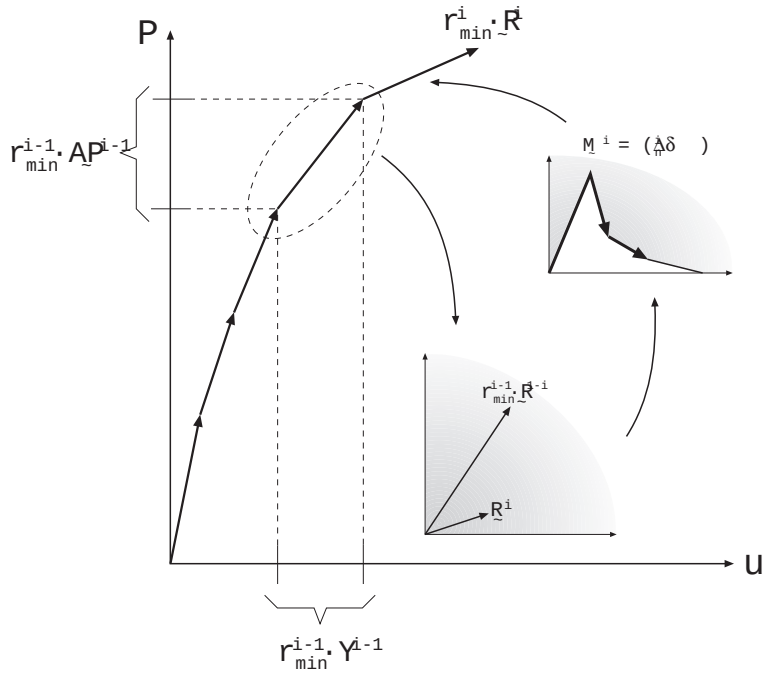

Figure 6.5: Path control

6.2.5 Mode I, Mode II solution algorithm

The solution algorithm is based on an linear incremental solution procedure, Figure (6.1). A structural member is loaded with a unit load, $P = 1.0$, and by use of the load factor, r^i_{min}, and the sign rule for the global response, $sgn(r^i_{min})$, we can determine the intrinsic incremental global response by computing

$$(\Delta P^i, \Delta u^i) = sgn(r^i_{min}) r^i_{min} \bar{E}^i \tag{6.38}$$

The total response is obtained as the accumulative incremental response where the external forces are given by

$$P^i = \sum_{\gamma=0}^{\gamma=i} \Delta P^\gamma \tag{6.39}$$

and the corresponding displacements appear as

$$u^i = \sum_{\gamma=0}^{\gamma=i} \Delta u^\gamma \tag{6.40}$$

The expressions above refer to a single degree of freedom (SDOF) system which can easily be extended to a multi degree of freedom (MDOF) system, i.e. instead of an external point load, multiple point loads can also be applied, approximating different kind of load configurations with distributed load. The program structure used for computing the solution algorithm above is constructed as fortran programs

(Pnforce_list.f and Prload.f) in conjunction with the commercial finite element program ABAQUS as a solver for the global system of equations. ABAQUS utilizes user defined elements, written in fortran (Pcrackel.f), for determining the behavior of the crack zone. For determining the stiffness in each element the element routine has to communicate with the results file through a communication file (Pnodeflag.dat). The different parts of the program structure are controlled or run by a script file written for Unix in the Korn shell programming language. The commercial programming package MATLAB has also been utilized for programming the solution algorithm for PC's.

6.2.6 Mixed mode solution algorithm

Solving the fracture process for Mode I and Mode II simultaneously, termed as mixed mode, is somewhat more complicated than for each mode by itself. It seems obvious that the two modes interact with each other and thus the first task will be to derive a process (method) where this effect is taken into account. In the modelling the two modes are represented by two springs which in the elastic state are considered to have no extension. The first linear part of both the shear and the tension curves is considered to have a slope approaching infinity, Figure(6.1). In the model analysis this slope is of the order 1000 to 100.000 times the following slope, or

$$10^3 \leq \left| \frac{k_0}{k_1} \right| \leq 10^5 \tag{6.41}$$

When the structure is exposed to an external or internal load the level of stress increases simultaneously in both springs provided that both modes are activated. The stress level increases until cracks start to form in the material i.e. maximum stress level (load level) is reached in both modes at the same moment. In other words, both springs are activated and the stiffness of the springs becomes negative. Different criteria have been suggested and used in both continuum models as well as discrete models such as the present one. The following is a criteria suggested by Norris:

$$\left(\frac{\sigma}{f_t}\right)^2 + \left(\frac{\tau}{f_s}\right)^2 \leq 1.0 \tag{6.42}$$

where σ and τ are the stresses in mode I and mode II respectively whereas f_t and f_s are the corresponding strength of pure tension and shear, respectively. Instead of the stress values we may use the stress level for each mode in the criteria. With the stress levels expressed as

$$\begin{aligned} x_{k,\sigma}^{i+1} &= 1 - c_{k,\sigma}^{i+1} = 1 - \left(1 - \frac{r_{min}^{i+1}}{r_{k,\sigma}^{i+1}}\right) c_{k,\sigma}^{i} \\ x_{k,\tau}^{i+1} &= 1 - c_{k,\tau}^{i+1} = 1 - \left(1 - \frac{r_{min}^{i+1}}{r_{k,\tau}^{i+1}}\right) c_{k,\tau}^{i} \end{aligned} \tag{6.43}$$

This may seem to be a sufficient criteria for the activation of the negative springs but as the load factors $r_{min}, r_{k,\sigma}, r_{k,\tau}$ are extracted from the envelope curves for $\sigma - \delta_n$ or $\tau - \delta_s$ we have to introduce a scale factor on $\mathbf{r_{min}}$ which leads to the fracture

criteria used in the present study

$$\left(1-\left(1-\frac{\xi_k r_{min}^{i+1}}{r_{k,\sigma}^{i+1}}\right)c_{k,\sigma}^{i}\right)^2+\left(1-\left(1-\frac{\xi_k r_{min}^{i+1}}{r_{k,\tau}^{i+1}}\right)c_{k,\tau}^{i}\right)^2=1.0 \tag{6.44}$$

For each pair of springs in the model the fracture criteria is simply solved for ξ_k and the solution we seek is the largest positive solution less than 1.0. Having passed the point of fracture we need to define some dimensionless parameters some of which are state variables used to pass information from state (i) to $(i+1)$ These definitions and corresponding derivations are demonstrated here on bilinear curves for both $\sigma-\delta_n$ and $\tau-\delta_s$. However, the expressions derived finally are general expressions for any number of poly-linear subsets.

6.3 Stability of global response

Depending on the ratio of fracture energy and elastic energy stored in a structure, different kind of failure phenomenon can appear. Stable fracture can occur where a structural member "warns" of the potential fracture with extensive deformations and visible damage before the load-bearing capacity is used up. On the other hand, a particularly unstable failure can also be the case with so-called snap-back. The structure can possibly develop a minor visible crack prior to failure but the more unstable the failure, the less visible signs prior to the snap-back. During the numerical computations the risk for instability and/or checking for snap-back can be controlled by performing an eigenvalue analysis on the system equations, Petersson [10], having split them into a system of two stiffness matrices

$$(K^e-K^\sigma)\dot{a}=\dot{P} \tag{6.45}$$

The K^e matrix includes only constant contributions from the linear-elastic part of the structural member outside the potential cracking zone. The K^σ matrix, however, can vary during the cracking process resulting in an unstable failure. By performing the eigenvalue analysis

$$\det([K^e-\lambda K^\sigma])=0 \tag{6.46}$$

the lowest eigenvalue λ_1 can be used as a measure of the risk for instability in the crack propagation.

Chapter 7

Numerical Study

7.1 General

The experimental work described in Chapter 4 and the methods of numerical modelling described in Chapters 5 and 6 form the background for the following numerical studies. The influence of geometry and load configurations are the main issues.

All LEFM studies were carried out utilizing the general purpose finite element program ABAQUS. The NLFM modelling was partly carried out using ABAQUS where the crack propagation process was implemented as FORTRAN subroutines. The major part of the parameter studies (NLFM) was carried out by utilizing the general purpose mathematics program MATLAB and the finite element package CALFEM. The crack propagation procedure was implemented in the same manner as the CALFEM routines.

In Figure (7.1) we have a schematic illustration of the procedures of LEFM and NLFM implemented here. We start with the fracture energy as a basic material parameter. In the case of LEFM we then detect the stress field and provide the critical load through a fracture criterion. The NLFM procedure descends from the constitutive relation for tensile and shear fracture which may be combined in a mixed mode relation. Finally the global response is extracted from crack propagation procedure.

The first of subsequent sections in this chapter are dedicated to convergence study and verification of the modelling. Use is made of the three-point bending test, the four-point bending test and results from the EMS tests (Section 4.4) on small clear wood specimen. Furthermore, comparison is made with known test results for end-notched beams.

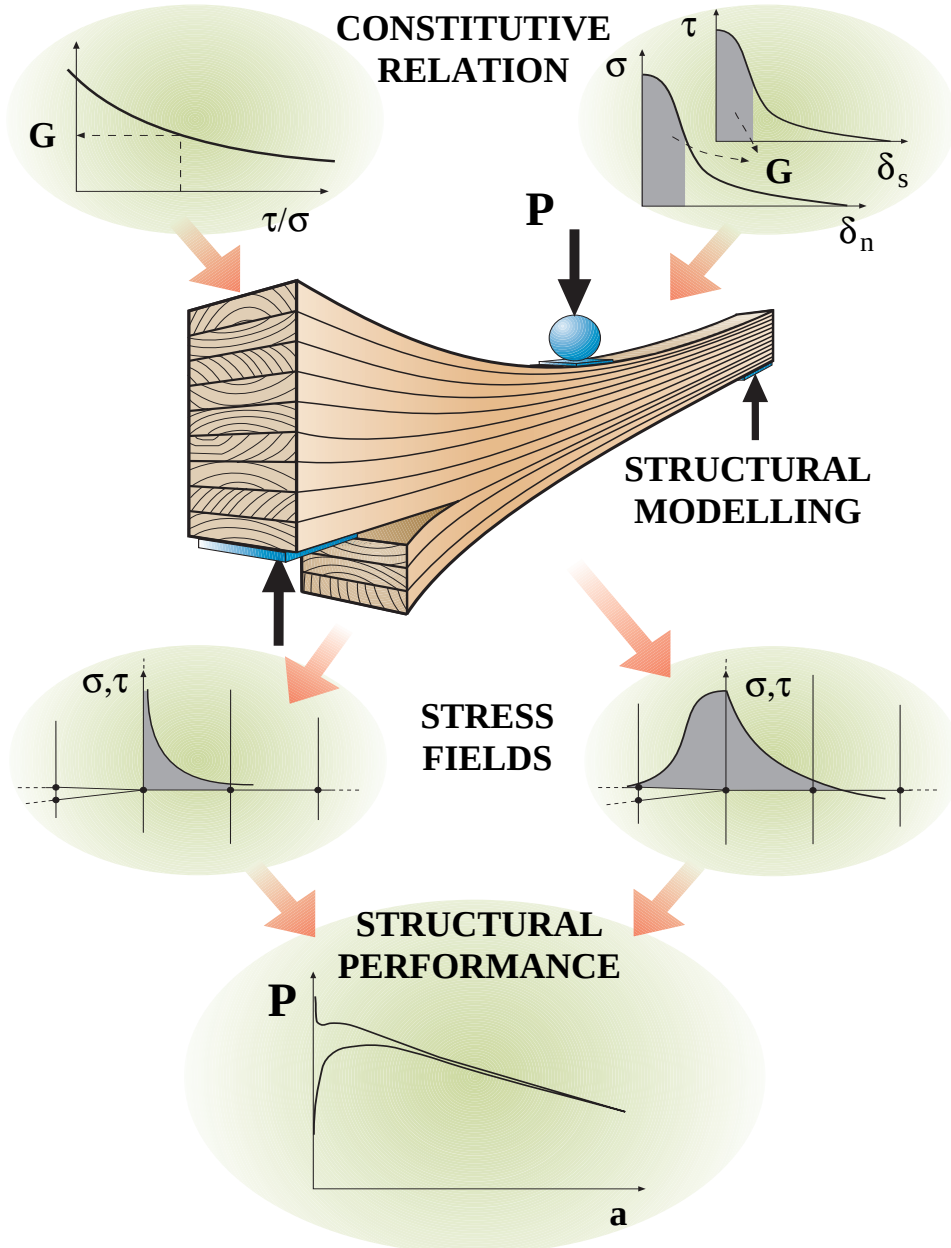

Figure 7.1: Schematic illustration of the two main fields of fracture analysis, LEFM and NLFM

7.2 Verification of FE-modelling

7.2.1 Test specimen for determination of Mode I fracture energy

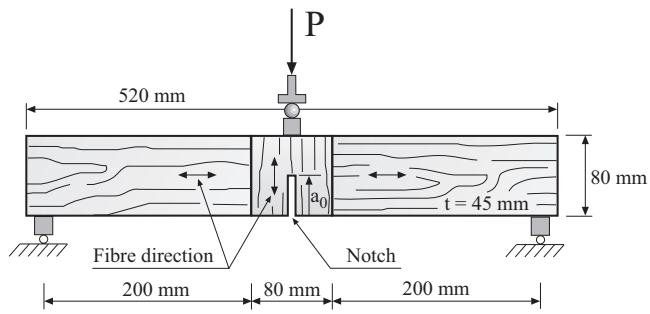

Figure 7.2: Test specimen for mode I fracture

The three point test specimen has been chosen here for verification by NLFM. This test specimen has been adopted as a standard test specimen [62, 51, 10] for the evaluation of fracture energy in wood for pure opening mode, Figure [7.2]. The specimen is made of three parts, glued together. The fiber direction of the central part is perpendicular to the direction of the beam axis. This central piece is provided with an initial notch up to approximately 50 - 60% of the beam height. The length of the notch is essential for the instability characteristics of the beam and the tendency is towards greater risk of instability the shorter the notch, Figure (7.2).

It is rather simple to establish a two-dimensional FE-model of this mode I specimen. The notch depth, a_0, was made equal to 48 mm. From the material parameters the material characteristic length is estimated to $l_{ch} \approx 3mm$. A suitable element size may be taken as $\frac{l_{ch}}{5}$ to $\frac{l_{ch}}{10}$ which suggest that the element size should be 0.3 to 0.6 mm. A convergence study, Figure (7.6) reveals that the results (limit load and mid-side displacement) converge quickly, from approximately 68% and 55% error in force and displacements respectively, with element size 10×10 mm to approximately 7% error with element size 5×5 mm. With the element size 2.5×2.5 mm we are down to an error of 0.5 % to 1.5 %. A further subsequent refinement of the mesh does not reveal any dramatic changes in the results but the absolute maximum element size for determining the limit load seems, for the present shape of the $\sigma - \delta$ curve, to be of the same size as the characteristic length of the material, l_{ch}. For the model in Figure (7.6) the load is applied as a point load. By modelling the support as a piece of steel stretching over an area of one fourth of the beam height and applying the load as a uniformly distributed, the limit load increases while the corresponding displacement decreases. In the present model this difference is not of any great proportions, with difference in results in the vicinity of 1%. It is, however, important to model the boundary conditions as accurately as possible when the computations include non-linear effects. This is especially important when comparing numerical calculations and experimental results in order to calibrate the input parameters in the model.

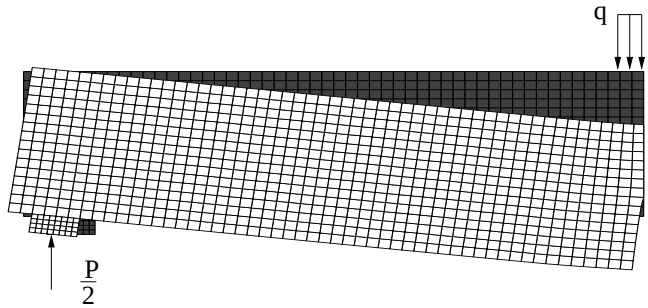

Figure 7.3: Mesh with 5×5 mm elements, mesh density M= $\frac{h}{5} = 16$

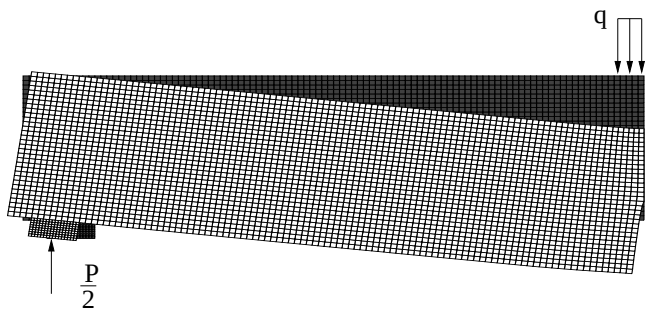

Figure 7.4: Mesh with 2.5 × 2.5 mm elements, mesh density M= $\frac{h}{2.5} = 32$

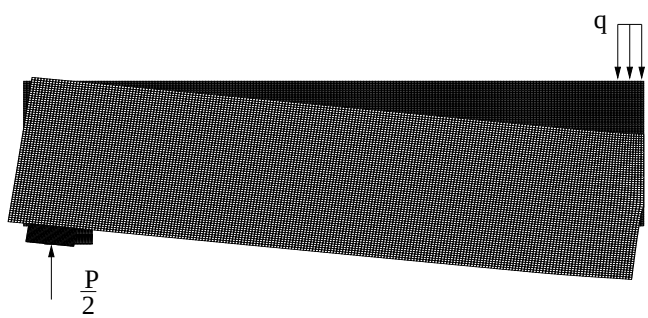

Figure 7.5: Mesh with 1.25 × 1.25 mm elements, mesh density M= $\frac{h}{1.25} = 64$

An unexpected behavior appeared in the convergence study where the displacement curve, Figure (7.7), appears to have a local minimum for mesh density $M = 16$ and local maximum for $M = 64$. The limit force curve shows a similar behavior. The interesting thing is that neither displacements nor forces approach the limit value in a similar manner. Bearing in mind that the results are upper limit solutions and that the size of the fracture process zone is not constant during the computations one has to admit that these variations are of minor importance. The fact that the size of the fracture process zone approaches a constant size with subsequently increasing

mesh refinement supports the convergence behavior and therefore no attempts will be made to investigate further mesh refinement.

With assumed fracture energy of $300Nm/m^2$ the numerical results gave a maximum load of $250N$ at a displacement of $2.28mm$ which is very close to experimental results. In experimental research reported by Gustafsson [6] the measured mean value for

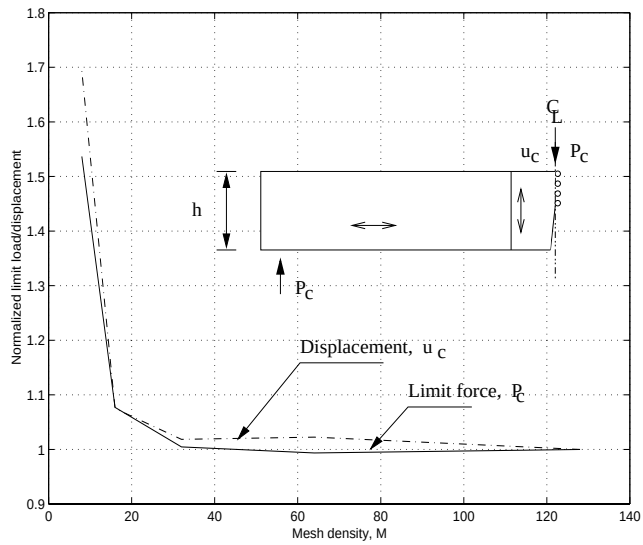

Figure 7.6: Performance of three-point bending test with varying mesh density

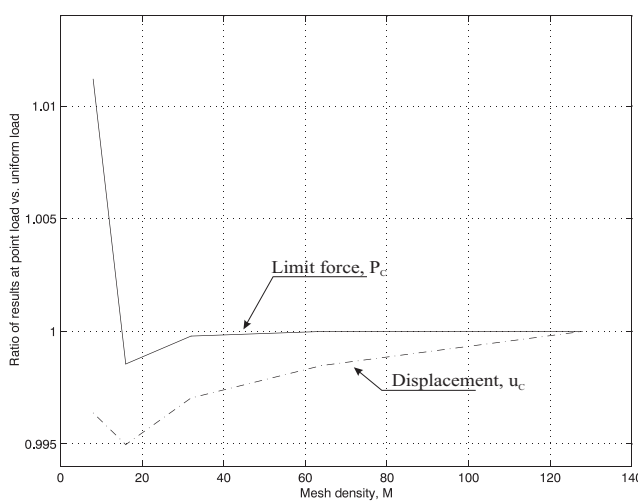

Figure 7.7: Difference in results depending on load configuration and boundary conditions

the fracture energy was $294Nm/m^2$ and a mean value, for the maximum load, of $225N$ was reached. Similar results are reported by Petersson [9].

7.2.2 Four point bending test

The four-point bending test is a test setup arranged for an experimental investigation of crack propagation starting from a defect such as a knot. The specimen is supplied with a vertical notch in the symmetry plane and subjected to a bending moment in the central part. The crack will start from the notch and propagate at nearly constant load. Load-deflection relations obtained from a LEFM model are presented in Figure (7.8). The mean crack propagation load from experimental tests is also indicated, showing a fairly good agreement. The model results are given for two cases, one for $G_c = G_{cI}$ and the other for mixed mode conditions $G_c = G_{c,mixed}$ according to the fracture criteria of Petersson [8]. The beam geometry was: $h = 170mm$; $b = 45mm$; the total length $l = 3000mm$; $a_0 = 42mm$ and the distance from support to the load P was $1000mm$. The element size was $3.25mm$ along the crack path and the material data was according to Table (5.1) in section (5.3).

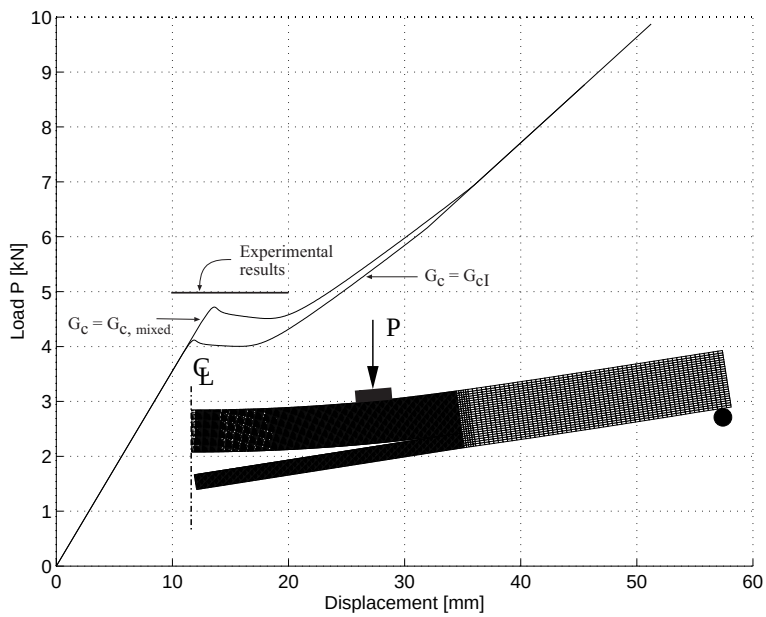

Figure 7.8: Results of four-point bending test FPB.

7.3 Numerical results

7.3.1 Introduction

The parameter studies in the subsequent sections are mostly presented in a diagram in which a relative force is plotted versus the parameter being investigated. A reference beam according to Figure (7.9)is used. The calculated ultimate load of this end-notched beam with $h = 200mm$ is used as a reference load in the presentation of some of the parameter studies. Other parameters for the reference beam are: $\alpha = 0.75$; $\beta = 0.5$; $\rho = 0.0$; $\theta = 0.0$ and $\gamma = 2.667$. Material data according to Table (5.1) in section (5.3) was used throughout the LEFM studies where the smallest element size was $3.125mm$.

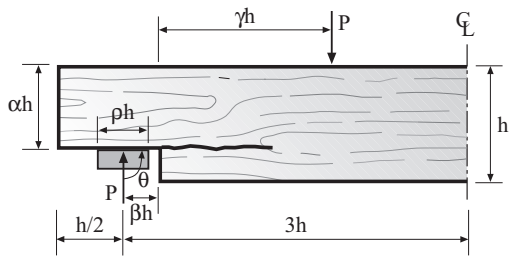

Figure 7.9: End-notched beam parameters

7.3.2 Load-bearing capacity

The load-bearing capacity has been calculated with LEFM for six types of beams, Figure (5.6). All beam geometries are of the same size with a height $h = 600mm$, depth $t = 120mm$ and a total length of $l = 4200mm$. Only half of the beam is modelled and the force versus crack length is determined.

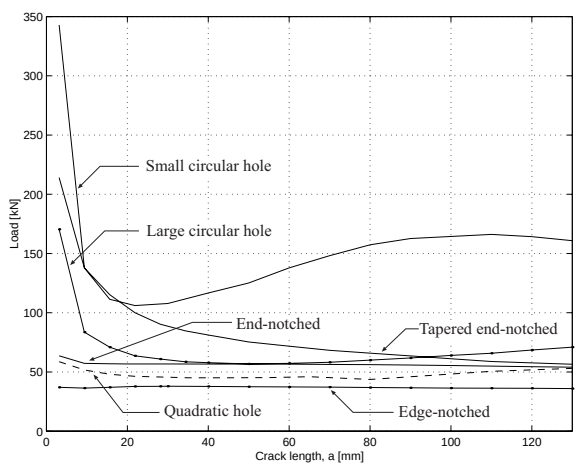

Figure 7.10: Load-bearing capacity of all geometries, h=600mm

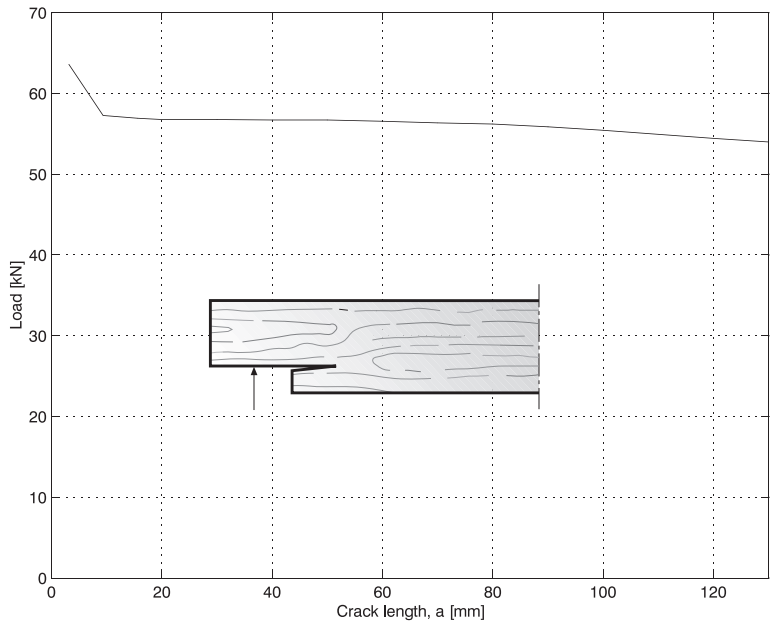

Figure 7.11: Load-bearing capacity of an end-notched beam, $h = 600mm$

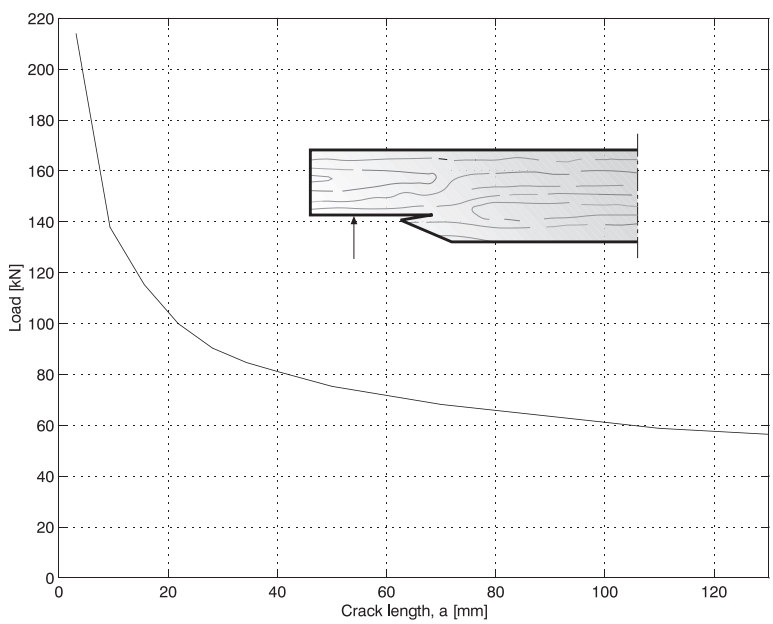

Figure 7.12: Load-bearing capacity of an tapered end-notched beam, $h = 600mm$.

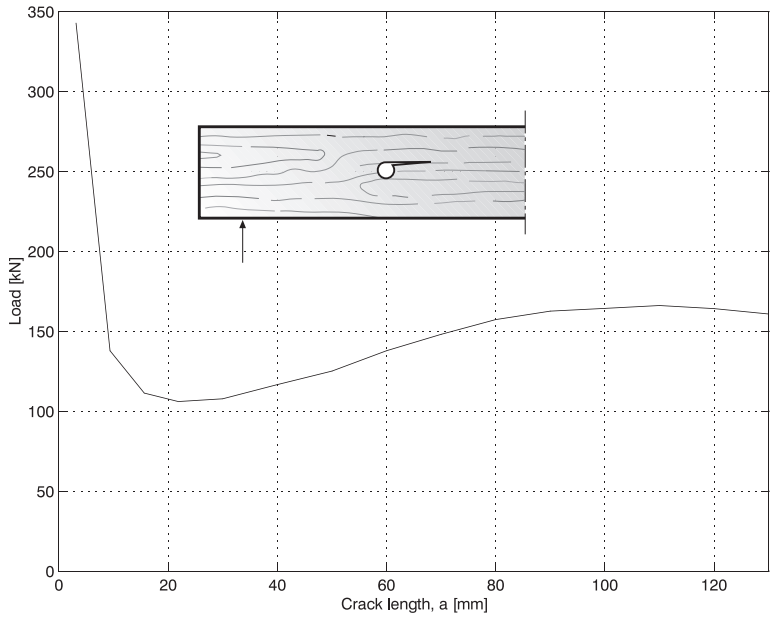

Figure 7.13: Load-bearing capacity of a beam with small internal circular hole, $h = 600mm$.

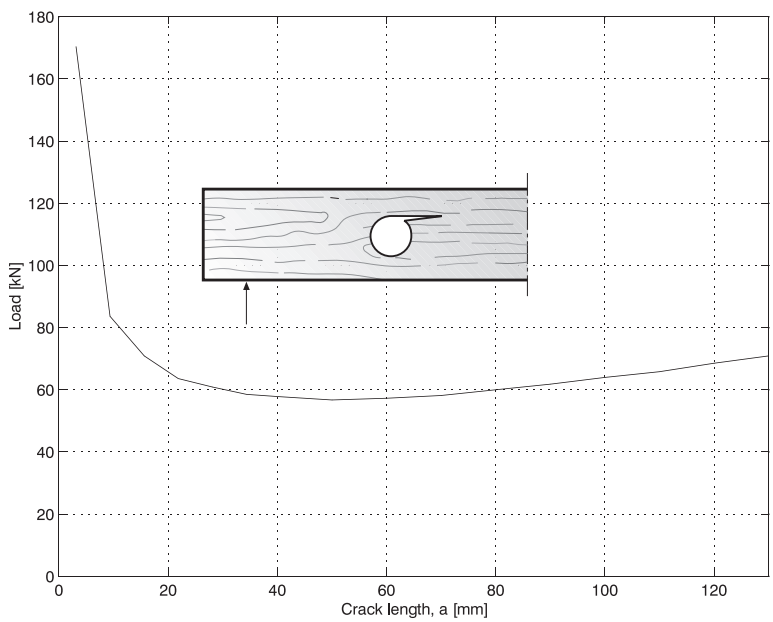

Figure 7.14: Load-bearing capacity of a beam with large internal circular hole, $h = 600mm$.

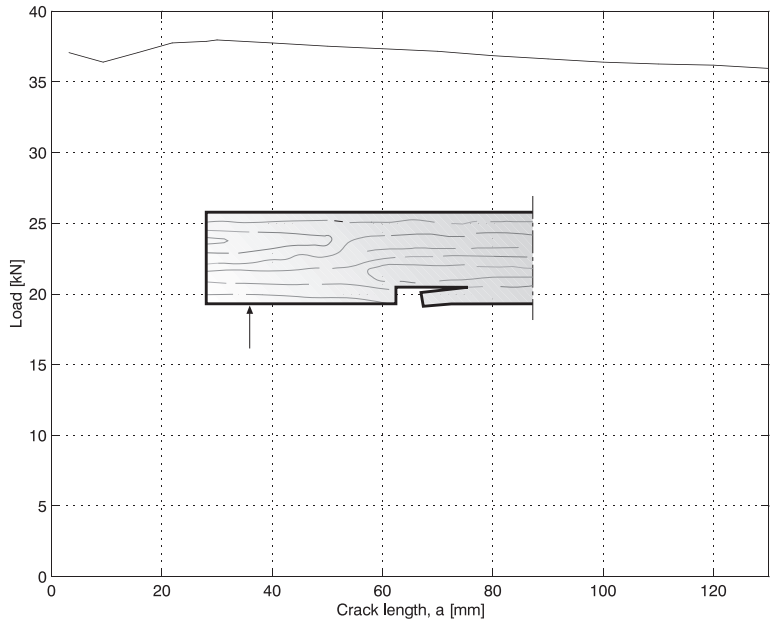

Figure 7.15: Load-bearing capacity of an edge-notched beam, $h = 600mm$.

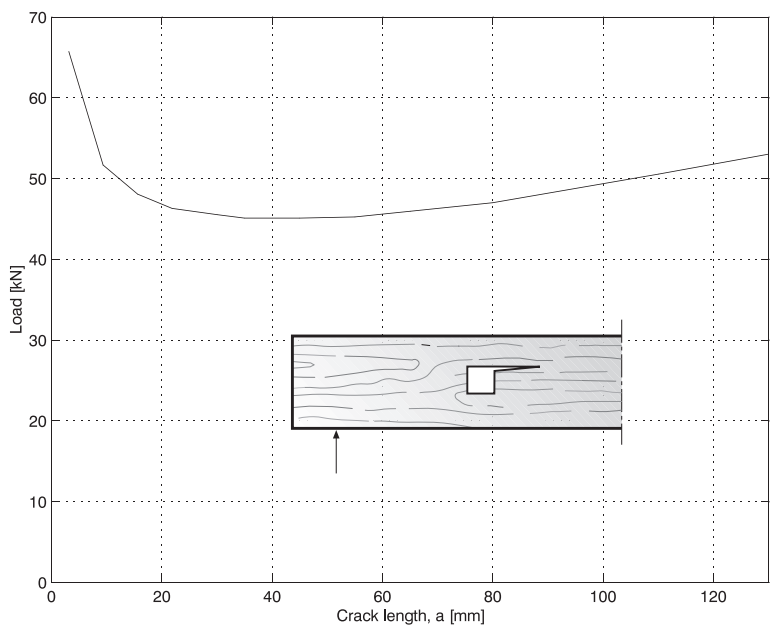

Figure 7.16: Load-bearing capacity of a beam with an internal quadratic hole, $h = 600mm$.

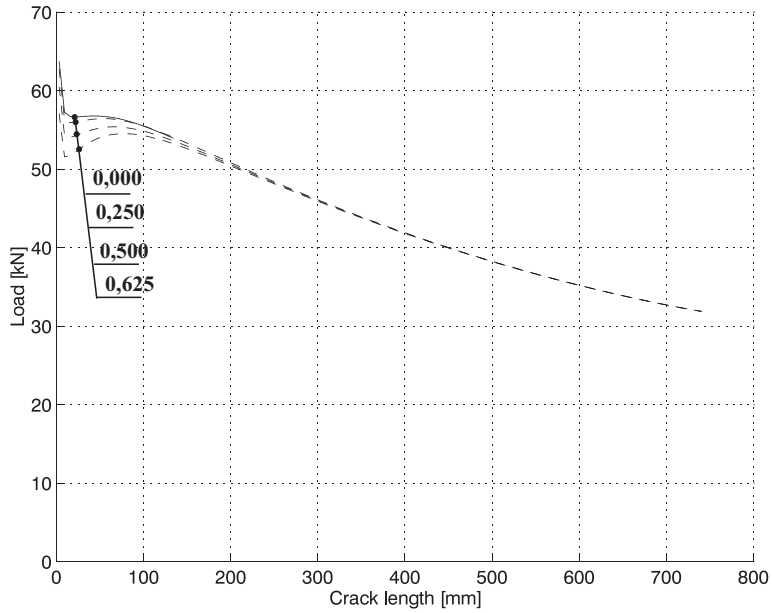

Figure 7.17: Effects of load distribution, ρ, at support (end-notched beam)

7.3.3 Distribution of load at support

Calculations were carried out on an end-notched beam in order to study the effect of distributed load at support. The common practice is to assume that the support is supplied by a concentrated point load. This is almost never the case in practice. Load at support is more or less distributed through mechanical fasteners or a contact surface of some kind. LEFM model has been applied on an end-notched beam with a total depth of $h = 600mm$ where the load at support is applied as a distributed load and a point load as well. The location of the resultant support force remains the same throughout. The results are presented in Figure (7.17) indicating that the crack propagation load becomes somewhat lower for crack lengths less than approximately $h/6$ with the relative load-bearing capacity down to 0.946. It is also interesting to observe that the fracture process is no longer immediately unstable as in the case of a point load.

The load distribution effect was investigated further with the non-linear model. Three geometrically similar beams, with different depths ($h = 100mm, h = 200mm$, $h = 400mm$), were investigated. The results in Figure (7.18) indicate similar tendency in decline of load-bearing capacity. The most interesting part is when the load is in the vicinity of the notch corner or when ρ is close to 2/3. The largest relative reduction in load-bearing capacity seems to be close to 0.034.

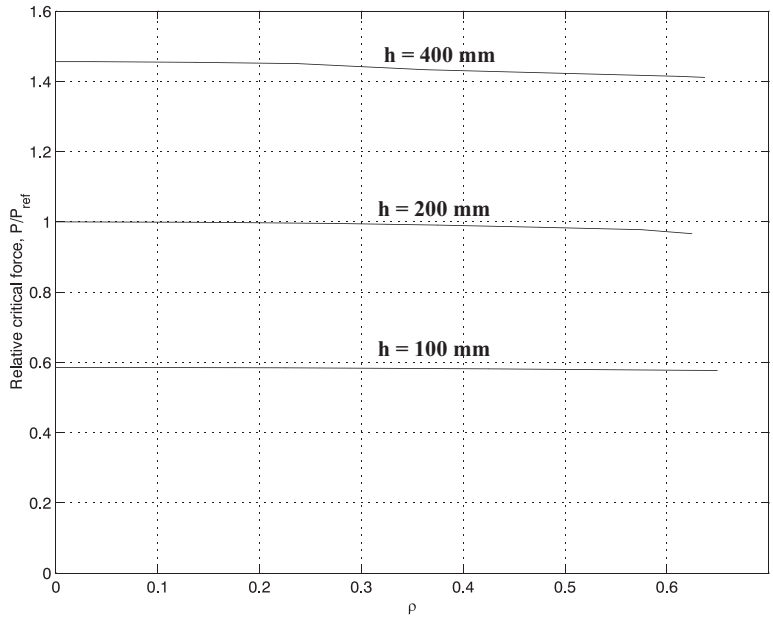

Figure 7.18: Effects of load distribution at support, ρ.

7.3.4 Influence of the geometry of the notch

The geometry of the notch or hole causing the singularity was investigated to some extent by NLFM for an end-notched beam and a beam with a square internal hole.

The influence of variation in notch depth, α, on the relative load-bearing capacity of an end-notched beam is presented in Figure (7.19). As expected the load-bearing capacity drops rapidly with increasing notch depth, especially for α greater than 0.75. For the higher values of α the drop is approximately $13 - 14$ times more rapid than for the lower values.

The length of the notch was also investigated. The distance between notch and support, β, varies from $\beta = 0.0$ up to $\beta = 0.85$. In most practical cases the support is within the distance of $0.1h$ from the end of the beam. The results are presented in Figure (7.20). The influence of the notch length, β, is considerable. For values of β less than approximately 0.02 the load-bearing capacity descends.

7.3.5 Influence of load configuration

The influence of the location of a point load has been investigated [43] with a NLFM model of an end-notched beam. The results indicate strong influence of the location of the load. A point load moves from the center of the beam towards the notch. The influence of the location of the load, see Figure (7.20) and Figure (7.21), becomes apparent when the load is in the vicinity of a beam depth h from the singularity. For distances within h form the notch the critical load ascends rapidly. As the

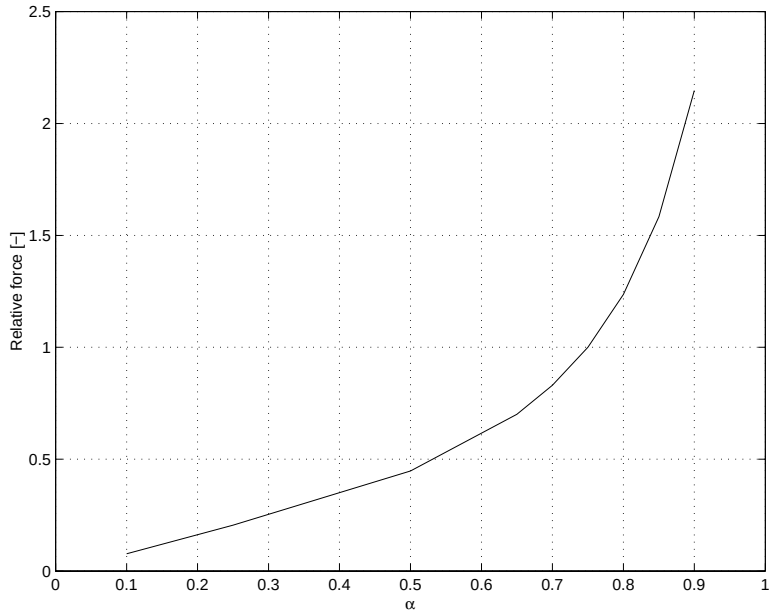

Figure 7.19: End-notched beam. Influence of variation in α.

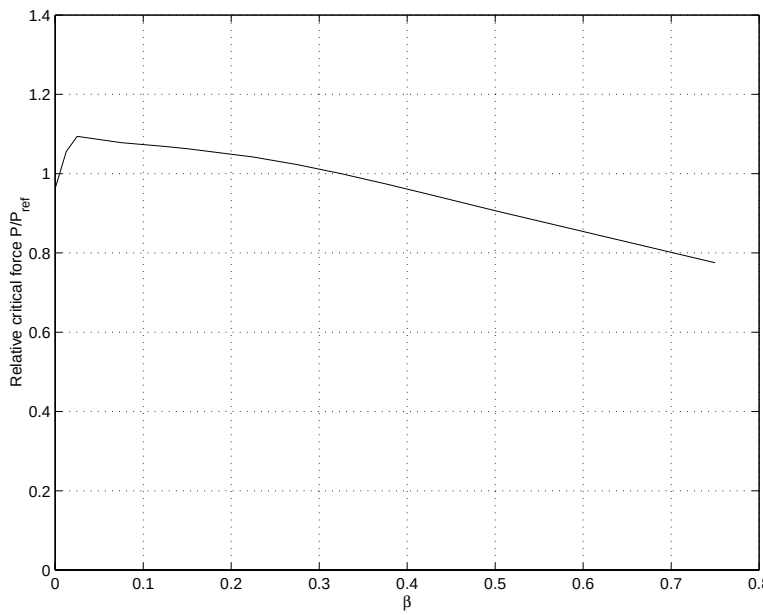

Figure 7.20: Influence of notch length, β. Support is h/20 from beam end.

load comes closer to the notch it runs more and more straight down to the support resulting in less tension perpendicular to grain at the tip of the notch. Also the fracture process becomes increasingly more stable.

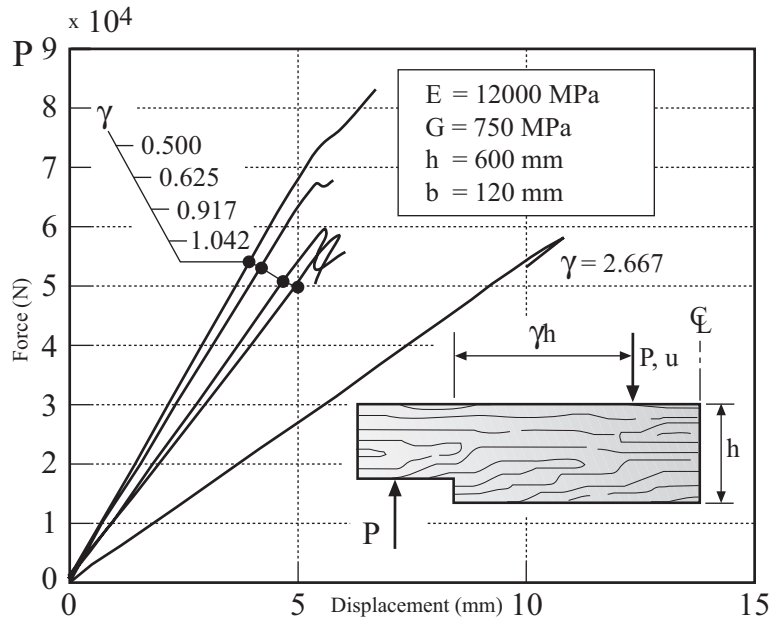

Figure 7.21: Fracture instability of an end-notched beam. FE-computations were terminated when maximum load was attained

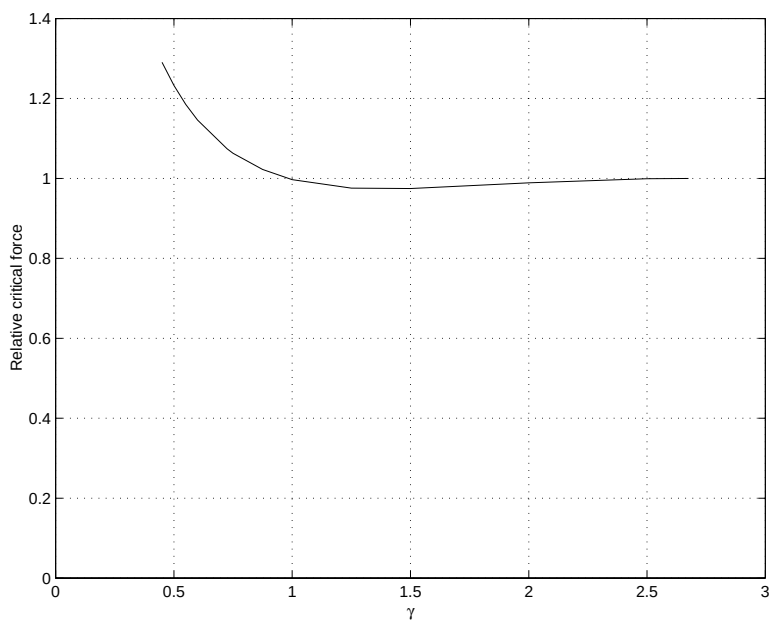

Figure 7.22: Influence of point load configuration, γ

7.3.6 Influence of axial force

The influence of axial forces on an end-notched beam was investigated by NLFM. The angle θ is indicated in Figure (7.9). When the force, P, is perpendicular to support $\theta = 0$ with positive values measured counterclockwise. Axial tension is imposed on the beam with positive values of θ and axial compression with negative values of θ. At the angle of 45° the shear and axial forces are equal. The curve seems to be descending linearly from $-10°$ up to 45°. For values below $-10°$ the curve takes on a convex parabolic form. It is known that at $\theta = 0$ we have a mixed mode situation in the fracture process zone. With increasing axial compression the shear forces in the fracture process zone will decrease resulting in increased load-bearing capacity.

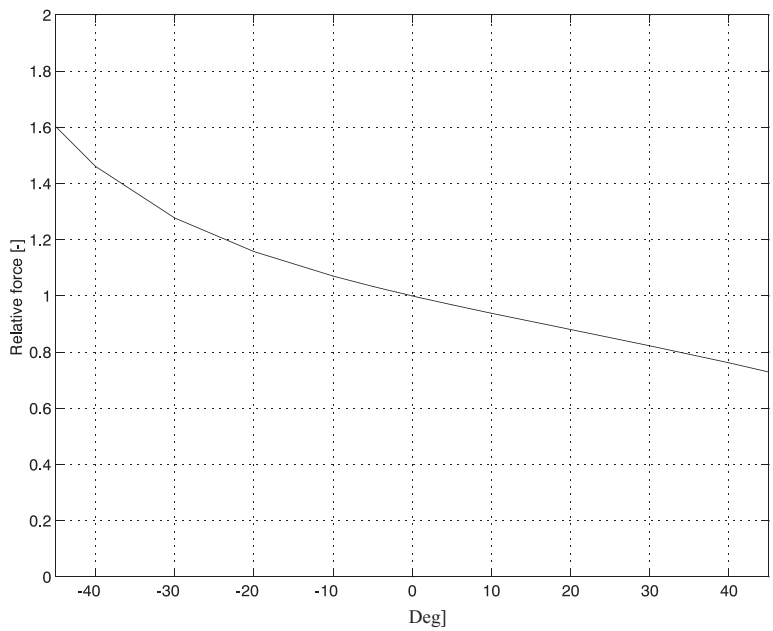

Figure 7.23: Influence of axial force

Chapter 8

Concluding Remarks

8.1 General discussion

In this report both experimental and numerical work concerning the fracture of timber beams is presented. The experimental work presented involves both small specimen testing and testing of structural elements (beams). The small specimen test results were used for determining or verifying the choice of constitutive relation for the fracture elements in the modelling. The test result of timber beams with a mid-section notch was compared with corresponding results from numerical computations.

The results of the LEFM calculations may be utilized to determine critical crack length as well as the ultimate load. Comparing the results for an end-notched beam presented in Figure (7.11) by LEFM and in Figure (7.21) by NLFM it is found that the ultimate loads are close to 58 kN in both cases. The nonlinear calculations were primarily aimed at determining the influence of different parameters on the load-bearing capacity. These calculations were made for beam depths up to 400mm.

8.2 Design considerations

The numerical results presented may be utilized for determining practical evaluation for the influence of different parameters on the load-bearing capacity. Generally, it seems convenient to express the influence of different parameters as:

$$P = P_0 k \tag{8.1}$$

where P is the actual load-bearing capacity and P_0 is the load-bearing capacity of the reference beam.

As an example Figure (7.17) represents results for an end-notched beam with a depth of $h = 600mm$. Here, it may be observed that the difference in ultimate load between the curve for a point load and the curve for a distributed load stretching close to the corner of the notch is close to 4.1%. Similar results may be extracted from Figure (7.18). In the case of a beam with $h = 400mm$ this difference is close to 3.2%. For the beam with $h = 100mm$ the result is 2.3%. In the case of influence of distributed load at support the factor k may be defined as a constant.

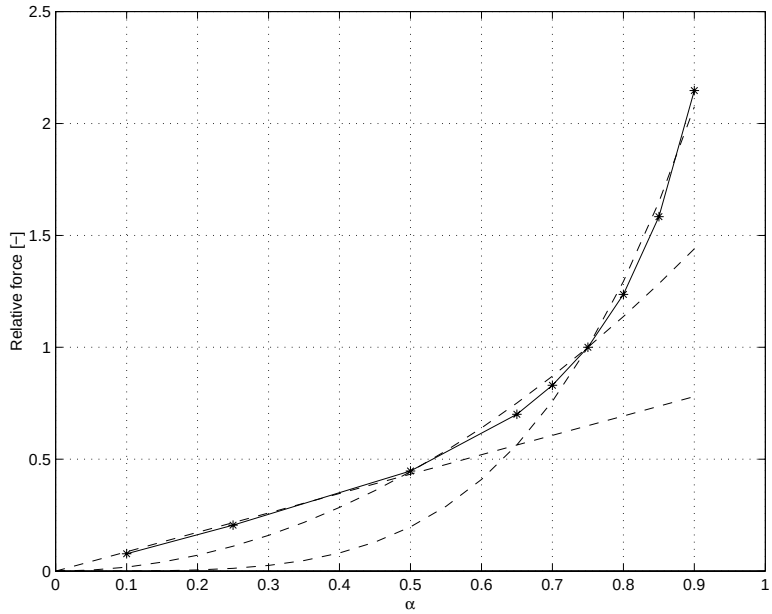

Figure 8.1: End-notched beam. Approximation of load-bearing capacity

In Figure (7.19) the influence of notch depth is shown with the relative force set to unity at $\alpha = 0.75$. As an example, this influence of notch depth may be approximated by

$$k = (\frac{\alpha c}{0.75})^n \tag{8.2}$$

where n and c are

$$\begin{array}{llll} n = 4 & c = 1 & for & \alpha > 0.75 \\ n = 2 & c = 1 & for & 0.485 < \alpha < 0.75 \\ n = 1 & c = 0.67 & for & \alpha < 0.485 \end{array} \tag{8.3}$$

The equation for the influence of α may of course be more or less different if some other reference beam is used with, for instance, some other value β than 0.5.

8.3 Conclusions

The main results of the present study can be put in two categories, enhancement of numerical procedures and presentation of structural behavior.

A constitutive relation for crack elements has been presented on the form of a polylinear function which is easy to implement in FE-programming.

By utilizing fracture mechanics it is possible to study the behavior of structural members with holes and notches. The results presented here suggest that it can be quite convenient to make use of numerical parameter studies, supported by experimental results, for the enhancement of building codes.

8.4 Potential future research

The approach to numerical implementation of fracture mechanics, adopted here, implies possibilities in various fields of wood mechanics. It is, for instance, simple to utilize the method on dowel joints or just a straight forward push over analysis [74, 75] of structures. The numerical process may be regarded as rather slow but the accuracy and reliability rather good.

By implementing the numerical procedure in analysis of mechanical timber joints, various parameters may be studied. The procedure can be adjusted to fracture process including both failure in mechanical fasteners as well as cracking in the structural member. It is also of major interest to study various methods for strengthening structural members with holes and notches.

Several ideas on improving the non-linear modelling have emerged. For some applications, the unloading branch of the stress versus deformation performance of the wood needs to be implemented. Also, implementation of an algorithm with respect to non-linear geometrical effects can be needed for analysis of mechanical joints with a ductile performance before development of unstable crack propagation and a sudden tensile or shear fracture perpendicular to grain.

Bibliography

[1] Bäcklund, Jan.:
Fracture mechanics (in Swedish)
Linköping 1977.

[2] Bodig, J and Jayne, B.A.:
Mechanics of wood and wood composites.
Van Nostrand Reinhold,
New York 1982

[3] Gullander, J.:
Fracture mechanical analysis of wooden beams with the Finite Element Method (in Swedish)
Master thesis, TVSM-5059,
LTH 1995

[4] Gustafsson, P.J.(editor):
Timber fracture mechanics model for strength analysis of beams
RILEM (TC 133-TF) Technical report-In preparation

[5] Gustafsson, P.J:
Fracture mechanics studies of non-yielding materials like concrete
Modelling of tensile fracture and applied strength analyses,
Doctoral thesis, Report TVBM-1007,
LTH Lund University, (1985)

[6] Gustafsson, P.J, Enquist, B.:
Strength of a wooden beam at right angle notch
Technical report, TVSM-7042,
LTH Lund University, (1988)

[7] Hallström, S.E.:
A generalised fracture mechanics approach to fracture initiated at corners
Doctoral thesis, Report No.97-31,
Department of Aeronautics, Division of Lightweight Structures, Royal Institute of Technology (KTH), Stockholm 1997

[8] Petersson, H.:
Fracture mechanics models for strength analysis of timber beams with a hole or a notch
Paper 3: *Energy Release Rate Analysis* LTH, Lund University

[9] Petersson, H.:
Analysis of fracture propagation
COST 508 Wood mechanics workshop, Bordeaux, april 1992
Division of Structural Mechanics, LTH, Lund University (1992)

[10] Petersson, H.:
Fracturing, material softening and finite element analysis
Report TVSM-7036, Division of Structural Mechanics, LTH, Lund University (1988)

[11] Petersson, H.:
Fracture mechanics - An integral view from micro- to macrostructure
International COST 508 Wood Mechanics Conference,
Division of Structural Mechanics, LTH, Lund University (19??)

[12] Petersson, H. and Wernersson, H.:
Analysis of wooden connections and adhesive joints with regard to fracturing behaviour
COST C1 Workshop, Strasbourg, october 28-30, 1992,
Division of Structural Mechanics, LTH, Lund University (1992)

[13] Petersson, H.:
Fracture design analysis of wooden beams with holes and notches
International Council for Building Research Studies and Documentation,
Working Commission W18 - Timber Structures,
Meeting twenty-eight, Copenhagen , april 1995,
Division of Structural Mechanics, LTH, Lund University (1995)

[14] Olsson, N.:
Glulam timber arches - Strength of splices and reliability-based optimisation
Doctoral thesis, Report 2001:12,
Department of Civil and Mining Engineering, Division of Timber Structures,
Lule University of Technology, (2001).

[15] Hearmon, R.F.S.:
Elasticity of wood and plywood
Special report on Forest Products Research, No 7,
London 1948

[16] Hellan, Kåre.:
Introduction to fracture mechanics
McGraw-Hill, 1984

[17] Hellen, T.K.:
On the method of virtual crack extensions
International Journal for Numerical Methods in Engineering, Vol.9,187-207, 1975

[18] Hibbit, Karlsson & Sorenssen, Inc.:
ABAQUS user's manual, Ver 5.4.
USA, 1992

[19] Hori, M. and Vaikuntan, N.:
Rigorous of crack path in two-dimensional elastic body
Mechanics of Materials, pp 1-14, (1997).

[20] Kanninen, M.F., Popelar, C.H.:
Advanced fracture mechanics
Oxford University Press, 1985

[21] Kollmann, Franz F.P., Core, W.A.:
Principles of wood science and technology, I. Solid Wood
Springer-Verlag, 1968

[22] Lekhnitskii, S.G.:
Anisotropic plates
Gordon and Breach, Science Publishers, New York 1968

[23] Ottosen, N.S. and Petersson, H.:
Introduction to the finite element method.
Prentice Hall, New York 1992.

[24] Paris, P.C. and Sih, G.C.:
Stress analysis of cracks
Fracture toughness testing and its applications, ASTM 381,
Prentice Hall, New York 1992.

[25] Sih, G.C., Paris. P.C. and Irwin, G.R.:
On cracks in rectlinearly anisotropic bodies.
International Journal of Fracture mechanics, Vol 1 (1965), pp. 189-200, 1965.

[26] Sih, G.C.:
Mechanics of fracture initiation and propagation
Kluwer Academic Publishers, 1991.

[27] Valentin, G.H. et. al.:
Application of fracture mechanics to timber structures.
RILEM state-of-the-art report, Technical Research Centre of Finland, Research Notes No. 1262,
Espoo Finland 1991.

[28] Wu, E.M.:
Application of fracture mechanics to anisotropic plates.
ASME J. of Applied Mechanics, vol 34 pp 967-974, 1967.

[29] Schellekens, J.C.J.:
Computational strategies for composite structures
Doctoral thesis, Department of Civil Engineering, University of Delft,1992.

[30] Hillerborg, A., Modéer and Petersson, P.E.:
Analysis of crack formation and crack growth in concrete by means of fracture mechanics and finite elements.
Cement and Concrete Research, vol 6, pp 773-782, 1976.

[31] Hillerborg, A.:
Application of fracture mechanics to concrete.
Summary of a series of lectures 1988.
Report TVBM-3030, Division of Building Materials, LTH, Lund university, Lund, 1988.

[32] Wernersson, H.:
Fracture characterization of wood adhesive joints.
Doctoral thesis, TVSM-1006, Division of Structural Mechanics, LTH, Lund University, (1994).

[33] Serrano, E.A.:
Finger-joints for laminated beams
Experimental and numerical studies of mechanical behaviour,
Licentiate thesis, Report TVSM-3021,
Division of Structural Mechanics, LTH, Lund University, (1997).

[34] Heyden, S.:
A network model applied to cellulose fibre materials
Licentiate thesis, Report TVSM-3018,
Division of Structural Mechanics, LTH, Lund University, (1996).

[35] Olson, K.G.:
Joint modelling and roof trusses
Licentiate thesis, Report TVSM-3022,
Division of Structural Mechanics, LTH, Lund University, (1997).

[36] Holmberg, S.:
A numerical and experimental study on initial defibration of wood
Doctoral thesis, Report TVSM-1010,
Division of Structural Mechanics, LTH, Lund University, (1998).

[37] Wald, F. (ed.):
Semi-rigid behaviour of civil engineering structural connections
COST C1, Proceedings of the state of the art workshop, Prague 26-28 october 1994
European Commission Directorate-Genenral XII,Brussels (1994).

[38] LRBB (coordinator):
Duration of load effect on different sized timber beams
Project AIR 2-CT94-1057, Consolidated progress report (1997)
Available at the Division of Structural Mechanics, LTH Lund University.

[39] Blaß, H.J. et.al. (ed.):
Timber engineering, STEP1
Basis of design, material properties, structural components and joints
First edition, Centrum Hout, The Netherlands, (1995).

[40] Blaß, H.J. et.al. (ed.):
Timber engineering, STEP1
Design - Details and structural systems
First edition, Centrum Hout, The Netherlands, (1995).

[41] Svensson, S.:
Internal stress in wood caused by climate variations
Doctoral thesis, TVBK-1013, Department of Structural Engineering, LTH, Lund University, (1997).

[42] Stefansson, F.:
Mechanical properties of wood at microstructural level
Master thesis, TVSM-5057, Division of Structural Mechanics, LTH, Lund University, (1994).

[43] Stefansson,F., Gustafsson,P.J., Petersson,H.:
Fracture analysis of beams with stress concentrations
WCTE98, (1998).

[44] Persson, K.:
Modelling of wood properties by a micromechanical approach
Licentiate thesis, Report TVSM-3020,
Division of Structural Mechanics, LTH, Lund University, (1997).

[45] Persson, K.:
Micromechanical modelling of wood and fibre properties
Doctoral thesis, Report TVSM-1013,
Division of Structural Mechanics, LTH, Lund University, (2000).

[46] Persson, K., Gustafsson, P.J. and Petersson, H.:
Influence of plastic dissipation on apparent fracture energy determined by three-point bending test
Report TVSM-7084, Division of Structural Mechanics, LTH, Lund University, (1993).

[47] Gustafsson, P.J., Enquist, B.:
Strength of a notched wooden beam (In swedish), Report TVSM-7042,
Division of Structural Mechanics, LTH, Lund University, (1988).

[48] Gustafsson, P.J., Petersson, H. and Stefansson, F.:
Fracture analysis of wooden beams with holes and notches
In: Proceedings of the International Wood Engineering Conference,
New Orleans, Louisiana, USA, October 28-31 1996, vol.4 pp.4/281-4/287.

[49] Gustafsson, P.J.:
A study of strength of notched beams
Report CIB-W18A/21-10-1, Meeting twenty one,
Vancouver, Canada, September 1988.
Division of Structural Mechanics, LTH, Lund University, (1988).

[50] Larsen, H.J., Gustafsson, P.J.:
Design of end notched beams
Report CIB-W18A/22-10-1, Meeting twenty two,
Berlin, DDR, September 1989.
Danish Building Research Institute, Denmark (HJL).
Division of Structural Mechanics, LTH, Lund University, (PJG), (1989).

[51] Larsen, H.J., Gustafsson, P.J.:
Fracture energy of wood in tension perpendicular to the grain
Report CIB-W18/24-19-1, Meeting twenty-four,
Oxford, UK, September 1991.
Division of Structural Mechanics, LTH, Lund University, (1991).

[52] Larsen, H.J., Gustafsson, P.J.:
Design of end notched beams
Report CIB-W18A/23-19-2, Meeting twenty-three,
Lisbon, Portugal, September 1990.
Danish Building Research Institute, Denmark (HJL).
Division of Structural Mechanics, LTH, Lund University, (HJL and PJG), (1989).

[53] Jayatilaka, A. de S.:
Fracture of engineering brittle materials
Applied Science Publishers, London, (1979).

[54] Dahlblom, O., Ottosen, N.S.:
Smeared crack analysis using generalized fictious crack model
Journal of Engineering Mechanics, vol. 116, no. 1, pp.55-76, (1990).

[55] Yon, J-H., Hawkins, N.M., Kobayashi, A.S.:
Comparisons of concrete fracture models
Journal of Engineering Mechanics, vol. 123, no. 3, pp.196-203, (1997).

[56] Kitsutaka, Y.:
Fracture parameters by polylinear tension-softening analysis
Journal of Engineering Mechanics, vol. 123, no. 5, pp.444-450, (1997).

[57] Williams, M.L.:
Stress singularities resulting from various boundary conditions in angular corners of plates in extension
Journal of Applied Mechanics, vol. 19, pp.526-528, (1952).

[58] Leicester, R.H.:
Some aspects of stress fields at sharp notches in orthotropic materials, I Plane stress
Division of forest products, techn. paper no. 57, CSIRO, Australia, (1971).

[59] Grenestedt, J.L., Hallström, S. and Kuttenkeuler, J.:
On cracks emanating from wedges in expanded PVC foam
Engineering Fracture Mechanics, vol. 54, no. 4, pp. 445-456, (1996).

[60] Fonselius, M.:
Fracture Mecahnics Testing of Wood
Licentiate thesis,Report no. 92-15, Department of Lightweight Structures, Royal Institute of Technology (KTH), Stockholm (1992).

[61] Boström, L.:
Draft recommendation for determination of fracture energy in forward shear

along the grain in wood
Materials and Structures, Research and testing, vol. 28, no. 182, pp. 482-487, (1995).

[62] Boström, L.:
Method for determination of the softening behaviour of wood and the applicability of a nonlinear fracture mechanics model
Doctoral thesis, Report TVBM-1012, Divison of Building Materials, LTH, Lund university, (1992).

[63] Smith, I. and Chui, Y.H.:
Influence of moisture content on mode I fracture energy of plantation-grown red pine
IUFRO/5.02 Timber Engineering Meeting, Bordeaux, France, august 17-21, (1992)
Wood Science and Technology Centre, University of New Brunswick, Canada

[64] Kretschmann, D.E. and Green, D.W.:
The effect of moisture content on mode I fracture energy for a three-point bending specimen
RILEM Fracture mechanics workshop: "Determination of fracture properties of wood", April 7th, (1992)
U.S.D.A. Forest Service, Forerst products laboratory, Madison, Wisconsin, USA

[65] Karihaloo, B.L.:
Fracture mechanics & structural concrete
Longman Scientific & Technical, UK, (1995)

[66] Bažant, Z.P., Cedolin, L.:
Stability of structures
Oxford University Press, Oxford, (1991)

[67] Illston, J.M., Dinwoodie, J.M. and Smith, A.A.:
Concrete, timber and metals
The nature and behaviour of structural materials
Van Nostrand Reinhold International, Berkshire, England, (1987)

[68] Arfvidsson, J., Dahlblom, O., and Martensson, A:
Internal stesses, cracking and cuping due to wood drying Pilot study, Internal Report TVBM-1012, Division of Building Physics, Divison of Structural Mechanics and Division of Structural Engineering, LTH, Lund university, (1992).

[69] Ormarsson, S.:
Numerical analysis of moisture-related distortions in sawn timber Doctoral thesis, Report 99:7, Department of Structural Mechanics, LTH, Lund University, (1999).

[70] Persson, K, Petersson, H. and Stefansson, F.:
Cell structure modelling for the determination of mechanical properties of wood
Proceedings of the conference on Plant Biomechanics, pp 171-177, Reading, UK (1997).

[71] Tryding, J.:
In-plane fracture of paper Doctoral thesis, Report TVSM-1008, division of Structural Mechanics, LTH, Lund University, (1996).

[72] Cannmo, P.:
Modelling of plasticity and damage in a polycrystalline microstructure
Licentiate Thesis, Report TFHF-1015, Department of Solid Mechanics, LTH, Lund University, (1994).

[73] Nilson, C.:
On nonlocal plasticity, strain softening and localization
Doctoral thesis, Report TVSM-1007, Division of Structural Mechanics, LTH, Lund University, (1994).

[74] Computers and Structures, Inc.:
SAP2000 Nonlinear user's manual, Ver 7.4
Berkeley, California, USA, (2000).

[75] Naeim, F. et al.(ed.):
The seismic design handbook, 2nd ed.
Kluwer Academic Publishers, (2001).

Appendix A

Analytical solutions

A.1 Differential equation for a plane state stress field

The state of equilibrium in a plane body can be described with three stress variables $\sigma_{xx}, \sigma_{yy}, \tau_{xy}$ and two body force variables b_x and b_y, Figure (A.1)

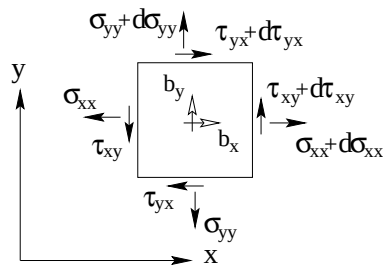

Figure A.1: Components of stress.

$$\begin{aligned} \frac{\partial \sigma_{xx}}{\partial x} + \frac{\partial \tau_{xy}}{\partial y} + b_x &= 0 \\ \frac{\partial \tau_{yx}}{\partial x} + \frac{\partial \sigma_{yy}}{\partial y} + b_y &= 0 \end{aligned} \tag{A.1}$$

where $\tau_{xy} = \tau_{yx}$. All stresses and displacements are regarded as an average over the thickness of the body. Assuming small displacements, the normal strains are derived as

$$\epsilon_{xx} = \frac{\partial u_x}{\partial x}; \quad \epsilon_{yy} = \frac{\partial u_y}{\partial y}; \quad \gamma_{xy} = \frac{\partial u_x}{\partial y} + \frac{\partial u_y}{\partial x} \tag{A.2}$$

These expressions can be differentiated in the following manner

$$\begin{aligned} \frac{\partial^2 \epsilon_{xx}}{\partial y^2} &= \frac{\partial^3 u_x}{\partial x \partial y^2} \\ \frac{\partial^2 \epsilon_{yy}}{\partial x^2} &= \frac{\partial^3 u_y}{\partial x^2 \partial y} \\ \frac{\partial^2 \gamma_{xy}}{\partial x \partial y} &= \frac{\partial^3 u_x}{\partial x \partial y^2} + \frac{\partial^3 u_y}{\partial x^2 \partial y} \end{aligned} \tag{A.3}$$

and by adding terms the condition for the compatibility of deformation is acquired as a single expression

$$\frac{\partial^2 \epsilon_{xx}}{\partial y^2} + \frac{\partial^2 \epsilon_{yy}}{\partial x^2} - \frac{\partial^2 \gamma_{xy}}{\partial x \partial y} = 0 \tag{A.4}$$

The generalized Hooke's law for the state of plain stress or plain strain can be written on component form as

$$\begin{bmatrix} \epsilon_{xx} \\ \epsilon_{yy} \\ \gamma_{xy} \end{bmatrix} = \begin{bmatrix} c_{11} & c_{12} & c_{14} \\ c_{21} & c_{22} & c_{24} \\ c_{41} & c_{42} & c_{44} \end{bmatrix} \begin{bmatrix} \sigma_{xx} \\ \sigma_{yy} \\ \tau_{xy} \end{bmatrix} \tag{A.5}$$

Substituting Eq.(A.5) in Eq.(A.4) results in the compatibility equation of stresses

$$\begin{aligned} &c_{11}\frac{\partial^2 \sigma_{xx}}{\partial y^2} + c_{12}\frac{\partial^2 \sigma_{yy}}{\partial x^2} + c_{14}\frac{\partial^2 \tau_{xy}}{\partial x \partial y} + c_{21}\frac{\partial^2 \sigma_{xx}}{\partial y^2} + c_{22}\frac{\partial^2 \sigma_{yy}}{\partial x^2} + c_{24}\frac{\partial^2 \tau_{xy}}{\partial x \partial y} - \\ &c_{41}\frac{\partial^2 \sigma_{xx}}{\partial y^2} - c_{42}\frac{\partial^2 \sigma_{yy}}{\partial x^2} - c_{44}\frac{\partial^2 \tau_{xy}}{\partial x \partial y} = 0 \end{aligned} \tag{A.6}$$

The equilibrium equation is satisfied by defining an Airy stress function Φ, such that

$$\left.\begin{aligned} \sigma_{xx} &= \frac{\partial^2 \Phi}{\partial y^2} \\ \sigma_{yy} &= \frac{\partial^2 \Phi}{\partial x^2} \\ \tau_{xy} &= -\frac{\partial^2 \Phi}{\partial x \partial y} \end{aligned}\right\} \tag{A.7}$$

Substituting Eq.(A.7) into Eq.(A.6) results in a general 4'th order homogeneous differential equation (PDE) that describes the stress field of a plane anisotropic body in the absence of body forces

$$c_{22}\frac{\partial^4 \Phi}{\partial x^4} - 2c_{24}\frac{\partial^4 \Phi}{\partial x^3 \partial y} + (2c_{12} + c_{44})\frac{\partial^4 \Phi}{\partial x^2 \partial y^2} - 2c_{14}\frac{\partial^4 \Phi}{\partial y \partial x^3} + c_{11}\frac{\partial^4 \Phi}{\partial y^4} = 0 \tag{A.8}$$

If the material is orthotropic and the coordinate axes coincide with the principal directions of elasticity, we obtain $c_{24} = c_{14} = 0$ and the PDE reduces to

$$c_{22}\frac{\partial^4 \Phi}{\partial x^4} + (2c_{12} + c_{44})\frac{\partial^4 \Phi}{\partial x^2 \partial y^2} + c_{11}\frac{\partial^4 \Phi}{\partial y^4} = 0 \tag{A.9}$$

Furthermore, if the material is isotropic, $E_{xx} = E_{yy} = E$ and $G_{xy} = \frac{E}{2(1+\nu_{xy})}$, the stress field is described by the bi-harmonic equation

$$\left.\begin{aligned} \frac{\partial^4\Phi}{\partial x^4} + 2\frac{\partial^4\Phi}{\partial x^2\partial y^2} + \frac{\partial^4\Phi}{\partial y^4} = 0 \\ \nabla^4\Phi = \Delta^2\Phi = 0 \end{aligned}\right\} \tag{A.10}$$

Continuing with the generalized PDE, Eq.(A.10) can be written symbolically with four linear differential operators of the first order

$$D_1 D_2 D_3 D_4 \Phi = 0 \tag{A.11}$$

where

$$D_k = \left(\frac{\partial}{\partial y} - \mu_k \frac{\partial}{\partial x}\right) \qquad (k = 1, 2, 3, 4) \tag{A.12}$$

and μ_k are the roots of the characteristic equation to the PDE

$$c_{11}\mu^4 - 2c_{14}\mu^3 + (2c_{12} + c_{44})\mu^2 - 2c_{24}\mu + c_{22} = 0 \tag{A.13}$$

Dealing with orthotropic materials the characteristic equation simplifies to

$$c_{11}\mu^4 + (2c_{12} + c_{44})\mu^2 + c_{22} = 0 \tag{A.14}$$

and the roots of the PDE appear as

$$\left.\begin{aligned} \mu_3 = \frac{\mu_1}{\overline{\mu_1}} \\ \mu_4 = \frac{\mu_2}{\overline{\mu_2}} \end{aligned}\right\} = \pm\left(-\frac{2c_{12} + c_{44} - \sqrt{(2c_{12} + c_{44})^2 - 4c_{11}c_{22}}}{2c_{11}}\right)^{\frac{1}{2}} \tag{A.15}$$

$$\left.\begin{aligned} \mu_3 = \frac{\mu_1}{\overline{\mu_1}} \\ \mu_4 = \frac{\mu_2}{\overline{\mu_2}} \end{aligned}\right\} = \pm\left(-\frac{2c_{12} + c_{44} + \sqrt{(2c_{12} + c_{44})^2 - 4c_{11}c_{22}}}{2c_{11}}\right)^{\frac{1}{2}}$$

The roots μ_k are either complex or purely imaginary and occur in conjugate pairs $\mu_1, \mu_2, \overline{\mu_1}, \overline{\mu_2}$. For orthotropic materials, three types of solutions are possible given the coordinate axes coincide with the principal axes of elasticity

Case 1	$\mu_1 = \beta i, \quad \mu_2 = \delta i$	*General case for wood*
Case 2	$\mu_1 = \mu_2 = \beta i$	*Isotropic materials and a special case of orthotropic materials*
Case 3	$\mu_1 = \alpha + \beta i, \quad \mu_2 = -\alpha + \beta i$	*Paper*

(A.16)

From the solution of the characteristic equation it is evident that each case, as described above, is governed by a condition which is totally controlled by material parameters

$$\begin{aligned} Case\ 1 \quad & \frac{(2c_{12}+c_{44})^2}{4c_{11}c_{22}} > 1 \\ Case\ 2 \quad & \frac{(2c_{12}+c_{44})^2}{4c_{11}c_{22}} = 1 \\ Case\ 3 \quad & \frac{(2c_{12}+c_{44})^2}{4c_{11}c_{22}} < 1 \end{aligned} \tag{A.17}$$

These conditions will be discussed further in a subsequent section on plane state. In Case 2 it is indicated that this special solution for orthotropic materials also applies to isotropic materials. This is true when $\beta = 1$, i.e. $\mu_1 = \mu_2 = i$. The general solutions to the PDE are different, depending on the roots of the characteristic equation. Defining the variables z_1 and z_2 by

$$\begin{aligned} z_1 &= x + \mu_1 y \\ z_2 &= x + \mu_2 y \end{aligned} \tag{A.18}$$

the general solutions to Eq.(A.10) are

$$\begin{aligned} \mu_1 \neq \mu_2 \quad & \Phi = 2\Re\left[\Phi_1(z_1) + \Phi_2(z_2)\right] \\ \mu_1 = \mu_2 \quad & \Phi = 2\Re\left[\Phi_1(z_1) + \overline{z_1}\Phi_2(z_1)\right] \end{aligned} \tag{A.19}$$

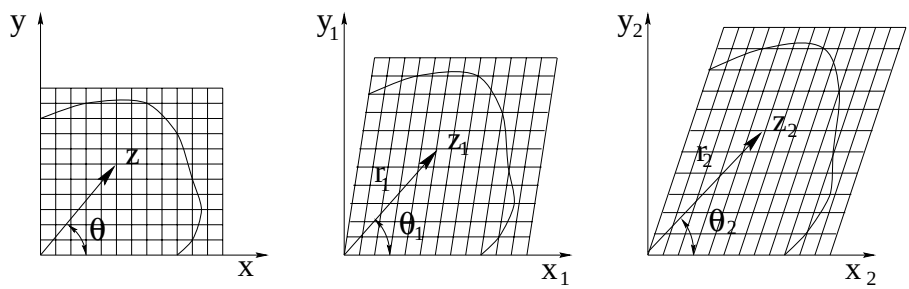

Figure A.2: Real space region and mapped regions.

The functions Φ_1 and Φ_2 are thus defined in the mapped coordinate systems according to Figure (A.2) where

$$\begin{aligned} z_k = x + \mu_k y = x + (\alpha_k + \beta_k i)y = x_k + y_k i \ \ with \\ x_k = x + \alpha_k y \ \ and \ \ y_k = \beta_k y \end{aligned} \tag{A.20}$$

A general expression for the stress and displacement fields of materials according to Case 1 or Case 3 is derived from Eq.(A.2) and (A.7)

$$\left.\begin{array}{l} \sigma_{xx} = 2\Re\left[\mu_1^2\Phi_1''(z_1) + \mu_2^2\Phi_2''(z_2)\right] \\ \sigma_{yy} = 2\Re\left[\Phi_1''(z_1) + \Phi_2''(z_2)\right] \\ \tau_{xy} = -2\Re\left[\mu_1\Phi_1''(z_1) + \mu_2\Phi_2''(z_2)\right] \\ \\ u_x = 2\Re\left[p_1\Phi_1'(z_1) + p_2\Phi_2'(z_2)\right] \\ u_y = 2\Re\left[q_1\Phi_1'(z_1) + q_2\Phi_2'(z_2)\right] \\ \\ where \\ \\ p_k = c_{11}\mu_k^2 + c_{12} - c_{14}\mu_k \\ q_k = c_{12}\mu_k + \dfrac{c_{22}}{\mu_k} - c_{24} \end{array}\right\} \quad (A.21)$$

A.2 Differential equation for the anti-plane problem

In order to be able, subsequently, to describe anti-plane problems involving a crack, it is first necessary to derive a separate differential equation which takes the planar discontinuity into account. In other words, the stress relief behind the crack tip is decisive for the formulation of the differential equation. Physically, the problem can be described as a cylinder with a side crack under torsion. The associated displacements are

$$u_x = u_y = 0 \;\; and \;\; u_z = u_z(x, y) \quad (A.22)$$

The constitutive relation involves only two stress components and two strain components. Assuming small displacements the engineering strains become

$$\begin{bmatrix} \gamma_{xz} \\ \gamma_{yz} \end{bmatrix} = \begin{bmatrix} \dfrac{\partial u_z}{\partial x} \\ \dfrac{\partial u_z}{\partial y} \end{bmatrix} = \begin{bmatrix} c_{55} & c_{56} \\ c_{56} & c_{66} \end{bmatrix} \begin{bmatrix} \tau_{xz} \\ \tau_{yz} \end{bmatrix} \quad (A.23)$$

As all stress components vanish, except τ_{xz} and τ_{yz} the equilibrium equation reduces to

$$\frac{\partial \tau_{xz}}{\partial x} + \frac{\partial \tau_{yz}}{\partial y} = 0 \quad (A.24)$$

Through Eq.(A.2) and the equilibrium equation a 2'nd order differential equation can be derived, in terms of anti-plane displacements $u_z(x, y)$ which can be replaced by a stress function $\Phi_3'(z_k)$ in a similar manner as in the plane case.

$$c_{66}\frac{\partial^2 u_z}{\partial x^2} - 2c_{56}\frac{\partial^2 u_z}{\partial x \partial y} + c_{55}\frac{\partial^2 u_z}{\partial y^2} = 0 \quad (A.25)$$

The PDE can also be written with the aid of differential operators

$$D_5 D_6 u_z = 0 \quad (A.26)$$

where D_k (k=5,6) is defined as previously and μ_k (k=5,6) are the roots of the characteristic equation

$$c_{55}\mu^2 - 2c_{56}\mu + c_{66} = 0 \tag{A.27}$$

where

$$\left.\begin{matrix}\mu_5 \\ \mu_6\end{matrix}\right\} = \frac{c_{56} \pm \sqrt{c_{56}^2 - c_{55}c_{66}}}{c_{55}} \tag{A.28}$$

and as the two solutions are complex conjugate, the solution to the stress and displacement fields can be conveniently described with a single geometrical parameter $z_5 = x + \mu_5 y$. Thus, the general solutions become

$$\begin{gathered}\tau_{xz} = 2\Re\left[\mu_5 \Phi_3''(z_5)\right] \\ \tau_{xz} = -2\Re\left[\Phi_3''(z_5)\right] \\ \textit{and} \\ u_z(z_5) = 2\Re\left[\frac{\mu_5(c_{55}c_{66} - c_{56}^2)}{c_{66} - c_{56}\mu_5}\Phi_3'(z_5)\right]\end{gathered} \tag{A.29}$$

A.3 Stress and displacement field in the vicinity of a crack

In order to derive an expression for the stress and displacement field in the vicinity of a crack tip, it is convenient to make use of the general expressions in Eq.(A.21) and Eq.(A.29). The problem is to find an appropriate form for Φ_k'' and Φ_k'. The following procedure was applied by Paris et al. [24]. Close to a crack tip ($z = z_0$) the function Φ_k'' may be written as

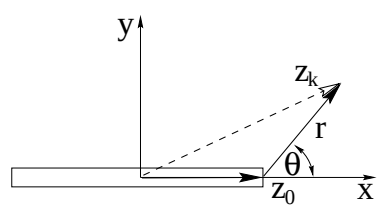

Figure A.3: Notation for the vicinity of a crack tip.

$$\Phi_k''(z_k) = \frac{\Psi_k^{(1)}(z_k)}{\sqrt{z_k - z_0}} + \Psi_k^{(2)}(z_k) + \cdots \qquad (k = 1, 2, 5) \tag{A.30}$$

where, according to Figure (A.3)

$$\left.\begin{matrix}z_k - z_0 = r(\cos\theta + \mu_k \sin\theta) \\ r^2 = x^2 + y^2\end{matrix}\right\} \tag{A.31}$$

with all parameters defined in the real space region, and

$$\Psi_k^{(j)}(z_k) = \sum_{n=0}^{\infty} \lambda_{kn}^{(j)} (z_k - z_0)^n \quad (j = 1, 2;\ k = 1, 2, 5) \tag{A.32}$$

Substitution of Eq.(A.31) and (A.32) into Eq.(A.30), with $n = 0$ results in

$$\Phi_k''(z_k) = \frac{\lambda_{k0}^{(1)}}{\sqrt{r(\cos\theta + \mu_k \sin\theta)}} + \mathcal{O}(r^{\frac{1}{2}}) \tag{A.33}$$

where the last term is disregarded due to the dominating character of the first term in the vicinity of the crack tip. The constants $\lambda_{k0}^{(1)}$ are redefined in terms of stress intensity factors (k), where

$$\left.\begin{aligned} \lambda_{10}^{(1)} &= -\frac{\mu_2}{2\sqrt{2}(\mu_1 - \mu_2)} \left(k_1 + \frac{k_2}{\mu_2}\right) \\ \lambda_{20}^{(1)} &= \frac{\mu_1}{2\sqrt{2}(\mu_1 - \mu_2)} \left(k_1 + \frac{k_2}{\mu_1}\right) \\ \lambda_{30}^{(1)} &= -\frac{k_3}{2\sqrt{2}} \end{aligned}\right\} \tag{A.34}$$

Substituting Eq.(A.33) and (A.34) into Eq.(A.21) and (A.29) results in

$$\begin{aligned} \sigma_{xx} = \quad & 2\Re\left[\mu_1^2 \frac{-\mu_2\left(k_1 + \frac{k_2}{\mu_2}\right)}{2\sqrt{2}(\mu_1 - \mu_2)\sqrt{r(\cos\theta + \mu_1 \sin\theta)}} + \mu_2^2 \frac{\mu_1\left(k_1 + \frac{k_2}{\mu_2}\right)}{2\sqrt{2}(\mu_1 - \mu_2)\sqrt{r(\cos\theta + \mu_2 \sin\theta)}}\right] = \\ & \frac{k_1}{\sqrt{2r}}\Re\left[\frac{\mu_1\mu_2}{\mu_1 - \mu_2}\left\{\frac{\mu_2\left(1 + \frac{k_2}{k_1\mu_1}\right)}{\sqrt{\cos\theta + \mu_2 \sin\theta}} - \frac{\mu_1\left(1 + \frac{k_2}{k_1\mu_2}\right)}{\sqrt{\cos\theta + \mu_1 \sin\theta}}\right\}\right] = \\ & \frac{k_1}{\sqrt{2r}}\Re\left[\frac{\mu_1\mu_2}{\mu_1 - \mu_2}\left\{\frac{\mu_2}{\sqrt{\cos\theta + \mu_2 \sin\theta}} - \frac{\mu_1}{\sqrt{\cos\theta + \mu_1 \sin\theta}}\right\}\right] + \\ & \frac{k_2}{\sqrt{2r}}\Re\left[\frac{1}{\mu_1 - \mu_2}\left\{\frac{\mu_2^2}{\sqrt{\cos\theta + \mu_1 \sin\theta}} - \frac{\mu_1^2}{\sqrt{\cos\theta + \mu_1 \sin\theta}}\right\}\right] \end{aligned} \tag{A.35}$$

Consequently

$$
\begin{aligned}
\sigma_{yy} = \; & \frac{k_1}{\sqrt{2r}}\Re\left[\frac{1}{\mu_1-\mu_2}\left\{\frac{\mu_1}{\sqrt{\cos\theta+\mu_2\sin\theta}}-\frac{\mu_2}{\sqrt{\cos\theta+\mu_1\sin\theta}}\right\}\right] \; + \\
& \frac{k_2}{\sqrt{2r}}\Re\left[\frac{1}{\mu_1-\mu_2}\left\{\frac{\mu_2^2}{\sqrt{\cos\theta+\mu_1\sin\theta}}-\frac{\mu_1^2}{\sqrt{\cos\theta+\mu_1\sin\theta}}\right\}\right] \\
\tau_{xy} = \; & \frac{k_1}{\sqrt{2r}}\Re\left[\frac{\mu_1\mu_2}{\mu_1-\mu_2}\left\{\frac{1}{\sqrt{\cos\theta+\mu_1\sin\theta}}-\frac{1}{\sqrt{\cos\theta+\mu_2\sin\theta}}\right\}\right] \; + \\
& \frac{k_2}{\sqrt{2r}}\Re\left[\frac{1}{\mu_1-\mu_2}\left\{\frac{\mu_1}{\sqrt{\cos\theta+\mu_1\sin\theta}}-\frac{\mu_2}{\sqrt{\cos\theta+\mu_2\sin\theta}}\right\}\right] \\
\tau_{xz} = \; & -\frac{k_3}{\sqrt{2r}}\Re\left[\frac{\mu_3}{\sqrt{\cos\theta+\mu_5\sin\theta}}\right] \\
\tau_{yz} = \; & \frac{k_3}{\sqrt{2r}}\Re\left[\frac{1}{\sqrt{\cos\theta+\mu_5\sin\theta}}\right]
\end{aligned}
\tag{A.36}
$$

A.4 Energy rate and stress intensity factors

More about Irwin's and Griffith's theories For materials that are considered brittle the concept of energy rate (G) is strongly attached to stress intensity (K) through material properties. This relationship was derived by Irwin [25] where he proposed that the change in potential energy (Π) of a body equals the work performed by the stresses in the corresponding crack propagation zone (Δa), Figure (A.4). Therefore the energy rates may be calculated as

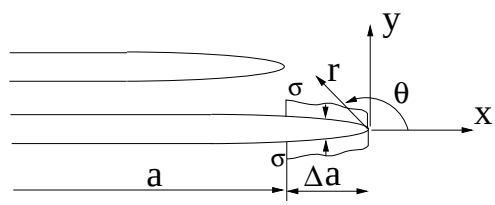

Figure A.4: Calculation of energy release rate.

$$
-\frac{\partial\Pi}{\partial a} = G_i = \lim_{\Delta a\to 0}\frac{1}{\Delta a}\int_0^{\Delta a}\sigma_i(\Delta a - r, 0)\; u_i(r,\pi)dr \quad (i=1,2,3) \tag{A.37}
$$

The substitution of Eq.(A.35) and (A.36) into the integral expression above results in

$$
\begin{aligned}
G_I &= -\frac{K_I^2}{2} c_{22} \Im \left[\frac{\mu_1 + \mu_2}{\mu_1 \mu_2} \right] \\
G_{II} &= \frac{K_{II}^2}{2} c_{11} \Im \left[\mu_1 + \mu_2 \right] \\
G_{III} &= \frac{K_{III}^2}{2} \Im \left[\frac{c_{44} c_{55} - c_{45}^2}{c_{45} - \mu_3 c_{55}} \right]
\end{aligned}
\tag{A.38}
$$

where the modes of fracture are independent. This is achieved by ignoring the coupling terms in the expression for the stress field. For mode I and mode II the energy release, assuming coupling of stresses, becomes

$$
\begin{aligned}
G_I &= -\frac{K_I}{2} c_{22} \Im \left[\frac{K_I(\mu_1 + \mu_2) + K_{II}}{\mu_1 \mu_2} \right] \\
G_{II} &= \frac{K_{II}}{2} c_{11} \Im \left[K_{II}(\mu_1 + \mu_2) + K_I \mu_1 \mu_2 \right]
\end{aligned}
\tag{A.39}
$$

By adding terms, the total energy release rate then results in

$$
G = \sum_{i_I}^{III} G_i \tag{A.40}
$$

For orthotropic materials the relationship between energy release rate and stress intensity factors

$$
G_i = \xi_i K_i^2 \tag{A.41}
$$

is obtained by substituting Eq.(A.38) into Eq.(A.41). The results are shown in Table (2.1) for both orthotropic and anisotropic materials.

	Anisotropic	Orthotropic
Mode I	$\frac{1}{2} \Im \left[-c_{22} \frac{\mu_1 + \mu_2}{\mu_1 \mu_2} \right]$	$\sqrt{\frac{c_{11} c_{22}}{2}} \left[\sqrt{\frac{c_{22}}{c_{11}}} + \frac{2c_{12} + c_{33}}{c_{11}} \right]^{\frac{1}{2}}$
Mode II	$\frac{1}{2} \Im \left[c_{11}(\mu_1 + \mu_2) \right]$	$\frac{c_{11}}{\sqrt{2}} \left[\sqrt{\frac{c_{22}}{c_{11}}} + \frac{2c_{12} + c_{33}}{c_{11}} \right]^{\frac{1}{2}}$
Mode III	$\frac{1}{2} \Im \left[\frac{c_{55} c_{66} - c_{56}^2}{c_{56} - \mu_5 c_{55}} \right]$	$\frac{\sqrt{c_{55} c_{66}}}{2}$

Table A.1: Elastic coefficients, ξ_i (i=I,II,III).

A.5 Plane problems

Dealing with two-dimensional problems of fracture, it is often necessary to choose whether to use the constitutive properties of plane strain or plane stress. In fact, pure state of plane strain or plane stress is not so common and in most cases the governing state is a mixture of both. The geometry of the structure has a great influence on which one of the plane states is dominating. However, it is of some interest to view the influence of different degrees of orthotropy on the stress field and thus being able to predict whether changes in elastic parameters have any substantial effect on the fracture process. The roots of the characteristic equations seem to be an appropriate measure on the degree of orthotropy as in all cases the roots for isotropic materials are $\mu_k = \pm i$. The formulation and derivation of expressions in previous sections has been kept entirely on the level of plane state, i.e. no distinction has been made between plane strain or plane stress and they can therefore be used as general expressions for both states. In the subsequent sections the discussion will only involve isotropy or orthotropy.

A.6 Plane strain

The state of plane strain is described in Ottosen and Petersson [23] as the state where the only non-zero stresses are σ_{xx}, σ_{yy} and τ_{xy}. Then, the constitutive relation becomes

$$\begin{bmatrix} \epsilon_{xx} \\ \epsilon_{yy} \\ \gamma_{xy} \end{bmatrix} = \begin{bmatrix} \dfrac{1-\nu_{xz}\nu_{zx}}{E_{xx}} & -\dfrac{\nu_{yx}+\nu_{yz}\nu_{zx}}{E_{yy}} & 0 \\ -\dfrac{\nu_{xy}+\nu_{xz}\nu_{zy}}{E_{xx}} & \dfrac{1-\nu_{yz}\nu_{zy}}{} & 0 \\ 0 & 0 & \dfrac{1}{G_{xy}} \end{bmatrix} \begin{bmatrix} \sigma_{xx} \\ \sigma_{yy} \\ \tau_{xy} \end{bmatrix} \tag{A.42}$$

As previously mentioned, the roots of the orthotropic characteristic equation differ somewhat depending on material parameters. The general case for wood and similar materials depends on the condition in Eq.(A.43) which, by substituting the compliance components with corresponding material parameters, appears as

$$\frac{E_{xx}E_{yy}\left(-\dfrac{2}{E_{yy}}(\nu_{yx}+\nu_{yz}\nu_{zx})+\dfrac{1}{G_{xy}}\right)^2}{4(1-\nu_{xz}\nu_{zx})(1-\nu_{yz}\nu_{zy})} > 1 \tag{A.43}$$

The condition in Eq.(A.43) may be used as a measure of degree of orthotropy.

Appendix B

Determination of fracture characteristics for wood. Experimental Results

The following experimental results are obtained from small specimen testing in the EMS testing device. The procedure was displacement controlled. For each test the fracture energy in mode I and mode II is obtained.

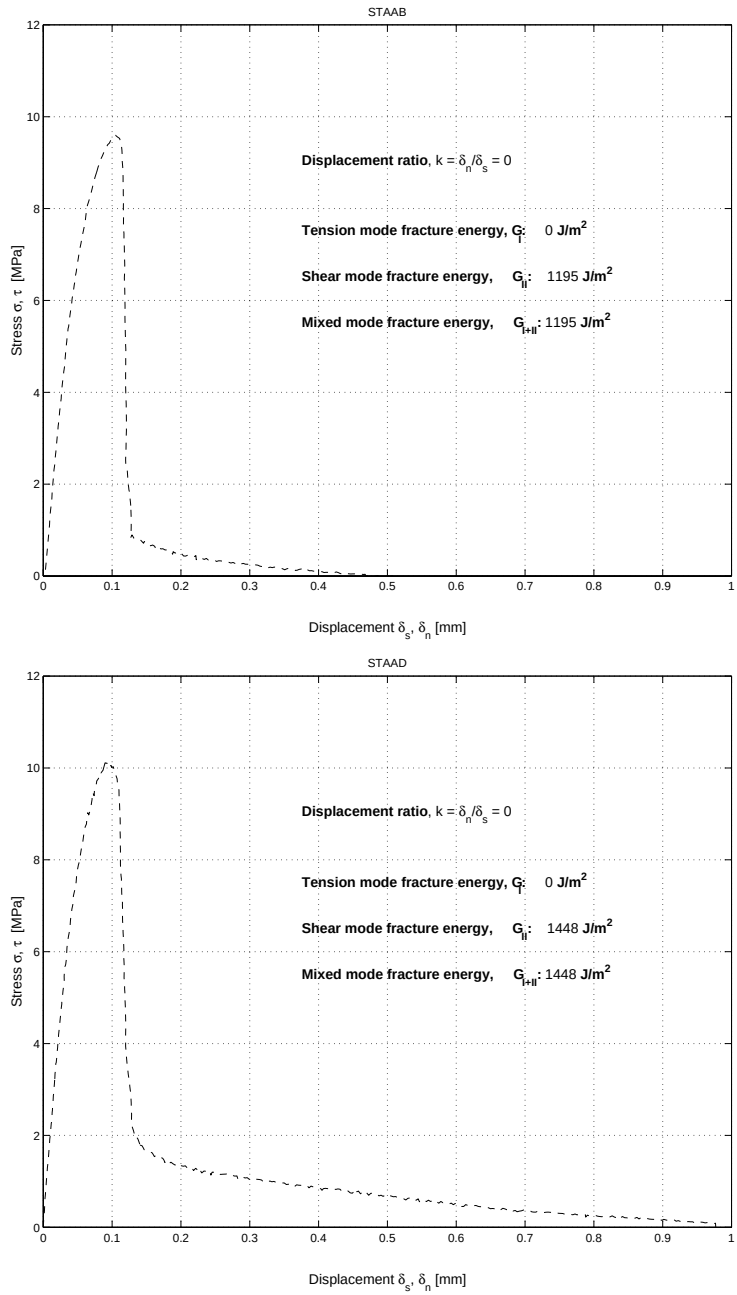

Figure B.1: Stress-displacement diagrams. Displacement ratio $k = \frac{\delta_n}{\delta_s} = 0$

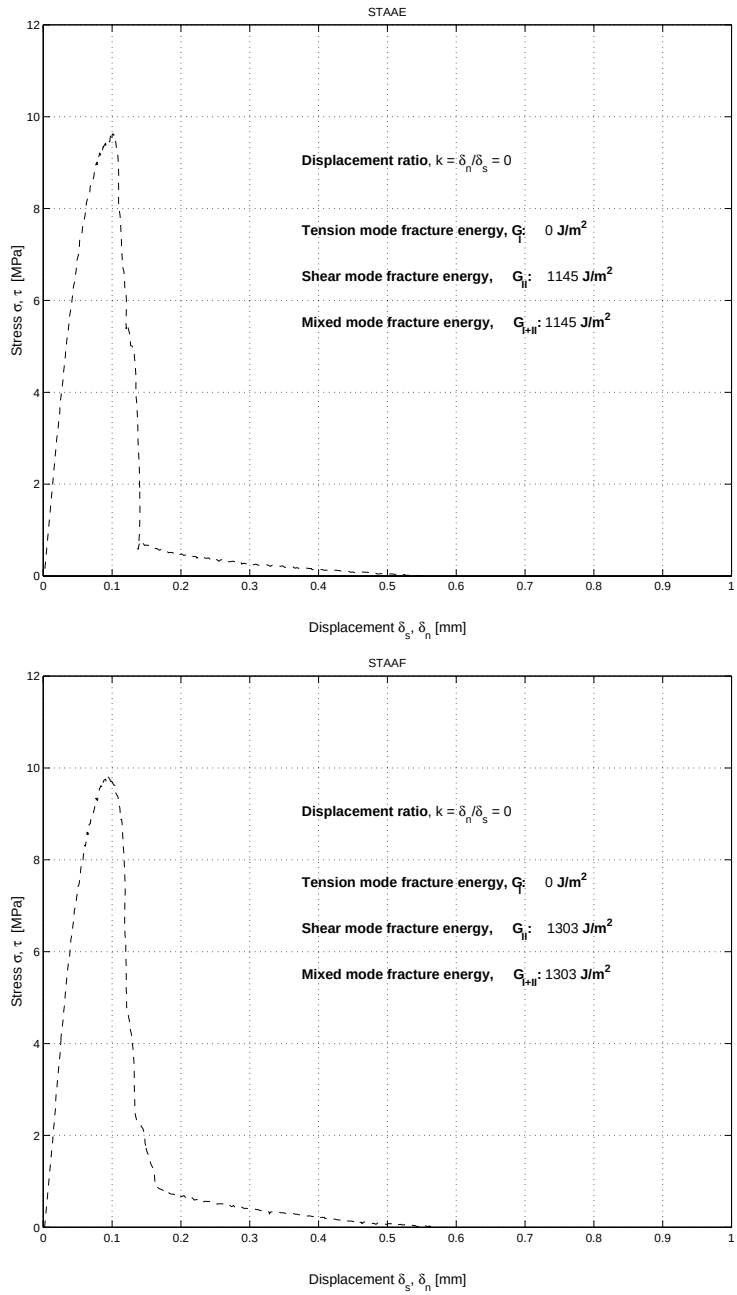

Figure B.2: Stress-displacement diagrams. Displacement ratio $k = \frac{\delta_n}{\delta_s} = 0$

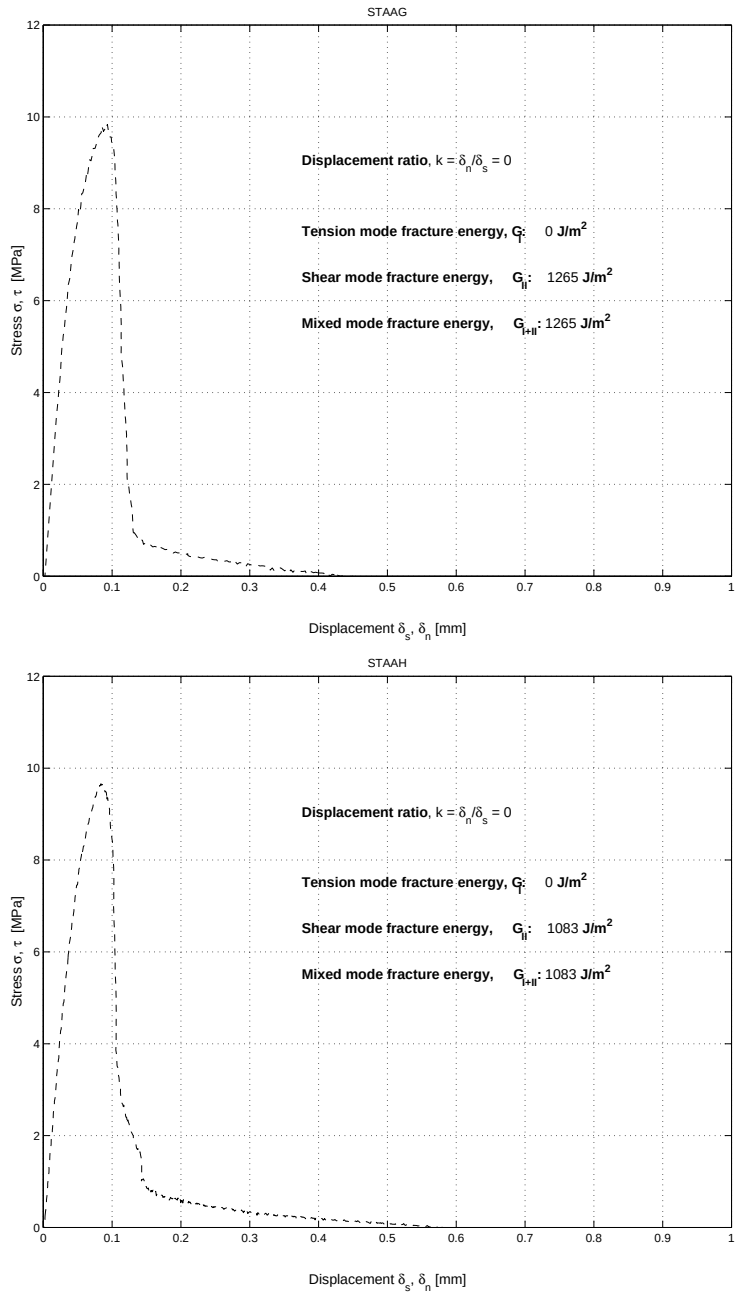

Figure B.3: Stress-displacement diagrams. Displacement ratio $k = \frac{\delta_n}{\delta_s} = 0$

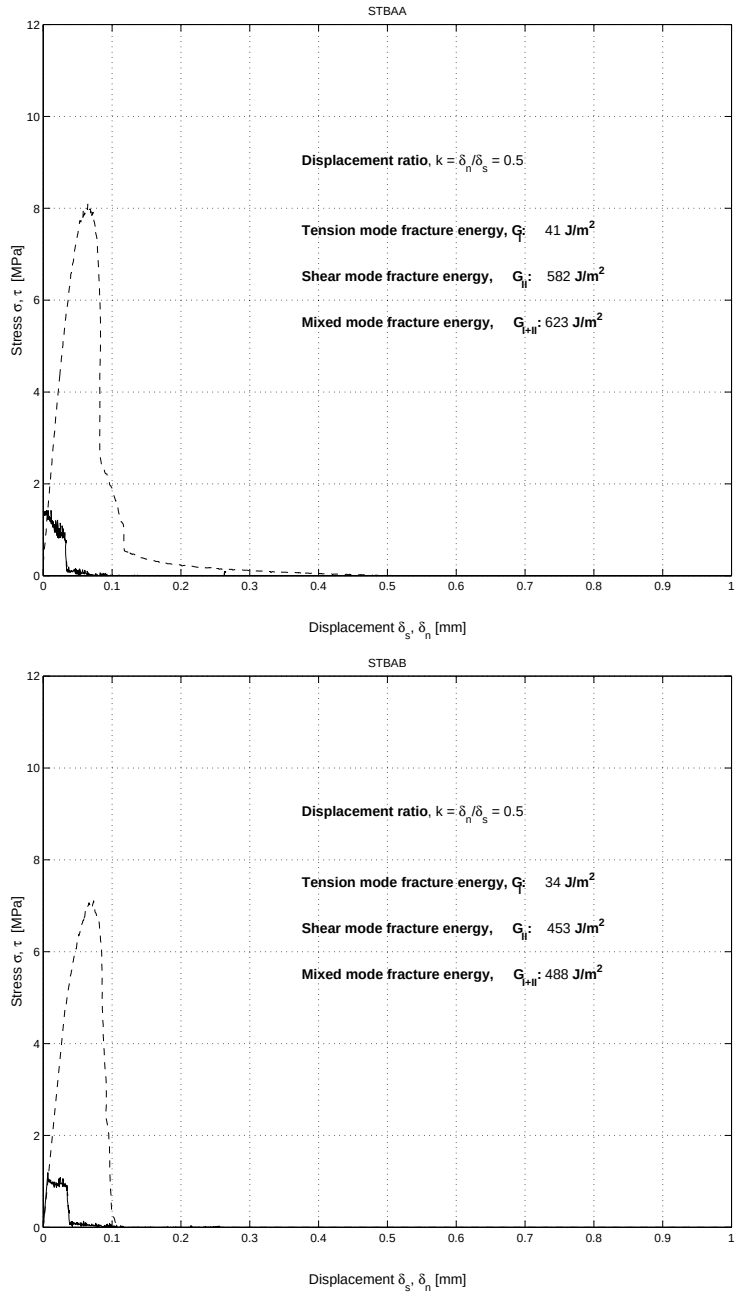

Figure B.4: Stress-displacement diagrams. Displacement ratio $k = \frac{\delta_n}{\delta_s} = 0.5$

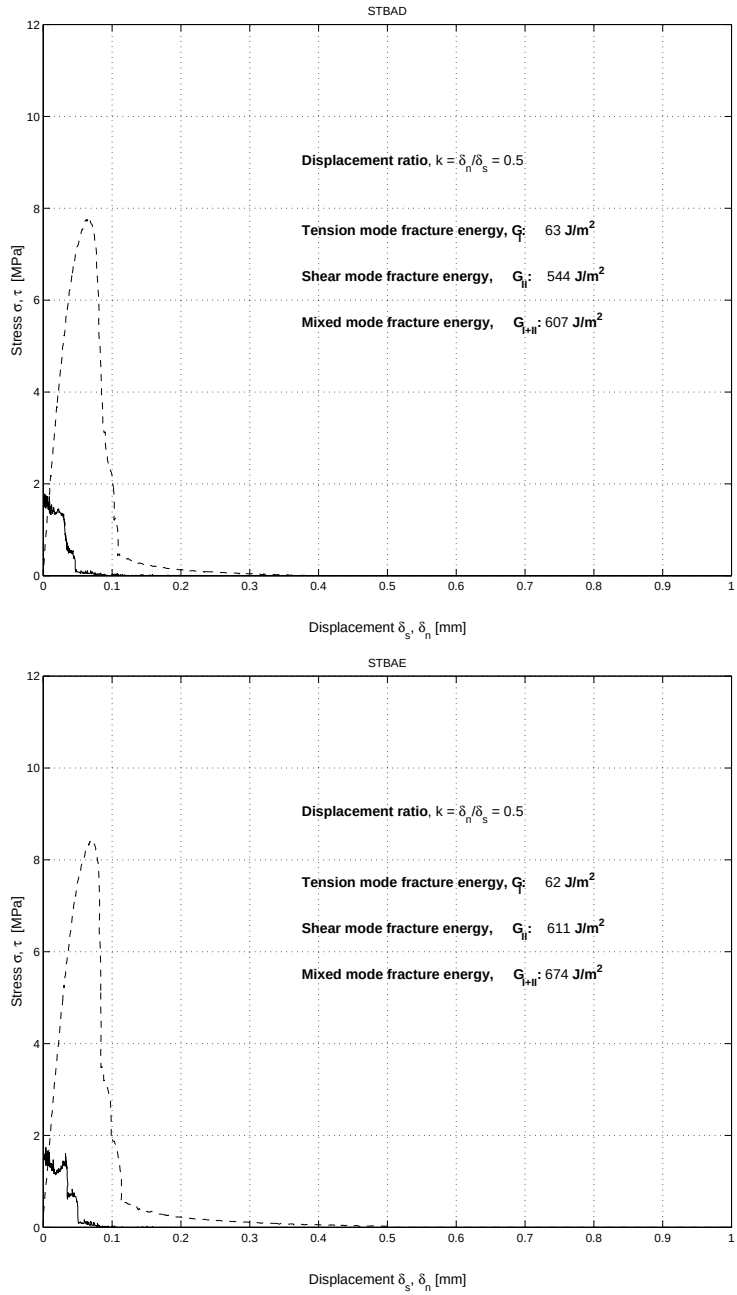

Figure B.5: Stress-displacement diagrams. Displacement ratio $k = \frac{\delta_n}{\delta_s} = 0.5$

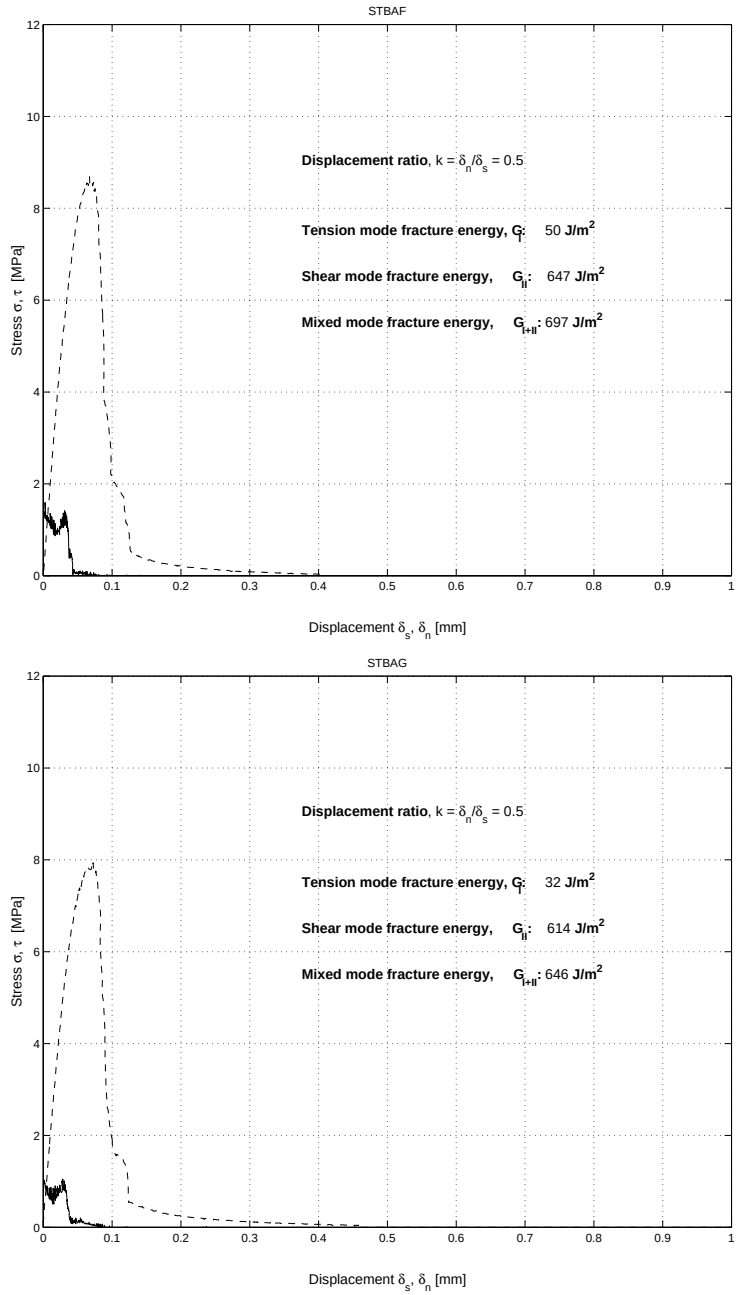

Figure B.6: Stress-displacement diagrams. Displacement ratio $k = \frac{\delta_n}{\delta_s} = 0.5$

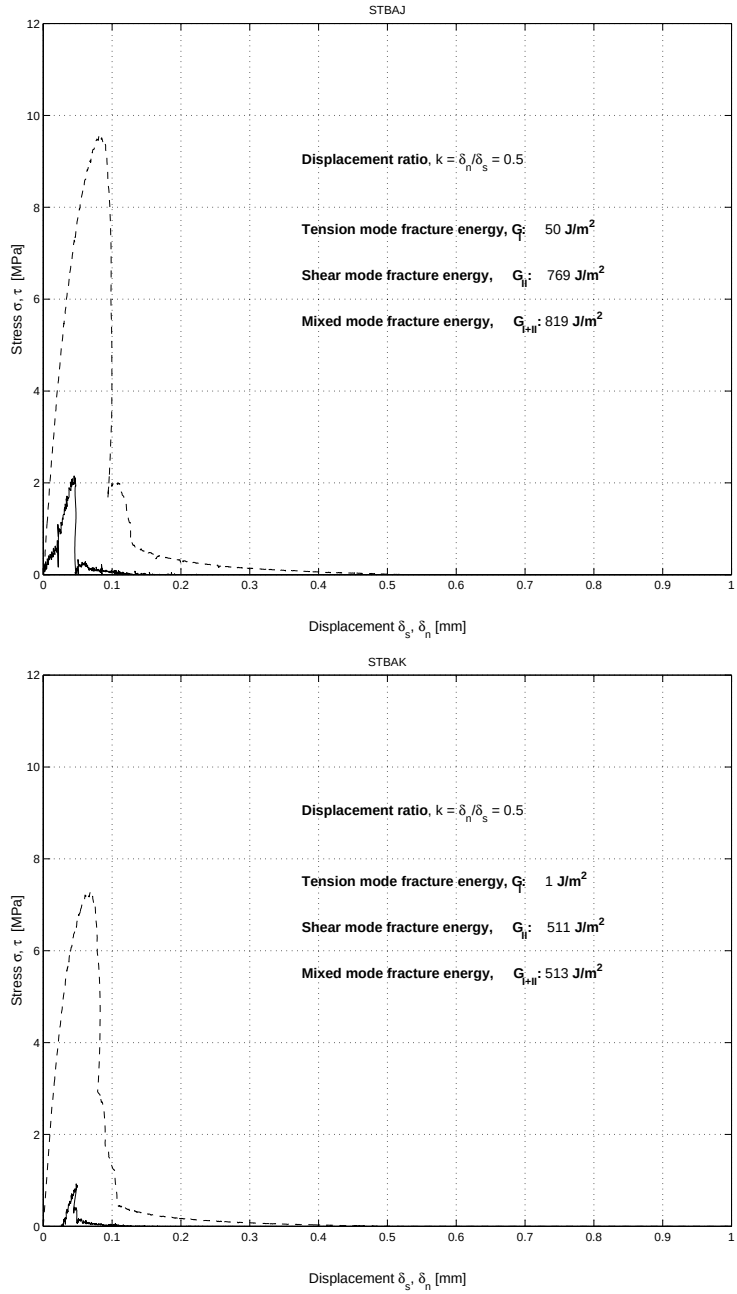

Figure B.7: Stress-displacement diagrams. Displacement ratio $k = \frac{\delta_n}{\delta_s} = 0.5$

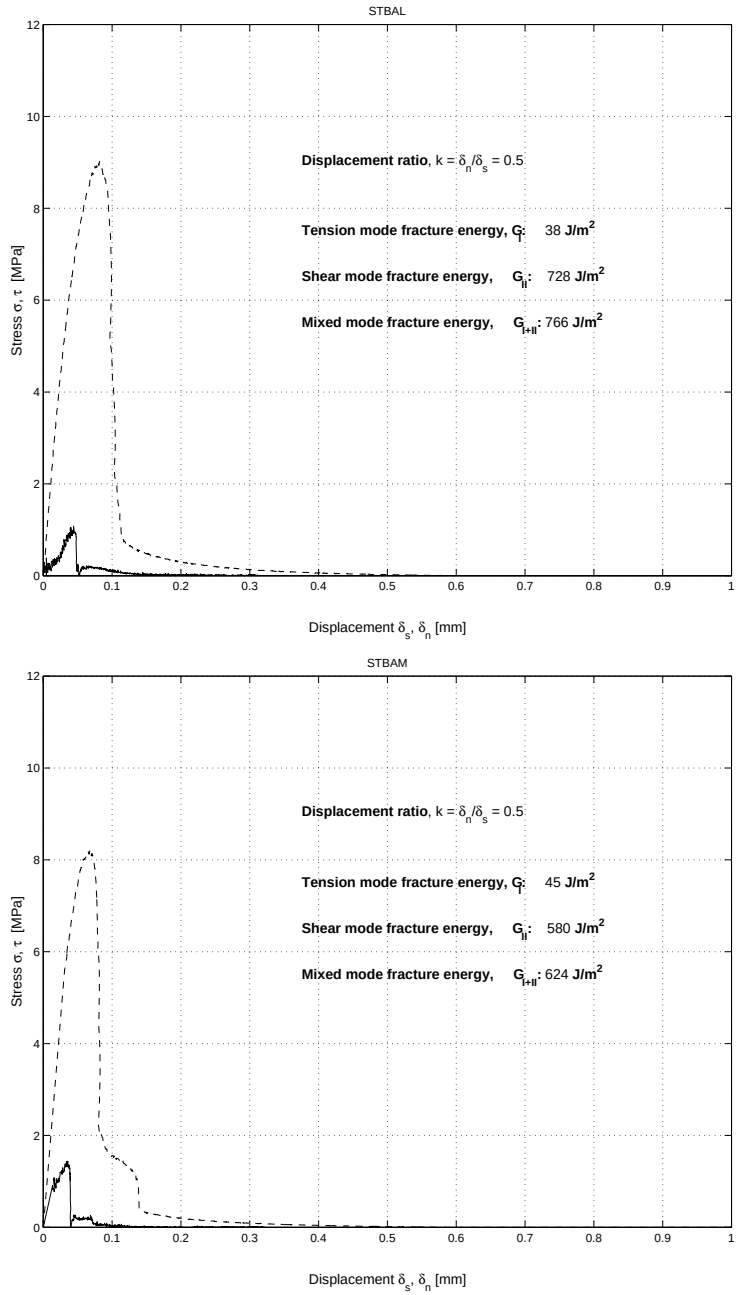

Figure B.8: Stress-displacement diagrams. Displacement ratio $k = \frac{\delta_n}{\delta_s} = 0.5$

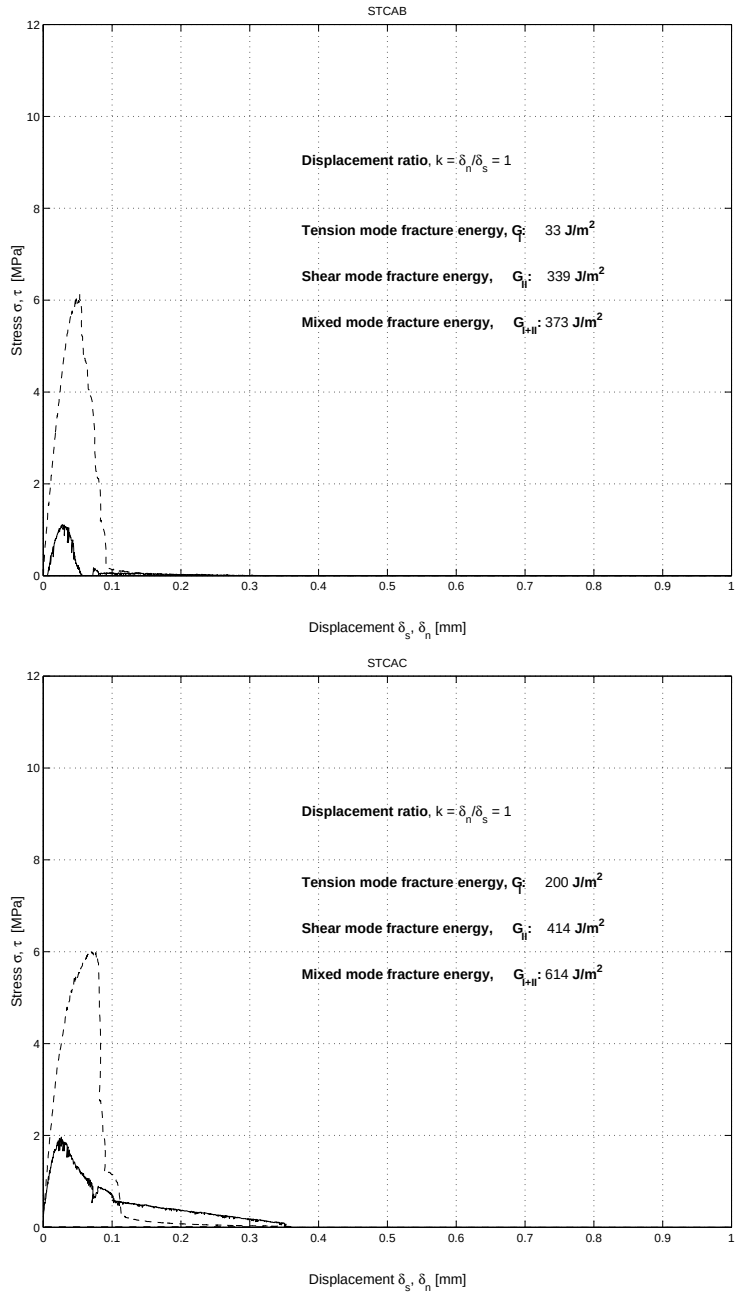

Figure B.9: Stress-displacement diagrams. Displacement ratio $k = \frac{\delta_n}{\delta_s} = 1.0$

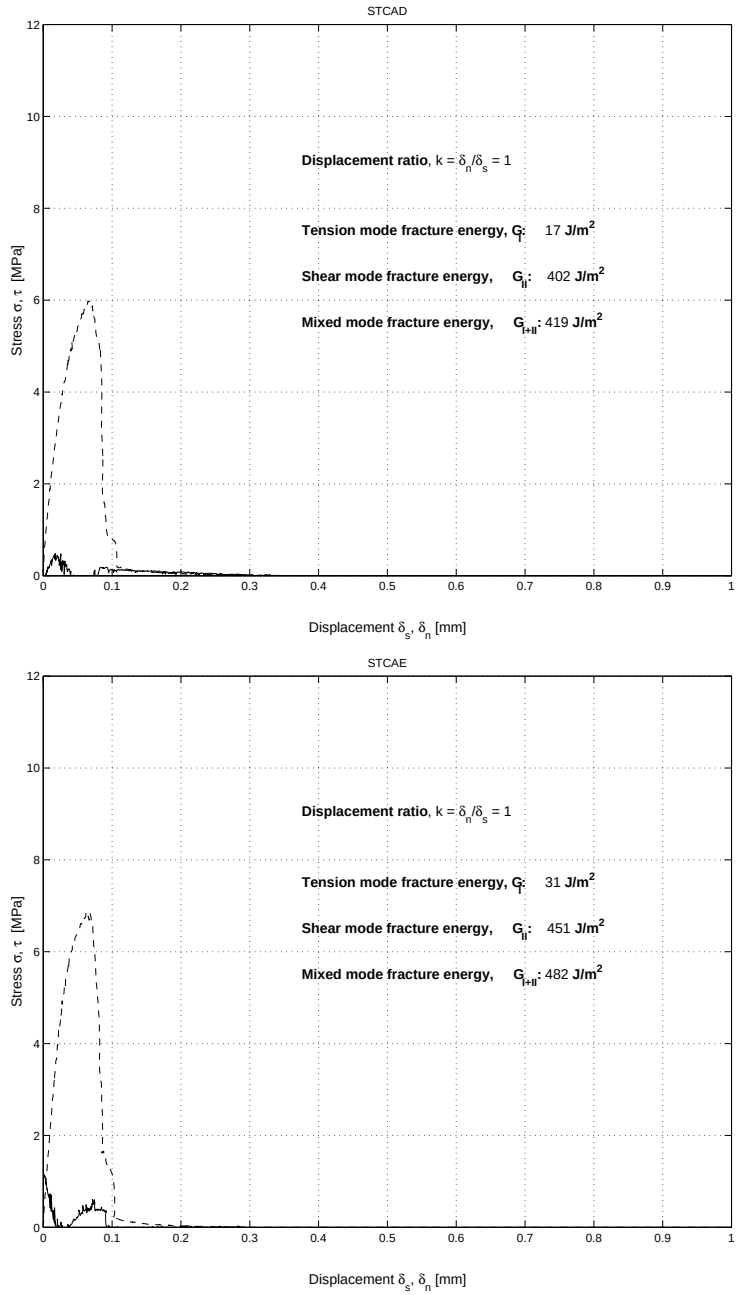

Figure B.10: Stress-displacement diagrams. Displacement ratio $k = \frac{\delta_n}{\delta_s} = 1.0$

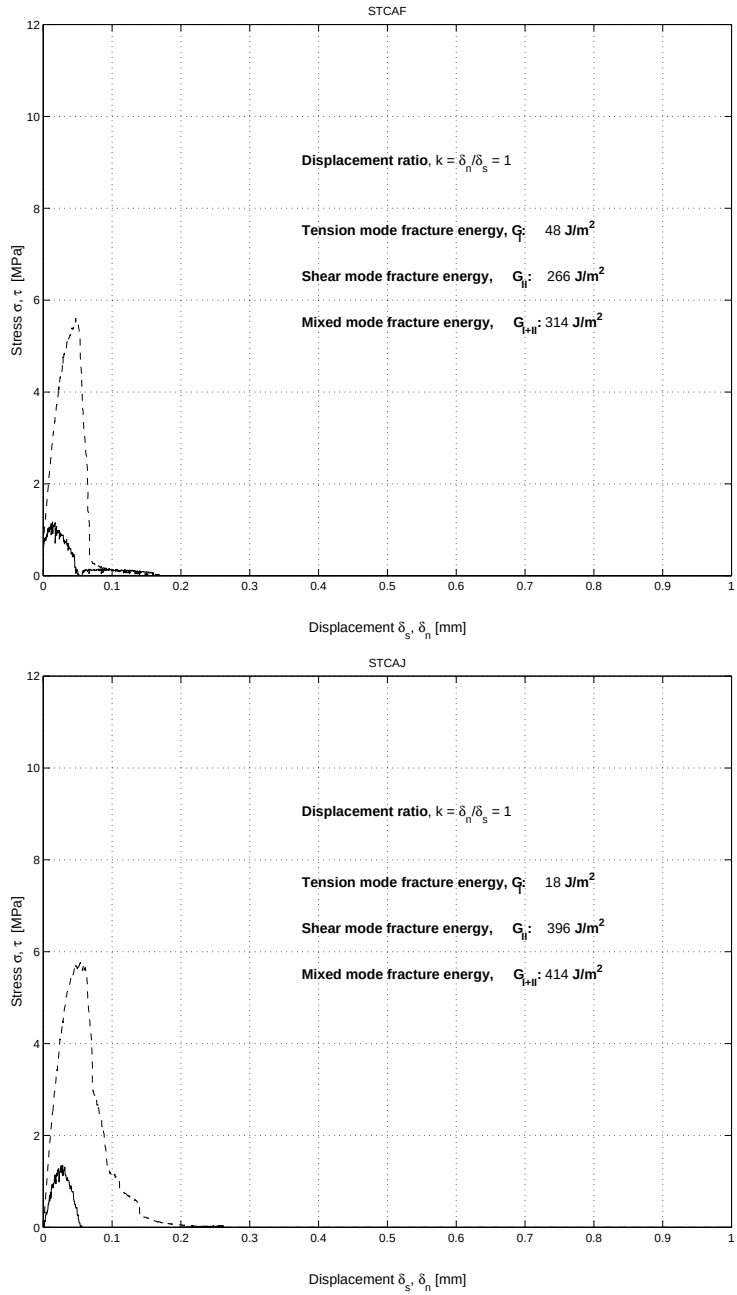

Figure B.11: Stress-displacement diagrams. Displacement ratio $k = \frac{\delta_n}{\delta_s} = 1.0$

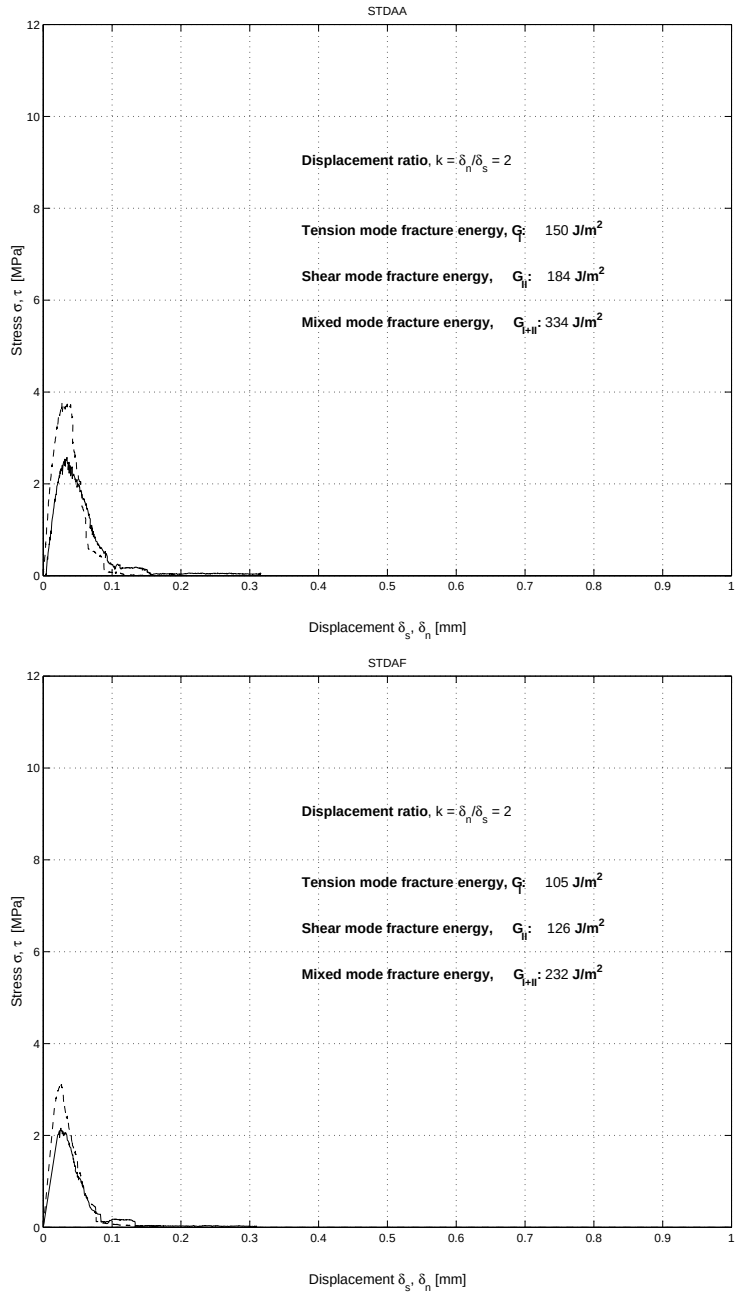

Figure B.12: Stress-displacement diagrams. Displacement ratio $k = \frac{\delta_n}{\delta_s} = 2.0$

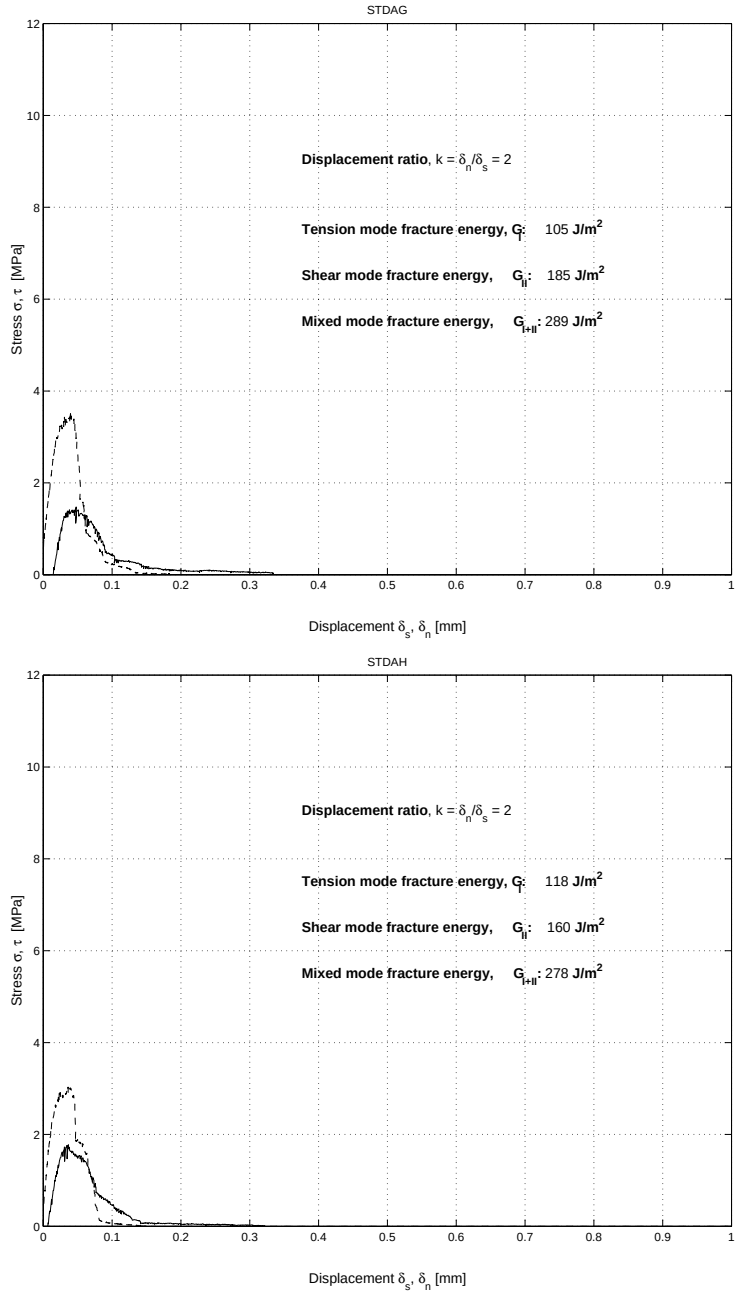

Figure B.13: Stress-displacement diagrams. Displacement ratio $k = \frac{\delta_n}{\delta_s} = 2.0$

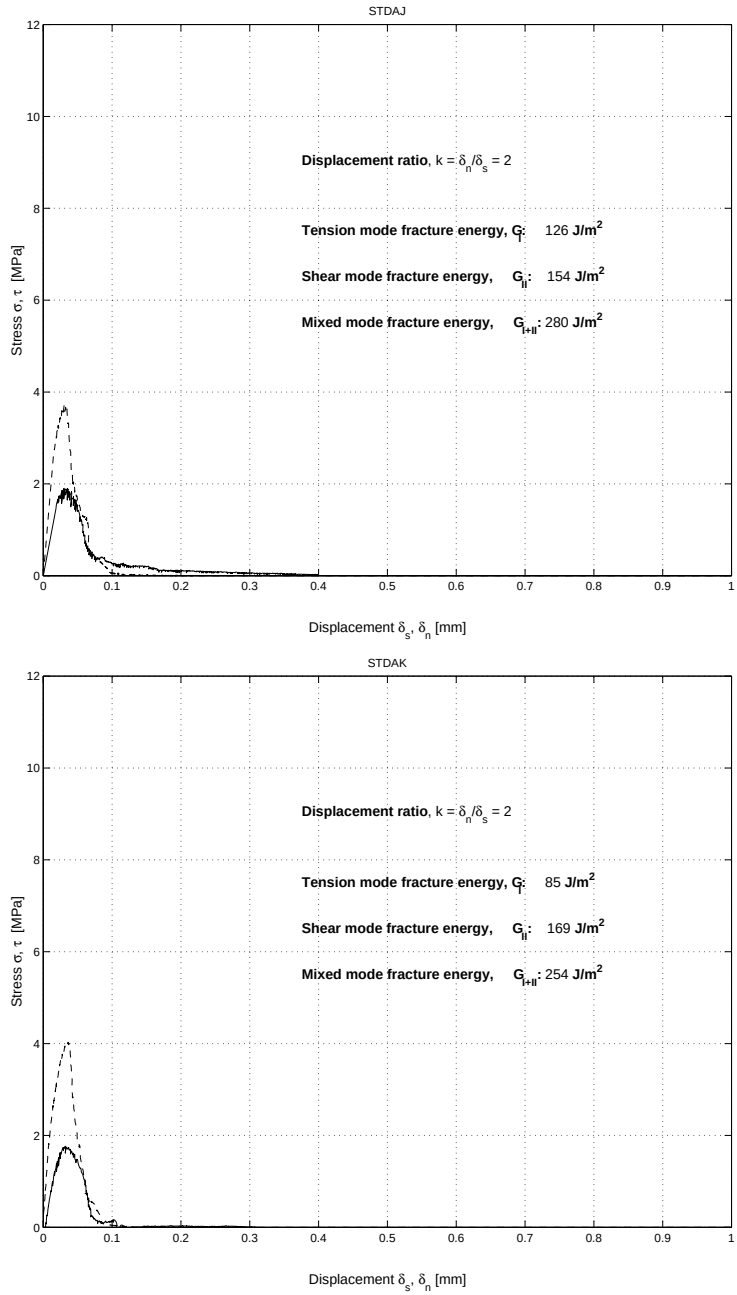

Figure B.14: Stress-displacement diagrams. Displacement ratio $k = \frac{\delta_n}{\delta_s} = 2.0$

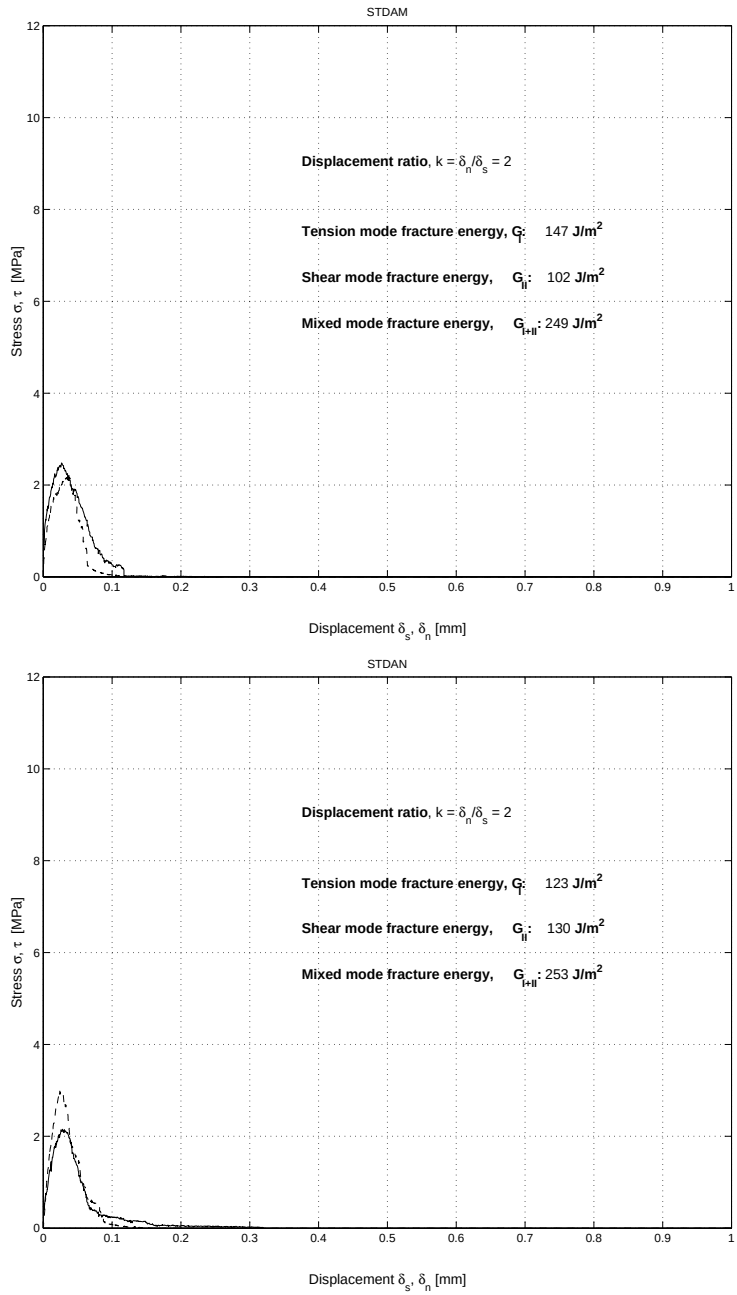

Figure B.15: Stress-displacement diagrams. Displacement ratio $k = \frac{\delta_n}{\delta_s} = 2.0$

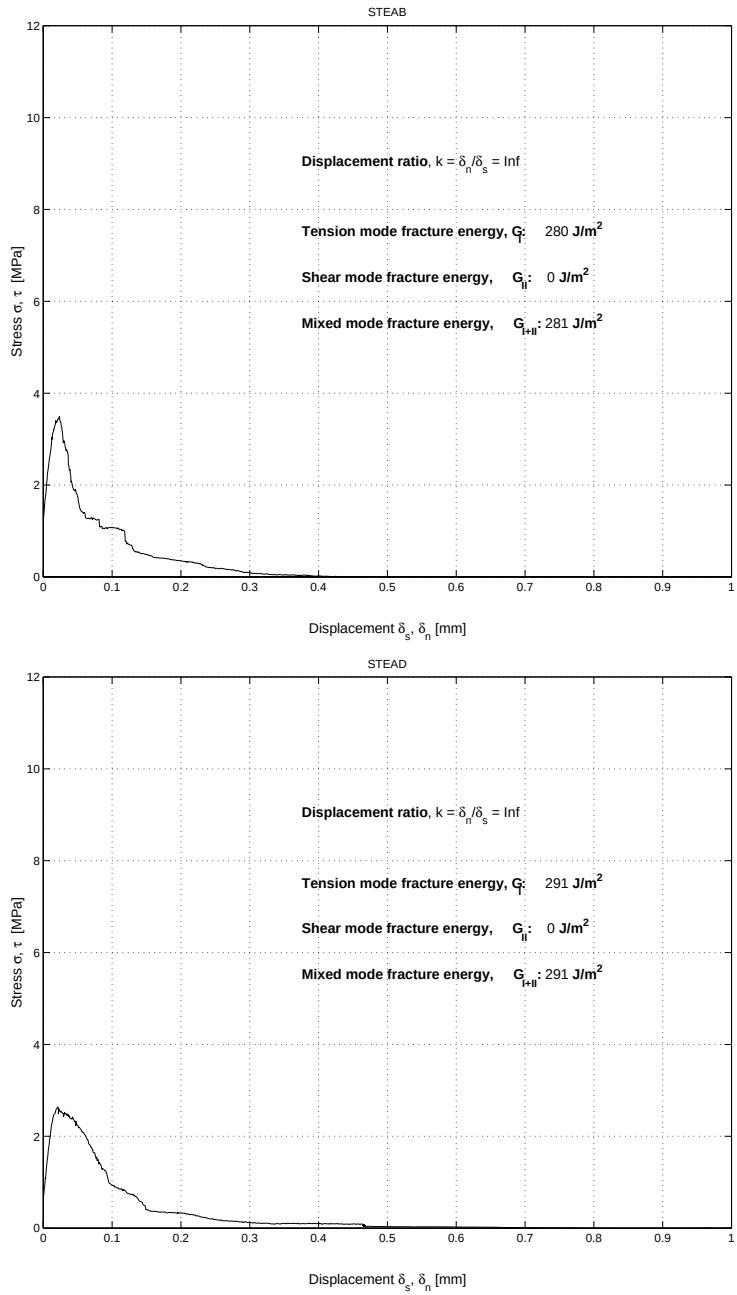

Figure B.16: Stress-displacement diagrams. Displacement ratio $k = \frac{\delta_n}{\delta_s} = \infty$

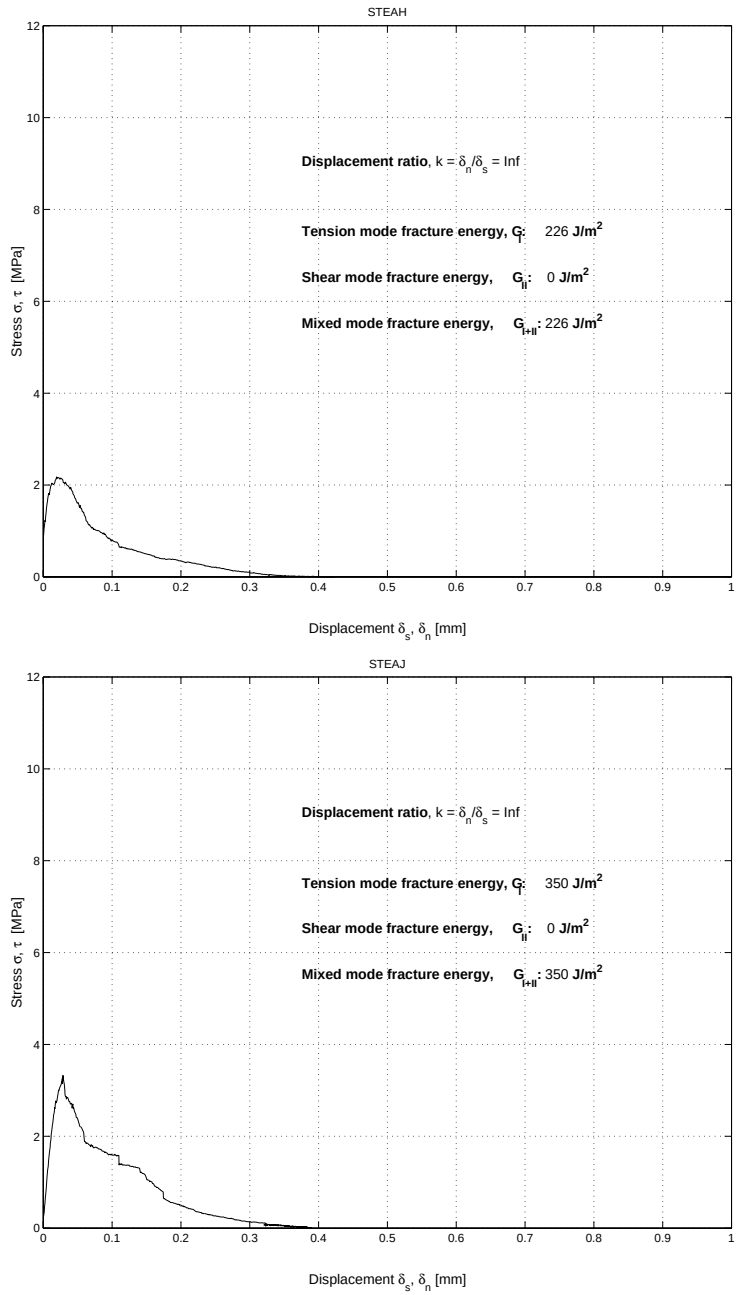

Figure B.17: Stress-displacement diagrams. Displacement ratio $k = \frac{\delta_n}{\delta_s} = \infty$

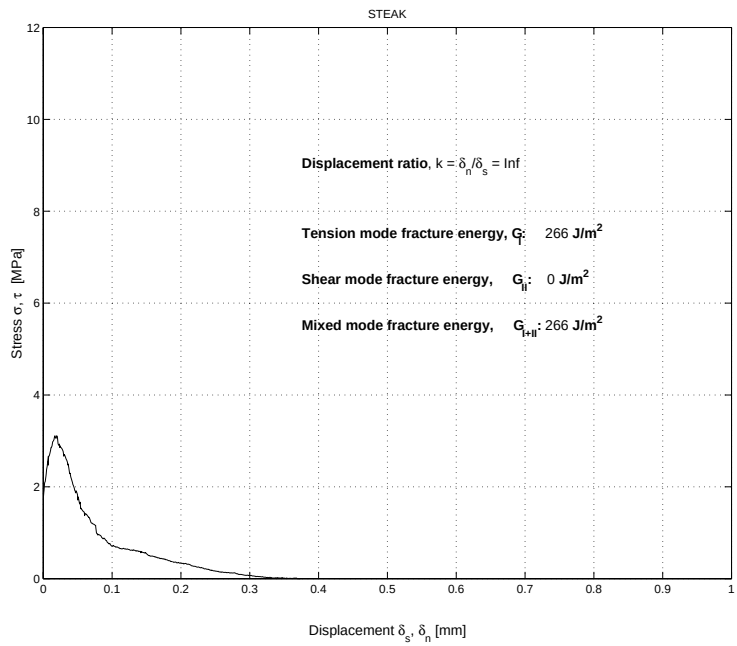

Figure B.18: Stress-displacement diagrams. Displacement ratio $k = \frac{\delta_n}{\delta_s} = \infty$

Appendix C

Linear Elastic Fracture Mechanics Model

C.1 Basic theory

The following description of the basic and applied theory is from Petersson [8]. A body of linear elastic material loaded in such a way that the strains can be considered as small (except for the cracking process zone) is studied. We may write the equilibrium equations as

$$\frac{\partial \sigma_{ij}}{\partial x_j} + b_i = 0 \tag{C.1}$$

in the volume V, where $\sigma_{ij} = \sigma_{ji}$ denotes a stress component, b_i a body force component and x_j refers to a Cartesian coordinate system. Conventional summation rule is applied. On the boundary surface S the tractions are defined by

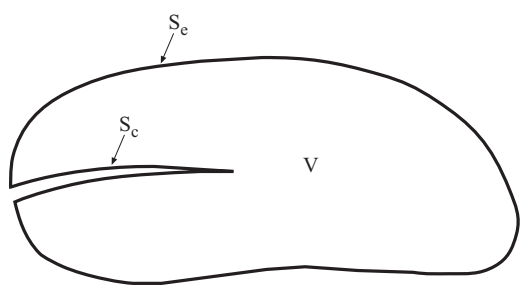

Figure C.1: Studied body with a crack. Total boundary surface $S = S_e + S_c$

$$p_i = n_j \sigma_{ij} \tag{C.2}$$

where n_j is a direction cosine for the outward normal to the surface S. The stresses are related to the strains ϵ,

$$\sigma_{ij} = D_{ijkl} \epsilon_{kl} \tag{C.3}$$

where D is a symmetric tensor. Due to the assumption of small deformations the strains are

$$\epsilon = \frac{1}{2} \left(\frac{\partial u_i}{\partial x_j} + \frac{\partial u_j}{\partial x_i} \right) \tag{C.4}$$

where u_i denotes a displacement component. Due to the tensor symmetry of D we may write

$$\epsilon_{ij}\sigma_{ij} = \frac{\partial u_i}{\partial x_j} D_{ijkl} \frac{\partial u_k}{x_l} \tag{C.5}$$

For a body with a crack, Figure (C.1), a week formulation of the equilibrium equations may be established, starting from Eq.(C.1). Weighting functions v_i (i = 1,2,3) are introduced [23]

$$\int_V v_i \frac{\partial \sigma_{ij}}{\partial x_j} dV + \int_V v_i b_i dV = 0 \tag{C.6}$$

By integration by parts and utilizing Eq.(C.2) we get

$$\int_V \frac{\partial v_i}{\partial x_j} \sigma_{ij} dV = \int_V v_i b_i dV + \int_S v_i p_i dS \tag{C.7}$$

or

$$\int_V \frac{\partial v_i}{\partial x_j} D_{ijkl} \frac{\partial u_k}{\partial x_l} dV = \int_V v_i b_i dV + \int_S v_i p_i dS \tag{C.8}$$

Let us now assume a disturbance between two studied states, ①and ② For state ① we choose the weighting functions as

$$v_i = v_i^{①} = u_i^{②} \tag{C.9}$$

and for state ②

$$v_i = v_i^{②} = u_i^{①} \tag{C.10}$$

This yields that

$$\int_V \frac{\partial u_i^{②}}{\partial x_j} D_{ijkl} \frac{\partial u_k^{①}}{\partial x_l} dV = \int_V \frac{\partial u_i^{①}}{\partial x_j} D_{ijkl} \frac{\partial u_k^{②}}{\partial x_l} dV \tag{C.11}$$

and according to Eq.(C.6) and Eq.(C.7) that

$$\int_V u_i^{②} b_i^{①} dV + \int_S u_i^{②} p_i^{①} dS + \int_V u_i^{①} p_i^{②} dV + \int_S u_i^{①} p_i^{②} dS = 0 \tag{C.12}$$

Alternatively,

$$\int_V (u_i^{②} b_i^{①} - u_i^{①} b_i^{②}) dV + \int_S (u_i^{②} p_i^{①} - u_i^{①} p_i^{②}) dS = 0 \tag{C.13}$$

We may now study a case where b_i and p_i are constant between states ①and ② except for the cracking area S_c. By use of the notation

$$\begin{aligned} \delta u_i &= u_i^{②} - u_i^{①} \\ \delta b_i &= b_i^{②} - b_i^{①} \\ \delta p_i &= p_i^{②} - p_i^{①} \end{aligned} \tag{C.14}$$

Eq.(C.13) can be rewritten as

$$\int_V b_i \delta u_i dV + \int_{S_e} p_i \delta u_i dS = \int_{S_c} (u_i \delta p_i - \delta u_i p_i) dS \tag{C.15}$$

The crack region is assumed to be so thin that the tractions p_i approximately are equal on two adjacent points on the surface S_c (symbolically $S_c = 2A_c$)). This

makes it meaningful to introduce the relative displacements w_i (crack opening and slips) with respect to the surface A_c instead of the displacements u_i on S_c. By this Eq.(C.15) can be written as

$$\int_V b_i \delta u_i dV + \int_{S_c} p_i \delta u_i dS = \int_{A_c} (w_i \delta p_i - \delta w_i p_i) dA \tag{C.16}$$

Let us then study a case where the influence of a disturbance to the system can be expressed by a single crack coordinate **a** and where $dA = b_c \cdot da$ with constant width b_c. Let us further assume that the crack propagation occurs in a self-similar way corresponding to

$$\begin{aligned} \delta w_i &= \frac{dw_i}{da}\delta a \\ \delta p_i &= \frac{dp_i}{da}\delta a \end{aligned} \tag{C.17}$$

By these assumptions we may write Eq.(C.15) as

$$\int_V b_i \frac{du_i}{da} dV + \int_{S_c} p_i \frac{du_i}{da} dS = b_c \int (w_i \frac{dp_i}{da} - \frac{dw_i}{da} p_i) da \tag{C.18}$$

In order to simplify we assume that the relations between p_i and w_i (i=1,2,3) are unique (for the current ratios between p_1, p_2 and p_3 or w_1, w_2 and w_3), see Figure (C.2). This means that we can write $p_i = p_i(w_i)$ or $w_i = w_i(p_i)$. This yields

$$\int_{a_c} (w_i \frac{dp_i}{da} - \frac{dw_i}{da} p_i) da = \int_0^{p_{i0}} w_i dp_i - \int_{w_{i0}}^0 p_i dw_i = 2G_c \tag{C.19}$$

where

$$G_c = \sum_{i=1}^{3} G_{ci} = \int_0^{p_i 0} w_i dp_i = \int_0^{w_{i0}} p_i dw_i \tag{C.20}$$

Substitution of Eq.(C.19) into Eq.(C.18) results in

$$\int_V b_i \frac{du_i}{da} dV + \int_{S_e} p_i \frac{du_i}{da} dS = 2 b_c G_c \tag{C.21}$$

In case of concentrated forces $\{P\}$ only we may introduce for the cracking load level

$${P_c}^T = [P_{c1} P_{c2} \cdots P_{cn}] \tag{C.22}$$

with the associated displacements $\{u_c\}$,

$${u_c}^T = [u_{c1} u_{c2} \cdots u_{cn}] \tag{C.23}$$

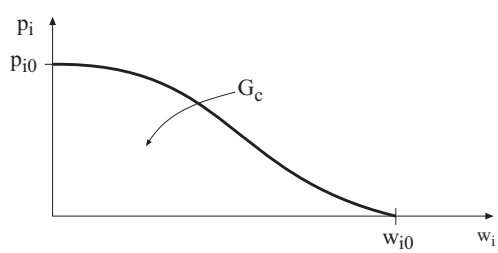

Figure C.2: Relation between cohesive stress p_i and relative displacement w_i

Eq.(C.21) can then be written on the form

$$P_c{}^T \frac{du_c}{da} = 2b_c G_c \tag{C.24}$$

This basic matrix equation, Eq.(C.24), can conveniently be used in finite element analysis where $\{P_c\}$ and $\{u_c\}$ will then refer to nodal loads and nodal displacements, respectively.

C.2 Applied theory

The two-dimensional structure introduced in Figure (C.3) carries a set of reference loads {P}. We assume that the material is linear elastic and by denoting the displacements with {u} we have

$$\{P\} = \begin{bmatrix} P_1 \\ P_2 \\ \vdots \\ P_n \end{bmatrix} \qquad \{u\} = \begin{bmatrix} u_1 \\ u_2 \\ \vdots \\ u_n \end{bmatrix} \tag{C.25}$$

The crack length is denoted with a and the fracture energy with G_c where G_c is considered to be a material parameter. This assumption is according to Griffith's theory. We advance by assuming that the external loads are increased proportionally, step by step. This means that the actual loads are $\alpha\{\mathrm{P}\}$ where α may be increased gradually up to the critical level of α which corresponds to the maximum load level for the actual state (crack length). This state may either reflect a stable or unstable crack growth. As we have assumed linear elasticity the corresponding displacements are $\alpha\{u\}$. Hence, we can express the displacements by the flexibility relation

$$\{u\} = [C]\{P\} \tag{C.26}$$

where the flexibility matrix $[C]$ is also termed as the compliance. The internal energy for the linear elastic material can now be expressed as

$$W = \frac{1}{2}\alpha^2\{P\}^T\{u\} = \frac{1}{2}\alpha^2\{P\}^T[C]\{P\} \tag{C.27}$$

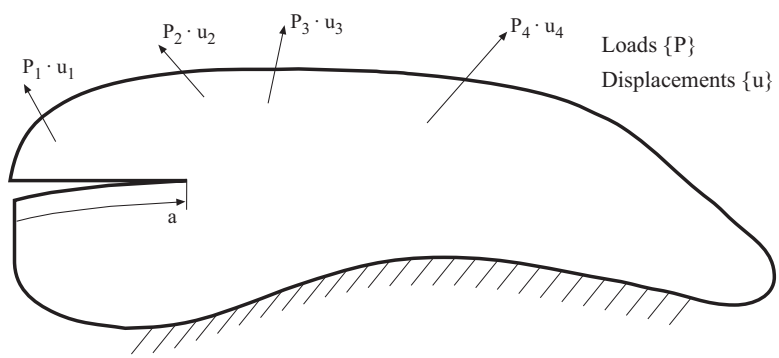

Figure C.3: Two-dimensional body with a crack

We now assume that the reference load P and the load multiplication factor α are kept constant with respect to variation of the crack length a. For the critical value of $\alpha = \alpha_c$ this gives us

$$\frac{\partial W}{\partial a} = \frac{1}{2}\alpha_c^2 \{P\}^T \left[\frac{\partial C}{\partial a}\right] \{P\} \tag{C.28}$$

As the second law of thermodynamics claims that the work performed by external forces, at quasi-static conditions, is equal to the work performed by internal forces, we may combine Eq.(C.28) and Eq.(C.24)

$$\frac{\partial W}{\partial a} = 2 b_c G_c \tag{C.29}$$

and we obtain

$$\alpha_c = \sqrt{\frac{2 b_c G_c}{\{P\}^T \frac{dC}{da} \{P\}}} \tag{C.30}$$

This equation is straightforward to apply in finite element analysis. For the numerical analysis, based on the finite element method, we will utilize Eq.(C.30). The critical load factor α_c at cracking is extracted from approximation of the equation. The load vector $\{P\}$ contains given reference loads. We allow the crack length to increase gradually so for each value of $a = a_i$ we obtain the corresponding displacements u_i. The stepwise crack propagation may be approximated by

$$\Delta a_i = a_{i+1} - a_i \tag{C.31}$$

obtaining the approximate critical load factor

$$\alpha_{ci} = \sqrt{\frac{2 b_c \Delta a_i G_c}{\{P\}^T \left(\{u\}_{i+1} - \{u\}_i\right)}} \tag{C.32}$$

where the crack length is defined as

$$a \approx \frac{a_{i+1} + a_i}{2} \tag{C.33}$$

One of the difficulties in fracture analysis is the existence of mixed mode fracture, i.e. we have the fracture energy G_c dependent on the mode of fracture. The method adopted here for choosing a suitable value includes that the fracture energy may be obtained by estimating some average value of the ratio $\frac{\bar{\sigma}_\perp}{\bar{\tau}}$ between the normal and shear stresses in the crack process zone. In a finite element analysis an evaluation of the nodal forces from the individual elements close to the crack tip might give reasonable estimate of the mixed mode state. An illustration is given by Figure (C.4), where the summations of nodal forces for elements on each side of the crack are identical except for the sign. We approach the stress ratio in the assumed process zone by

$$\frac{\bar{\sigma}_\perp}{\bar{\tau}} \approx \frac{\sum_s P_{ys}}{\sum_s P_{xs}} \tag{C.34}$$

The index s refers to summation of nodal forces over the row of elements, on either side of the crack, which are assigned to the process zone. A reasonable relation between the stress ratio $\frac{\bar{\sigma}}{\bar{\tau}}$ and the fracture energy G_c has between suggested by Gustafsson [4]. This relation is shown in Figure (C.5) which is based on Eq.(3.32). The material parameters used to establish the relationship are as follows:

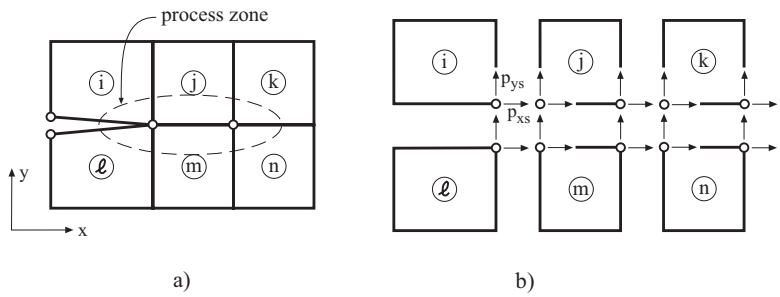

Figure C.4: Nodal element forces close to cracking process zone

Elasticity moduli	$E_{\parallel}$	12000	MPa
	$E_{\perp}$	400	MPa
Shear modulus	$G_{\parallel,\perp}$	750	MPa
Poisson's ratio	$\nu_{\parallel,\perp}$	0.41	-
Fracture energy	$G_{I,c}$	300	Nm/m^2
	$G_{II,c}$	1050	Nm/m^2

Table C.1: Material parameters in mixed mode fracture criterion

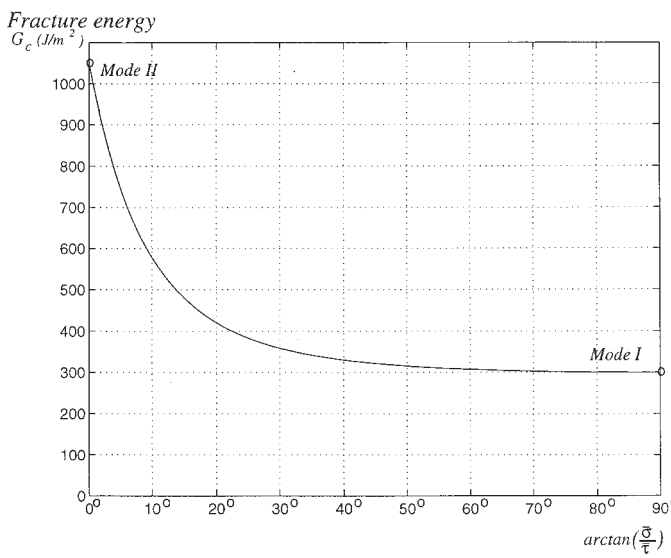

Figure C.5: Fracture criterion applied for mixed mode